

Flow Interaction and Heat Transfer Between Two Cylinders in a Uniform Air-Stream

Von dem Fachbereich Maschinenbau
der Universität Hannover
zur Erlangung des akademischen Grades
Doktor-Ingenieur
genehmigte
Dissertation
von

M. Sc. Eng. Khaled Yahia Zakaria

geboren am 15. November 1967 in Alexandria

2000

1. Referent: Professor Dr.-Ing. I. Teipel
2. Referent: Professor Dr.-Ing. M. Rautenberg
Tag der Promotion: 10.10.2000

Schlagwörter:

Deutsch: Strömung, Laminar, Zylinder
English: Flow, Laminar, Cylinder

**„Gedruckt mit Unterstützung des Deutschen Akademischen
Austauschdienstes“**

Vorwort

Diese Arbeit entstand während meiner Anwesenheit als DAAD Stipendiat am Institut für Mechanik der Universität Hannover.

Mein besonderer Dank gilt Herrn Professor Dr.-Ing. I. Teipel, der die vorliegende Arbeit angeregt, betreut und letztlich kritisch begutachtet hat. Professor Teipel war für mich nicht nur ein Doktorvater sondern ein echter Vater, der mir unglaublich viel geholfen hat. Herrn Professor Dr.-Ing. M. Rautenberg danke ich für die Übernahme des Korreferates.

Desweiteren möchte ich allen Kollegen und Freunden, die mir während der Fertigstellung dieser Dissertation mit Rat und Tat hilfreich zur Seite gestanden haben, meinen herzlichen Dank aussprechen. Insbesondere sind in diesem Zusammenhang mein Wegbegleiter Volker Caspary und Herr Dr.-Ing Hans-Georg Jacob zu nennen. Herrn Burkhard Salge möchte ich für seine Hilfe während der Rechenphase dieser Arbeit danken. Herrn Volker Meine möchte ich auch für sein Mitwirken an der äußeren Gestaltung der Arbeit ganz herzlich danken.

Passende Worte des Dankes für meine Eltern zu finden, die meine Entwicklung stets mit Geduld, Verständnis und vielen Freiheiten unterstützt haben, ist ebenso unmöglich wie die Dankbarkeit gegenüber meiner Lebensgefährtin Amira Ezzat auszudrücken, die mir in all den Monaten und Jahren immer wieder gezeigt hat, dass Arbeit alleine einen Menschen nicht ausfüllen kann.

Am Ende möchte ich mir beim DAAD bedanken, der mir die Gelegenheit gegeben hat, hier in Deutschland promovieren zu dürfen.

Hannover, im Oktober 2000

Abstract

Flow between two cylinders located side-by-side in a stream of air is a very complicated phenomenon and has long been the subject of interest for fundamental studies in fluid dynamics. The aim of the present work is to solve and study the problem of the fluid flow and forced convection around two circular cylinders in a stream of air for the case of unsteady laminar flow with Reynolds number ranging from 100 to 500, constant heat flux dissipating from both cylinders, as well as constant wall temperature for both cylinders. Flow visualization as well as heat transfer correlations are considered. The results showed a good agreement between the present work and that found in the literature. The biased nature of the flows could be verified numerically and the results showed that this effect takes place for any pitch to diameter ratio smaller than 2.0. The heat transfer results showed that for both modes of heat transfer used the most configuration that optimizes the heat transfer process is to put the cylinders about two diameters away from each other.

Zusammenfassung

Die Strömung um einen ruhenden Zylinder ist schon vielfältig behandelt worden, und es haben sich wichtige Resultate für verschiedene Anwendungsfälle ergeben. Das Ziel der vorliegenden Arbeit ist nun, die Strömung und den Wärmeübergang um zwei nebeneinander liegenden Zylinder numerisch zu untersuchen. Als Ergebnis ist von Bedeutung einmal der Widerstandskoeffizient. Er hängt entschieden von der Reynoldszahl und vom gegenseitigen Abstand der beiden Zylinder ab. Auch bei einer stationären Anströmung ergibt sich ab einer bestimmten Kombination der oben genannten Parameter zunächst eine oszillierende Abströmung. Die Mittellinie stellt dabei eine Symmetrielinie dar. Bei kleiner werdendem Abstand der beiden Zylinder verformt sich diese Symmetrielinie zu einer Art zeitlich irregulär schwankenden Mittellinie. Aus der Literatur weiß man, dass dieser Vorgang auch im Experiment nachgewiesen wurde.

Das zweite Resultat betrifft den Wärmeübergangskoeffizienten. Es wurden die Fälle konstante Wandtemperatur und konstanter Wärmefluss an der Wand behandelt. Wenn der Zylinderabstand zu Zylinderdurchmesser um zwei liegt, stellt sich jedes Mal ein optimaler Wert ein.

Contents

Abstract	I
Zusammenfassung	II
Nomenclatures	VIII
Chapter 1 Introduction	1
1.1 Motivation	1
Chapter 2 Problem Formulation	5
2.1 Geometry	5
2.2 Boundary and Initial Conditions	6
2.2.1 Inlet Boundary Condition	6
2.2.2 Upper and Lower Boundary Conditions	6
2.2.3 Outlet Boundary Conditions	6
2.2.4 Initial Conditions	7
Chapter 3 Literature Review	9
3.1 One Cylinder	9
3.1.1 Fluid Flow	9
3.1.2 Fluid Flow-Heat Transfer	13
3.2 Two and More Cylinders.....	14

3.2.1	Fluid Flow	14
3.2.2	Fluid Flow-Heat Transfer	16
Chapter 4 Governing Equations		17
4.1	Conservation Principles.....	17
4.2	Mass Conservation	18
4.3	Momentum Conservation.....	19
4.4	Conservation of Scalar Quantities.....	22
Chapter 5 Numerical Solution of The Governing Equations		25
5.1	General Formulation.....	25
5.2	Spatial Flux Discretization	27
5.3	Temporal Discretization.....	28
5.3.1	Fully Implicit	28
5.3.2	Crank-Nicholson.....	29
5.4	Convective Flux Formulation.....	29
5.4.1	Low-Order Spatial Discretization Schemes.....	30
5.4.1.1	Upwind differencing (UD)	30
5.4.2	Higher-Order Spatial Discretization Schemes.....	31
5.4.2.1	Linear upwind differencing (LUD)	31
5.4.2.2	Central differencing (CD).....	31
5.4.2.3	Quadratic upstream interpolation of convective kinematics (QUICK)...	32
5.5	Final FV Equations.....	32
5.6	Solution Algorithms	33
5.6.1	The PISO Algorithm.....	33

5.6.1.1	Working equations.....	34
5.6.1.2	Solution sequence.....	35
Chapter 6	Benchmarking Computations	39
6.1	The Benchmark Problem.....	39
6.2	Geometry and Boundary Conditions of the Problem.....	39
6.3	Test Cases.....	41
6.3.1	Case a) Steady Flow.....	41
6.3.2	Case b) Unsteady Flow	41
6.4	Results	42
6.4.1	Case a) Steady Flow.....	42
6.4.1.1	The numerical results	42
6.4.1.2	The gained experience during this test phase.....	43
6.4.1.2.1	The solution grid	43
6.4.1.2.2	The discretization scheme.....	45
6.4.1.3	Benchmark Test Extension.....	45
6.4.1.3.1	Steady flow edge-Reynolds number.	45
6.4.1.4	The ability to simulate the free flow condition	47
6.4.2	Case b) Unsteady Flow	48
6.4.2.1	The numerical results	48
6.4.2.2	The gained experience during test phase.....	50
6.4.2.2.1	Time step.....	50
6.4.2.2.2	Temporal discretization.....	51
6.4.2.3	Benchmark test extension.....	51

Chapter 7	Two Cylinders in a Uniform Stream.	53
7.1	Introduction	53
7.2	Normalizing The Results.....	54
7.3	Fluid Flow Results.....	56
7.3.1	The Vortex Shedding and Flow Pattern Behind The Cylinders	56
7.3.2	Pressure Distribution.....	65
7.3.2.1	Pressure field	65
7.3.2.2	Normalized pressure distribution on the surface of the cylinders	67
7.3.2.2.1	Instantaneous pressure variation	67
7.3.2.2.2	Mean pressure distribution on the surface of the cylinders.....	67
7.3.3	Lift, Drag Coefficients and Strouhal Number.....	70
7.3.3.1	Lift coefficients	70
7.3.3.2	Strouhal number	72
7.3.3.3	Drag coefficients	72
Chapter 8	Heat Transfer Results	75
8.1	Constant Wall Heat Flux	76
8.1.1	Thermal Field.....	76
8.1.2	Local Nusselt Number Around The Cylinders	80
8.1.2.1	Instantaneous local Nusselt number	80
8.1.2.2	Mean local Nusselt number	82
8.1.2.3	Mean average Nusselt number	83
8.2	Isothermal Walls.....	84
8.2.1	Thermal Field.....	85
8.2.2	Local Nusselt Number Around The Cylinders	89

8.2.2.1	Instantaneous local Nusselt number	89
8.2.2.2	Mean local Nusselt number	91
8.2.2.3	Mean average Nusselt number	92
Chapter 9	Effect of Reynolds Number on Heat Transfer Characteristics	95
9.1	Constant wall heat flux.....	95
9.1.1	Thermal Field.....	95
9.1.2	Mean Local Nusselt Number	97
9.1.3	Mean Average Nusselt Number.....	101
9.2	Isothermal Walls.....	102
9.2.1	Thermal Field.....	102
9.2.2	Mean Local Nusselt Number	105
9.2.3	Mean Average Nusselt Number.....	107
Chapter 10	Conclusions and Future Work	109
10.1	Conclusions	109
10.2	Future Work	111
REFERENCES		113
Lebenslauf		121

Nomenclatures

B	Distance between the domain entrance and the center of any cylinder
b_f	Body forces per unit mass
c_D	Drag coefficient
C_j	Convection term in Equ. (5.3)
c_L	Lift coefficient
CM	Control mass
Co	Courant number
c_p	Specific heat at constant pressure
C_p	Pressure coefficient
CV	Control volume
D	Cylinder diameter
\dot{D}	Rate of strain
D_j	Diffusion term in Equ. (5.3)
F	Vortex shedding frequency
F	Forces acting on the control volume
F_D	Drag force
F_j	Mass flux through face J
F_L	Lift force
H	Height of the domain of solution
I	Unit tensor
K	Thermal conductivity
L	Length of domain of solution
L_a	Length of recirculation

M	Mass
N	Direction normal to the surface
Nu	Nusselt number
P	Pressure
P	Normalized pressure
Pr	Prandtl number
Q	Heat flux
Q_ϕ	Source or sink of ϕ
q_o	Heat flux at the surface of cylinders
Re	Reynolds number
S	Distance between cylinders' centers
S	Surface of control volume
S	Viscous part of the stress tensor
T	Time
T	Stress tensor
T	Normalized time
t_i	Cartesian form of stress tensor
U	Velocity component in x direction
U	Normalized velocity in x direction
u_i	Cartesian components of the velocity vector \vec{V}
u_m	Maximum velocity at the entrance
V	Velocity vector
V	Velocity component in y direction
V	Normalized velocity in y direction
W	Velocity component in z direction
X	Normalized x distance
x_i	Cartesian coordinates in x , y , and z direction
Y	Normalized y distance

ϑ	Temperature
ϕ	Conserved intensive property
Φ	Extensive property
ρ	Density
μ	Dynamic viscosity
ν	Kinematic viscosity
Γ	Diffusivity for the quantity ϕ .
θ	Angle measured from base point of cylinder in counter clockwise direction
α	Angel represents the front stagnation point measured from the base point
δt	Time interval
Ω_{CM}	Volume occupied by the CM
δ_{ij}	Kronecker symbol
τ_{ij}	Viscous part of the stress tensor
Θ	Normalized temperature

Subscripts:

∞	Infinity
ϕ	Arbitrary variable
<i>average</i>	Average value
<i>b</i>	Base
<i>CM</i>	Control mass
<i>D</i>	Cylinder Diameter
<i>d</i>	Diffusion
<i>i, j, k</i>	<i>x, y, and z direction</i>
<i>mean</i>	Mean value
<i>N</i>	Neighbor
<i>o</i>	Base or at the cylinder surface

p At point P
 r Interpolated

Superscripts:

n At any time step
 $n+1$ At time step $n + \delta t$
 o At the start time
T Transpose
 \rightarrow Indicates a vector quantity

Chapter 1

Introduction

1.1 Motivation

Flow past a circular cylinder is a very complicated phenomenon and has long been the subject of interest for fundamental studies in fluid dynamics. This flow configuration is widespread in meteorology and astronomy as well as in engineering applications such as heat transfer surfaces in boilers, heat exchangers, and the like in various power generation plants and chemical plants.

While there is a considerable amount of theoretical and experimental work devoted to the studies of different aspects of flow around a single cylinder, information about the flow around two and more cylinders is very limited and mostly experimental.

The history of investigation of the flow around two circular cylinders is an example of unsystematic and fragmentary research, which has been carried out mainly to solve immediate practical problems. Industrial applications stimulated research projects appeared in various areas of engineering and science. Applications started in aeronautical engineering (twin struts to support wings), moved to hydronautical engineering (periscope, snorkel and radar mast vibrations), civil engineering (twin chimney stacks in wind, jetties and offshore structures in high seas), electrical engineering (twin-conductor transmission line vibration), mechanical engineering (in connection with heat exchanger tube vibrations) and chemical engineering (pipe-rack forces).

It is common in practice to assume that two cylinders should behave in a flow similar, or even in an identical manner, to a single cylinder. This assumption is justified only when the two cylinders are sufficiently apart. Generally, the interference between two cylinders at close proximity drastically changes the flow around them, produces unexpected forces and pressure distributions, and intensifies or suppresses vortex shedding. These changes of the flow pattern are systematically described and analyzed in the present work.

All the possible arrangements of two cylinders are grouped into three sections: tandem, side-by-side, and staggered. The possible flows around two circular cylinders may be classified in two categories: with and without interference. These two categories are divided by an interference boundary. The interference may be either partial, when only one cylinder is affected, or combined, when both mutually interfere.

With the advent of powerful computers, computational methods have become widely used to study fluid flow problems. The numerical solution of unsteady incompressible Navier-Stokes equations using finite difference method has been reported in numerous studies, among which a great number of results were obtained concerning flow separation from a circular cylinder.

The aim of the present work is to solve and study the problem of the fluid flow and forced convection around two circular cylinders in a Uniform Air-Stream for the case of unsteady laminar flow with Reynolds number ranging from *100* to *500*, constant heat flux dissipating from both cylinders, as well as constant wall temperature for both cylinders. Flow visualization as well as thermal fields are considered. In addition, results will be shown when the interference between the two cylinders is weak or strong. The following information is specifically required:

1. Solution of the flow field as a function of Reynolds number and the ratio between the transverse spacing between the cylinders s and the cylinder diameter d to give a numerical visualization of flow structure and to calculate pressure distribution, Strouhal number, drag coefficients and lift coefficients.
2. Solution of the thermal field to find the variation of local and average Nusselt number as a function of both pitch to diameter ratio s/d and Reynolds number.

This requires the solution of the full two-dimensional; unsteady Navier-Stokes and energy equations describing forced convection around the two cylinders. The numerical results provide detailed information about the velocity and thermal fields.

One of the facts today is the existence of many commercial CFD programs in the market. Some of these programs have simplified the process of solving CFD problems to be something like CAD or CAM problems. The reason of the wide dispersal of such codes is that the computers today are more powerful and cheaper compared with the past.

For this reason, the commercial program STAR-CD [80] from Computational Dynamics Limited was chosen. Ability and accuracy of the program for solving similar problems will be tested. The problem under consideration is to be solved with the aid of this program implementing all the experience gained from the test phase (such as solution grid, descritization method, etc.) to optimize the solution process.

The obtained results will help in understanding the relationship between the two cylinders and this will be very useful for some design aspects concerning heat exchangers and any application related to the flow around circular cylinders. Also this will answer some design related questions like the best spacing between cylinders to obtain the maximum heat transfer coefficient for a given value of Reynolds number.

As stated before, two types of thermal boundary conditions will be considered:

- The first type is the constant wall heat flux boundary condition, which mainly arises when electrical heating is to be considered.
- The second type will be the constant wall temperature boundary condition, which mainly arises when heating, or cooling is to be done using condensing or boiling fluid.

The heat transfer mode found in real applications is a combination of the two above modes and as a result, it is very important to study both of them. Although this problem is common to be found in the industry, no previous works at all are found that consider the heat transfer relation between the two cylinders as one unit with the fluid overtaking them.

All the above questions will be answered in the upcoming chapters. First of all the relation between the two cylinders keeping Reynolds number constant is to be tested. The impression got from this step is to be verified for the whole rang of Reynolds numbers under investigation. Finally, heat transfer characteristics are to be studied for the whole range of Reynolds number under consideration to represent the relationship between Nusselt number and other problem parameters (i.e. Reynolds number and pitch to diameter ration).

Chapter 2

Problem Formulation

2.1 Geometry

The geometry and the boundary conditions of the problem are given in Figure 2-1. The figure shows simply a domain of height h , length l with its third dimension (the width), which is very large compared to both h and l . The upper and lower sides of this domain represent the free stream conditions. A combination of two cylinders, each of diameter d , is centered between the upper and lower sides of the domain. The transverse spacing between the centers of cylinders is s . The center of the first cylinder is at a distance b from the entrance of the domain. The fluid used in the analysis is air with constant properties (no change with temperature). The flow is assumed laminar, incompressible and two-dimensional. The required Reynolds number is defined by choosing an appropriate combination of the entrance velocity u_∞ and the cylinder diameter d .

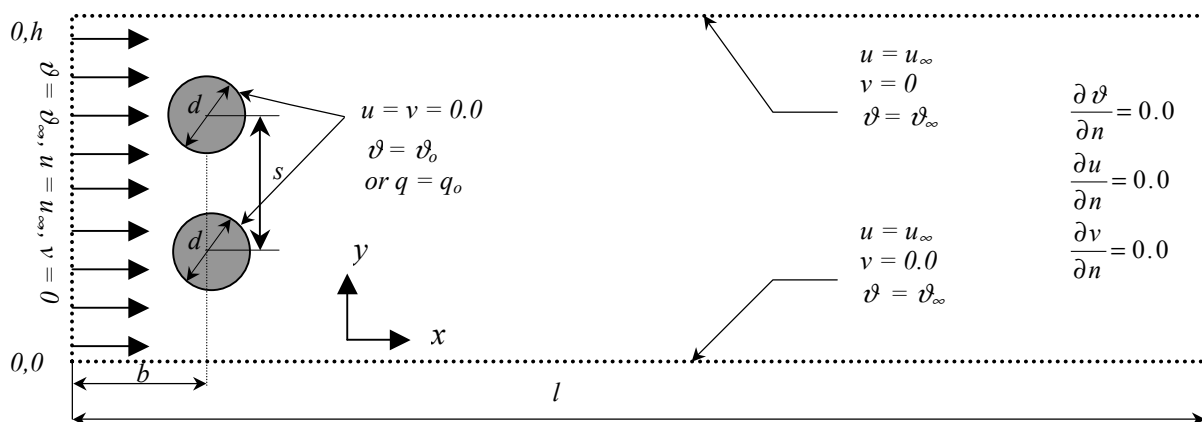


Figure 2-1 Geometry and boundary conditions of the flow around two cylinders in a channel.

2.2 Boundary and Initial Conditions

2.2.1 Inlet Boundary Condition

We assumed a free stream velocity profile at the entrance of the solution domain in the form:

$$u(0, y, t) = u_{\infty}, \quad v(0, y, t) = 0. \quad (2.1)$$

The temperature of the fluid is given to be constant at the entrance of the solution domain i.e.

$$\vartheta(0, y, t) = \vartheta_{\infty}. \quad (2.2)$$

2.2.2 Upper and Lower Boundary Conditions

The free stream boundary conditions at the upper and lower sides of the solution domain were assumed valid. This means:

$$\begin{aligned} u(x, 0, t) = u_{\infty}, \quad v(x, 0, t) = 0, \quad \vartheta(x, 0, t) = \vartheta_{\infty} \\ u(x, h, t) = u_{\infty}, \quad v(x, h, t) = 0, \quad \vartheta(x, h, t) = \vartheta_{\infty} \end{aligned} \quad (2.3)$$

At the cylinder walls, the temperature is kept constant or the wall heat flux is kept constant, and the no slip condition is applied. That is:

$$u_{cylinder\ walls}(t) = v_{cylinder\ walls}(t) = 0. \quad (2.4)$$

In case of constant wall temperature:

$$\vartheta_{cylinder\ walls}(t) = \vartheta_o. \quad (2.5)$$

In case of constant wall heat flux:

$$q_{cylinder\ walls}(t) = q_o. \quad (2.6)$$

2.2.3 Outlet Boundary Conditions

The distribution of the variables at the exit of the channel is determined by extrapolation from values on the current field points. It is assumed that the gradient of any variable is normally

alike to zero to the exit of the solution domain (zero-gradient condition). The value of any variable at the exit level is therefore equal to the value in the cell, which borders on the exit.

That means:

$$\begin{aligned}\frac{\partial u(n, y, t)}{\partial x} &= 0 \\ \frac{\partial v(n, y, t)}{\partial x} &= 0 \\ \frac{\partial \vartheta(n, y, t)}{\partial x} &= 0.\end{aligned}\tag{2.7}$$

2.2.4 Initial Conditions

At the beginning of calculations, the free stream condition is assumed, i.e. all the velocities are equal to u_∞ at first. The temperature is also assumed to be ϑ_∞ all over the domain of solution. This can be expressed as follows:

$$\begin{aligned}u(x, y, 0) &= u_\infty, & v(x, y, 0) &= 0, \\ \vartheta(x, y, 0) &= \vartheta_\infty.\end{aligned}\tag{2.8}$$

Chapter 3

Literature Review

Previous studies involving fluid flow will be reviewed first and followed by a review of studies involving heat transfer in addition to the fluid flow. After that a survey of studies involving two and more cylinders will be given.

3.1 One Cylinder

3.1.1 Fluid Flow

Steady and transient fluid flow over a fixed cylinder is a classic problem that has been extensively studied for many years.

Thom [1] gave the first successful numerical solution of the complete equations of motion in two dimensions for steady flow around a circular cylinder at $Re_D = 10$, where D is the diameter of the cylinder. Later, Thom [2] improved his numerical method by a transformation of the physical plane and obtained a solution at $Re_D = 20$ which agrees with earlier experimental results. Tomotika and Aoi [3] discussed the case of steady flow of a viscous fluid past a circular cylinder and found that two stationary eddies are always formed behind the cylinder. Further, it was found that such standing eddies are still formed even when the Reynolds number assumes very small values such as 0.05 , 0.1 , and 0.25 , in dissension to the common view that for very small Reynolds numbers, in the neighborhood of unity, the two stagnant eddies are not formed.

Allen and Southwell [6] used a relaxation technique to obtain solutions for $Re_D = 0, 1, 10, 100$, and $1,000$. They found that the length of the vortices behind the cylinder starts to decrease for $10 \leq Re_D \leq 100$. At Reynolds number of 0.16 , Taneda [7] found experimentally that the flow direction could hardly be deduced from the streamline pattern, because in the

limit of zero Reynolds number the flow past a solid body is reversible. At a Reynolds number of 1.24 , the streamline pattern clearly lost the fore-and-aft symmetry. Taneda measured the length of the standing vortex pair behind a cylinder up to $Re_D = 57.7$ and found that the downstream distance to the cores of eddies increases linearly with the Reynolds number. However, the lateral distance between the cores appears to grow more nearly as the square root of the Reynolds number.

Batchelor [8] suggested a limiting solution (Euler flow, $\nu \rightarrow 0$) with a closed-cusped wake of finite length, containing two regions with uniform vorticity associated with zero drag on the cylinder. Payne [9] obtained limiting steady-state solutions at $Re_D = 40$ and 100 by using the vorticity and velocity components as the dependent variables instead of vorticity and stream function. He carried out a numerical integration of the time dependent equations of motion at $Re_D = 40$ and at $Re_D = 100$ but did not proceed far enough to reach steady state. Kawaguti [4,5] and Apelt [10] used slightly modified versions of Thom's [1, 2] method to carry out calculations at $Re_D = 40$. Tritton [11] reported extensive data on drag coefficients for circular cylinders for $0.5 < Re_D < 100$.

Fromm and Harlow [12] solved the time-dependent flow equations past a rectangular object "cylinder" or plate in a channel. Grove et al. [13] investigated experimentally the steady separated flow past a circular cylinder. The flow was artificially stabilized with a splitter plate. It was found that the pressure coefficient at the rear (base) of the cylinder remained unchanged for $25 \leq Re_D \leq 177$, that the circulation velocity within the wake approached a nonzero limit as Re_D is increased, and that the wake length increased in direct proportion to Re_D .

Dennis and Shimshoni [14] reduced the equations of motion to a series of ordinary differential equations and solved these by a numerical method over the range of Re_D from 0.01 to 10^2 . Their results showed that the length of vortex wake behind the cylinder starts to decrease for $10 \leq Re_D \leq 100$. Acrivos et al. [15] studied the steady-state problem on the assumption that the stagnant vortex region behind a cylinder should stretch out linearly with an increase in Reynolds numbers. They were able to stabilize the wake for Reynolds numbers up to 180 by placing a splitter plate in the wake of the cylinder, as was done by Grove et al. [13]. Based on these experiments they suggested that at an infinite Reynolds number the wake bubble is viscous, that it has an infinite length and a width of the order of the cylinder diameter, and that the pressure coefficient at the rear (base) stagnation point is approximately equal to 0.45 .

Kawaguti and Jam [16] reported numerical solutions of the time-dependent equations for Re_D 10, 20, 30, 40, 50, 60, and 100. They have shown that the limiting steady-state solutions of the problem exist at $Re_D = 10, 20, 30, 40,$ and 50 , but solutions for $Re_D = 60$ and 100 were discontinued after a large time and before a steady state was reached.

A review by Roshko [17] indicates that as the $Re_D \rightarrow \infty$, there are two models of considerably different nature that have been suggested for the theoretical solution of a steady flow past a cylinder. The classical free-streamline model of Helmholtz-Kirchhoff as given in [4, 5, 8, 17, 28] gives a finite drag on the cylinder as $Re_D \rightarrow \infty$, with an open wake of infinite length and zero velocity separated from an inviscid region by free streamlines. The second concept, that of Batchelor [8], gives a limiting solution (Euler flow, $\nu \rightarrow 0$) with a closed-cusped wake of finite length, containing two regions with a uniform vorticity, associated with zero drag on the body. This result is known as D'Alembert's paradox. It seems that Batchelor was not aware of Taneda's experiments [7], which were published independently in the same year.

Acrivos et al. [18] gave further results in a later study, in support of the model in [33]. Hamielec and Raal [19] have obtained numerical solutions at Re_D up to 100. Their results also indicate a decrease in wake length as Reynolds number increases. Son and Hanratty [20] used an alternating-direction-implicit (ADI) method and symmetry of the flow in order to obtain limiting steady-state solutions of the transient problem at $Re_D = 40$ and 200. The value of the steady-state drag coefficient at $Re_D = 500$ was estimated by extrapolation. Their results showed that the length of the vortex wake behind the cylinder decreased for $200 \leq Re_D \leq 500$. Jain and Rao [22] removed the symmetry condition used by Kawaguti and Jam [16] in order to obtain numerical solutions at higher Reynolds numbers. They examined the flow at $Re_D = 40, 60, 100,$ and 200 , and found that the solutions for the unsteady problem approached those for the steady one at $Re_D = 40$ and 60 . Their results also showed that the length of the vortex wake behind the cylinder starts to decrease for $Re_D = 100$. Thoman and Szewczyk [23] solved the time-dependent equations for $1 \leq Re_D \leq 106$ and presented solutions for both stationary and rotating cylinders in that range of Reynolds numbers.

Steady-state solutions were obtained for long periods of times for $Re_D = 1$ and for $Re_D = 30$. At large Reynolds numbers, unsymmetrical disturbances were introduced after the solutions had been carried out to a certain dimensionless time. The disturbances caused alternate shedding of the vortices behind the cylinder and the formation of a vortex street. These authors besides Kawaguti and Jain [16] found it necessary to perturb the flow to promote

vortex shedding. Four techniques for such promotion used by Thoman and Szweczyk [23] included:

1. Placing the cylinder unsymmetrical in the flow field.
2. Purposely making the cylinder slightly eccentric.
3. Introducing artificial vorticity into the flow field for a small period of time.
4. Introducing a slight rotational velocity of the cylinder for a short period of time.

This suggests that steady-state solutions at high Reynolds numbers may be valid although not realizable in experiments due to the very great difficulty in isolating the flow from minute disturbances. Takami and Keller [21] have done numerical calculations of the steady problem in the range of Reynolds numbers from 1 to 60. Their results indicate linear dependence of the wake length on $Re_D < 60$.

The results of Allen and Southwell [6], Dennis and Shimshoni [14], Hamielec and Raal [19], Jam and Rao [22], and Patel [27] are in disagreement with the experiments of Taneda [7] and therefore their calculations are doubtful but may have been helpful for later investigators. Dennis and Chang [24] obtained finite-difference solutions of the equation of motion for steady incompressible flow around a circular cylinder for the range $5 \leq Re_D \leq 100$. The wake length was found to increase approximately linearly with an increase in Re_D . Collins and Dennis [25] have given an implicit and time-dependent scheme for solving the Navier-Stokes equations numerically. At Reynolds numbers higher than 100, this scheme failed to converge. At Reynolds numbers higher than 200, the divergence of the scheme occurred even earlier.

Jam and Goel [26] showed the process of shedding of vortices by computing the unsteady fluid flow around a circular cylinder at $Re_D = 200$. This was achieved by imposing the natural boundary conditions (no symmetry assumed). They obtained the shedding of the vortices by introducing some perturbation in the flow field as was done by Thoman and Szweczyk [23]. Patel [27] obtained semianalytical solutions of the impulsively started symmetrical unsteady flow past a circular cylinder for $60 \leq Re_D \leq 600$. Fornberg [29] obtained numerical solutions for steady viscous flow past a circular cylinder at Reynolds numbers up to 300. A symmetry boundary condition was imposed, as was done by Kawaguti and Jam [16], to increase stability for a much longer time.

3.1.2 Fluid Flow-Heat Transfer

Numerous studies on forced-convective heat transfer apply to a single cylinder. A single cylinder placed normal to a fluid stream was investigated experimentally by Giedt [30], where the local Nusselt numbers were determined for $7.08 \times 10^4 \leq Re_D \leq 2.19 \times 10^5$. Eckert and Soehngen [32] measured the local Nusselt number around a cylinder for $Re_D = 23$ to 597. Van der Hegge Zijnen [33] reviewed heat transfer by natural and by forced convection from horizontal cylinders to fluids. Experimental data of various origins were collected, and modified correlation formulas were derived from them.

Corns and Williams [34] conducted experiments for heated wires for $0.01 \leq Re_D \leq 140$. Their results pointed out clearly that, except at the very lowest of the Reynolds numbers, there are substantial discrepancies between experiment and results derived from theoretical models at low Reynolds numbers. These models were based on the linearization of the heat transfer equation with the external stream velocity, after the manner of Oseen. Perkins and Leppert [35] investigated experimentally a heated cylinder in a cross-flow of water and ethylene glycol for Re_D from 40 to 10^5 and Pr from 1 to 300. Kestin [42] and others [31, 37, 38, 40, 41, 44, 45, 46] studied the effect of free-stream turbulence intensity on heat transfer rate.

Most of the steady-state numerical studies were carried out for $Re_D \leq 300$, and a few included computation of heat transfer from a cylinder. Papers published on numerical calculations of heat transfer from a cylinder in steady flows at low Reynolds numbers are that of Harlow and Fromm [39], Dennis et al. [43], Jam and Goet [48], Apelt and Ledwich [49], and Ahmad and Qureshi [56]. Harlow and Fromm [39] presented a numerical study of the heat transfer in an incompressible fluid flow through a channel past a rectangular object "cylinder." Dennis et al. [43] discussed a theoretical study about a laminar forced convection in an incompressible steady fluid flow past a circular cylinder for $0.01 \leq Re_D \leq 40$. Jain and Goel [48] obtained a numerical solution of an unsteady, laminar forced convection from a circular cylinder. The Navier-Stokes equations and the energy equation were solved at Reynolds numbers 100 and 200, and Nusselt numbers were reported at those Reynolds numbers.

Apelt and Ledwich [49] studied a numerical solution of a heated circular cylinder in unsteady flows at Reynolds numbers of the range in which vortex shedding does not normally occur, i.e., $Re_D \leq 40$. Ahmad and Qureshi [56] reported an analysis of combined forced- and natural-convection (mixed-convection) heat transfer from a horizontal cylinder dissipating a uniform heat flux in air by solving the full two-dimensional, steady-state Navier-Stokes and energy

equations. Flow fields and transport results were determined in the ranges of Reynolds numbers $1 \leq Re_D \leq 60$ and the modified Grashof numbers $0 \leq Gr_D \leq 1.6 \times 10^4$.

An account of many experimental and theoretical results of forced-convection heat transfer from cylinders up to 1975 was given by Morgan [47]. Baughn et al. [53] presented experimental data for the local Nusselt number for a single cylinder, cylinders in tandem, and cylinders located in the entrance of an aligned and staggered tube bank. Local heat transfer measurements around a cylinder in an icing wind tunnel were made by Van Fossen et al. [51], Arimilli et al. [52], and Pais and Singh [54]. A horn-shaped ice accretion was formed on the forward side of the cylinder. The heat transfer results of uniform heat flux measurements, conducted by Papell [50], and by Baughn and Saniei [55], were compared directly to those of uniform surface temperature.

3.2 Two and More Cylinders

3.2.1 Fluid Flow

Unlike flow past a single cylinder, the study of flow past two cylinders was unsystematic and fragmentary. Biermann and Herrnstein [57] carried out measurements of the drag force when two circular cylinders were arranged to face the wind side by side. They expressed the results through the interference drag coefficient. This drag was zero for all spacings greater than five diameters. The interference drag increased as the spacing decreased but only down to 2.25 diameters. For smaller spacings, very odd changes occurred.

Landweber [58] undertook a photographic study of the wake behind two cylinders side by side in water. The spacings chosen were: 1.0 (cylinders in contact), 1.25, 1.5, 2.0, 2.25, 3, and 4. He observed a single vortex street for the first two spacings, “confused” *four* rows of vortices for the third, and two distinct vortex streets for the rest. He neglected the “confused 4 rows” and devoted the rest of his paper to coupled vortex streets.

Spivack [59] was the first to carry out systematic measurement of the vortex shedding frequency behind two cylinders in the side-by-side arrangement. He found for all transverse spacings, s greater than 2 diameters a single frequency in both wakes which, when reduced to Strouhal number, was the same as for the single cylinder. For transverse spacing less than 1.0, two different frequencies were recorded in both wakes. The upper frequency disappeared for

small spacings (about 1.4 dia) and only the lower one continued down to the cylinders in contact. The possible explanation for the existence of two different frequencies was due to two different wakes behind two cylinders, but why they were found in both wakes was left unexplained. A very low frequency was detected along the gap centerline (between the cylinders only) for spacings less than 1.4

Hori [60] measured the pressure distribution around two cylinders arranged one behind the other. He measured the surface pressure distribution around one of the two cylinders for various wind speeds, gaps between them and angles between the wind direction and the plane of the cylinders' axes. It was approved that there is a discontinuous change of the base pressure coefficient for the side-by-side arrangement when the spacings were 1.2 and 2.0 dia. Hori carefully verified this by adding additional experimental points in front of and behind the location of the jump, and stated: "When the flow was normal to the cylinders' axes and the gap is less than 2 diameter, there is a difference in base pressure coefficient C_{P_b} of the two cylinders, although the geometrical arrangement is symmetrical with respect to the stream."

Ishigai, et al. [61] used the Schlieren optical method and photographed the flow pattern around the two cylinders. He found that for the transverse spacing ratios 3 and 2.5 , the vortex shedding is "coupled". The vortex formation and shedding is markedly symmetric about the axis of the gap. For a transverse spacing of 2.0 dia, the vortex shedding was still coupled, but the gap flow is slightly deflected upwards. The vortex shedding becomes uncoupled and weak at a spacing of 1.5 dia and the gap flow is biased to one side. The same trend is continued at 1.25 dia. The biased flow in the gap is bistable and intermittently changes over either downwards or upwards.

Zdravkovich [62] stated that the discontinuity features of the vortex shedding observed by various authors are caused by the abrupt change from one stable flow pattern to another at the critical spacing of the two cylinders.

Although the problem is of great importance in practice, it seems that it has been somewhat neglected in numerical simulation. This is probably due to the complexity of flow configurations. The studies known to us are those of Stansby [63] who studied flow past two cylinders at different arrangements by assuming that flow was potential. Chen et al. [64] obtained unsteady solution without vortex shedding.

Li, et al. [65] developed a finite element program in order to simulate the vortex shedding behind one or two circular cylinders in tandem arrangement for $500 \leq Re$. For the case of two cylinders in tandem arrangement, one value of Reynolds number was studied ($Re = 100$).

Braun, et al. [66] examined numerically the fluid flow through a staggered array of cylinders. They have concentrated on the analysis of the physics of flow and pressure distribution in one row of cylinders and seven rows of cylinders. The numerical experiments were in transient mode at Reynolds numbers ranging from 86 to 869.

Ichioka, et al. [67] studied numerically the fluid elastic vibration of cylinder arrays. During the analysis, they studied the case of two fixed parallel cylinders (which is very similar to our case). The numerical results showed good agreement with the previous experimental results. The fact that the peaks in the lift power spectrum are in a certain range of Strouhal numbers at a transverse ratio $s/d < 2.0$ was also agreed with the phenomenon produced by Ichioka's work.

3.2.2 Fluid Flow-Heat Transfer

While there is a considerable amount of theoretical and experimental work devoted to the studies of different aspects of flow around a single cylinder, information about studies for the flow passed two parallel cylinders were very limited and mostly about the flow characteristics. No information was found that covers the heat transfer characteristics of the flow passed two cylinders. This was one of the reasons why we have decided to solve this problem.

Chapter 4

Governing Equations

4.1 Conservation Principles

Conservation laws can be derived by considering a given quantity of matter or *control mass* (CM) and its *extensive* properties, such as mass, momentum and energy. This approach is used to study the dynamics of solid bodies, where the CM (sometimes called the *system*) is easily identified. In fluid flows, however, it is difficult to follow a parcel of matter. It is more convenient to deal with the flow within a certain spatial region, we call a *control volume* (CV), rather than in a parcel of matter which quickly passes through the region of interest. This method of analysis is called the *control volume approach*.

The conservation law for an extensive property relates the rate of change of the amount of that property in a given control mass to externally determined effects. For mass, which is neither created nor destroyed in the flows of engineering interest, the conservation equation can be written:

$$\frac{dm}{dt} = 0. \quad (4.1)$$

On the other hand, momentum can be changed by the action of forces and its conservation equation is Newton's second law of motion:

$$\frac{d(m\vec{V})}{dt} = \sum f. \quad (4.2)$$

These laws are to be transformed into a control volume form. The fundamental variables will be *intensive* rather than *extensive* properties; the former are properties, which are independent

of the amount of matter considered. Examples are density ρ (mass per unit volume) and velocity \vec{V} (momentum per unit mass).

If ϕ is any conserved intensive property (for mass conservation, $\phi = 1$; for momentum conservation, $\phi = \vec{V}$ and for conservation of a scalar, ϕ represents the conserved property per unit mass), then the corresponding extensive property Φ can be expressed as:

$$\Phi = \int_{\Omega_{CM}} \rho \phi d\Omega, \quad (4.3)$$

where Ω_{CM} stands for volume occupied by the *CM*. Using this definition, the left hand side of each conservation equation for a control volume can be written:

$$\frac{d}{dt} \int_{\Omega_{CM}} \rho \phi d\Omega = \frac{d}{dt} \int_{\Omega_{CV}} \rho \phi d\Omega + \int_{S_{CV}} \rho \phi (\vec{V} - \vec{V}_b) \cdot n ds, \quad (4.4)$$

where Ω_{CV} is the *CV* volume, S_{CV} is the surface enclosing *CV*, n is the unit vector orthogonal to S_{CV} and directed outwards, \vec{V} is the fluid velocity and \vec{V}_b is the velocity with which the *CV* surface is moving. For a fixed *CV*, $\vec{V}_b = 0$ and the first derivative on the right hand side becomes a local (partial) derivative. This equation states that the rate of change of the amount of the property in the control mass, Φ , is the rate of change of the property within the control volume plus the net flux of it through the *CV* boundary due to fluid motion relative to *CV* boundary. The last term is usually called the *convective* (or sometimes, *advective*) flux of ϕ through the *CV* boundary. If the *CV* moves so that its boundary coincides with the boundary of a control mass, then $\vec{V} = \vec{V}_b$ and this term will be zero.

4.2 Mass Conservation

The integral form of the mass conservation (continuity) equation follows directly from the control volume equation, by setting $\phi = 1$:

$$\frac{\partial}{\partial t} \int_{\Omega} \rho d\Omega + \int_S \rho \vec{V} \cdot n dS = 0. \quad (4.5)$$

By applying the Gauss' divergence theorem to the convection term, one can transform the surface integral into a volume integral. Allowing the control volume to become infinitesimally small leads to a differential coordinate-free form of the continuity equation:

$$\frac{\partial \rho}{\partial t} + \text{div}(\rho \vec{V}) = 0. \quad (4.6)$$

This form can be transformed into an equation specific to a given coordinate system by providing the expression for the divergence operator in that system. The law for the Cartesian coordinates in both tensor and expanded notation may be written as follows.

$$\frac{\partial \rho}{\partial t} + \frac{\partial(\rho u_i)}{\partial x_i} = \frac{\partial \rho}{\partial t} + \frac{\partial(\rho u_x)}{\partial x} + \frac{\partial(\rho u_y)}{\partial y} + \frac{\partial(\rho u_z)}{\partial z} = 0, \quad (4.7)$$

where x_i ($i = 1, 2, 3$) or (x, y, z) are the Cartesian coordinates and u_i or (u_x, u_y, u_z) are the Cartesian components of the velocity vector \vec{V} .

4.3 Momentum Conservation

There are several ways of deriving the momentum conservation equation. One approach is to use the control volume method described above; in this method, one uses Eqs. (4.2) and (4.4) and replaces ϕ by \vec{V} , e.g. for a fixed fluid-containing volume of space:

$$\frac{\partial}{\partial t} \int_{\Omega} \rho \vec{V} d\Omega + \int_S \rho \vec{V} \vec{V} \cdot \vec{n} dS = \sum f. \quad (4.8)$$

To express the right hand side in terms of intensive properties one has to consider the forces, which may act on the fluid in a CV :

- Surface forces (pressure, normal and shear stresses and surface tension etc.);
- Body forces (gravity, electromagnetic forces, or any other forces which “act at a distance” on the fluid inside).

The surface forces due to pressure and stresses are, from the molecular point of view, the microscopic momentum flux across a surface. If these fluxes cannot be written in terms of

properties whose conservation is governed by the above equations (density and velocity), the system of equations is not closed; because there will be fewer equations than dependent variables and the solution is not possible. This possibility can be avoided by making certain assumptions. The simplest assumption is that the fluid is Newtonian; fortunately, the Newtonian model applies to many actual fluids.

For Newtonian fluids, the stress tensor \mathbf{T} , which is the molecular rate of transport of momentum, can be written:

$$\mathbf{T} = -\left(p + \frac{2}{3}\mu \operatorname{div} \vec{V}\right) \mathbf{I} + 2\mu \mathbf{D}, \quad (4.9)$$

where μ is the dynamic viscosity, \mathbf{I} is the unit tensor, p is the static pressure and \mathbf{D} is the rate of strain (deformation) tensor:

$$\mathbf{D} = \frac{1}{2} \left[\operatorname{grad} \vec{V} + (\operatorname{grad} \vec{V})^T \right], \quad (4.10)$$

where the superscript T means transpose

These two equations may be written, in index notation in Cartesian coordinates, as follows:

$$T_{ij} = -\left(p + \frac{2}{3}\mu \frac{\partial u_j}{\partial x_j}\right) \delta_{ij} + 2\mu D_{ij}, \quad (4.11)$$

$$D_{ij} = \frac{1}{2} \left(\frac{\partial u_i}{\partial x_j} + \frac{\partial u_j}{\partial x_i} \right), \quad (4.12)$$

where δ_{ij} is Kronecker symbol ($\delta_{ij} = 1$ if $i = j$ and $\delta_{ij} = 0$ otherwise). For incompressible flows, the second term in brackets in Equ. (4.11) is zero by virtue of the continuity equation. The following notation is used in the literature to describe the viscous part of the stress tensor:

$$\tau_{ij} = 2\mu D_{ij} - \frac{2}{3}\mu \delta_{ij} \operatorname{div} \vec{V}. \quad (4.13)$$

With the body forces (per unit mass) being represented by b_f , the integral form of the momentum conservation equation becomes:

$$\frac{\partial}{\partial t} \int_{\Omega} \rho \vec{V} d\Omega + \int_S \rho \vec{V} \vec{V} \cdot \vec{n} dS = \int_S \mathbf{T} \cdot \vec{n} dS + \int_{\Omega} \rho b_f d\Omega. \quad (4.14)$$

A coordinate-free vector form of the momentum conservation Equ. (4.14) is readily obtained by applying Gauss' divergence theorem to the convective and diffusive flux terms:

$$\frac{\partial(\rho \vec{V})}{\partial t} + \text{div}(\rho \vec{V} \vec{V}) = \text{div} \mathbf{T} + \rho b_f. \quad (4.15)$$

The corresponding equation for the i th Cartesian component is:

$$\frac{\partial(\rho u_i)}{\partial t} + \text{div}(\rho u_i \mathbf{v}) = \text{div} \mathbf{t}_i + \rho b_{f_i}. \quad (4.16)$$

Since momentum is a vector quantity, the convective and diffusive fluxes of it through a CV boundary are the scalar products of second rank tensors ($\rho \vec{V} \vec{V}$ and \mathbf{T}) with the surface vector $\vec{n} dS$. The integral form of the above equations is:

$$\frac{\partial}{\partial t} \int_{\Omega} \rho u_i d\Omega + \int_S \rho u_i \mathbf{v} \cdot \vec{n} dS = \int_S \mathbf{t}_i \cdot \vec{n} dS + \int_{\Omega} \rho b_{f_i} d\Omega. \quad (4.17)$$

where:

$$\mathbf{t}_i = \mu \text{grad} u_i + \mu (\text{grad} \mathbf{v})^T \cdot \mathbf{i}_i - \left(p + \frac{2}{3} \mu \text{div} \mathbf{v} \right) \mathbf{i}_i. \quad (4.18)$$

Here b_i stands for the i th component of the body force, superscript T means transpose and \mathbf{i}_i is the Cartesian unit vector in the direction of the coordinate x_i . In Cartesian coordinates, one can write the above expression as:

$$\mathbf{t}_i = \mu \left(\frac{\partial u_i}{\partial x_j} + \frac{\partial u_j}{\partial x_i} \right) \mathbf{i}_j - \left(p + \frac{2}{3} \mu \frac{\partial u_j}{\partial x_j} \right) \mathbf{i}_i. \quad (4.19)$$

4.4 Conservation of Scalar Quantities

The integral form of the equation describing conservation of a scalar quantity, ϕ , is analogous to the previous equations and reads:

$$\frac{\partial}{\partial t} \int_{\Omega} \rho \phi d\Omega + \int_S \rho \phi \vec{V} \cdot \vec{n} dS = \sum f_{\phi} , \quad (4.20)$$

where f_{ϕ} represents transport of ϕ by mechanisms other than convection and any sources or sinks of the scalar. Diffusive transport is always present (even in stagnant fluids), and it is usually described by a gradient approximation, e.g. *Fourier's law* for heat diffusion and *Fick's law* for mass diffusion:

$$f_{\phi}^d = \int_S \Gamma \text{grad } \phi \cdot \vec{n} dS . \quad (4.21)$$

Where Γ is the diffusivity for the quantity ϕ .

If $\phi = h$ (enthalpy), the energy equation can be written as:

$$\frac{\partial}{\partial t} \int_{\Omega} \rho h d\Omega + \int_S \rho h \vec{V} \cdot \vec{n} dS = \int_S k \text{grad } \vartheta \cdot \vec{n} dS + \int_{\Omega} (\vec{v} \cdot \text{grad } p + \mathbf{S} \cdot \text{grad } \vec{v}) d\Omega + \frac{\partial}{\partial t} \int_{\Omega} p d\Omega . \quad (4.22)$$

Where ϑ is the temperature, k is the thermal conductivity, $k = \mu c_p / Pr$, and \mathbf{S} is the viscous part of the stress tensor, Pr is the Prandtl number and c_p is the specific heat at constant pressure. The source term represents work done by pressure and viscous forces; this term may be neglected in incompressible flows. A further simplification is achieved by considering a fluid with constant specific heat. In this case, a convection/diffusion equation for the temperature becomes:

$$\frac{\partial}{\partial t} \int_{\Omega} \rho \vartheta d\Omega + \int_S \rho \vartheta \vec{v} \cdot \vec{n} dS = \int_S \frac{\mu}{Pr} \text{grad } \vartheta \cdot \vec{n} dS . \quad (4.23)$$

It is useful to write the conservation equations in a general form, as all of the above equations have common terms. The discretization and analysis can then be carried out in a general manner; when necessary, terms peculiar to an equation can be handled separately.

The integral form of the generic conservation equation will be:

$$\frac{\partial}{\partial t} \int_{\Omega} \rho \phi \, d\Omega + \int_S \rho \phi \, v \cdot n \, dS = \int_S \Gamma \, \text{grad } \phi \cdot n \, dS + \int_{\Omega} q_{\phi} \, d\Omega . \quad (4.24)$$

Where q_{ϕ} is the source or sink of ϕ . The coordinate-free vector form of this equation is:

$$\frac{\partial(\rho \phi)}{\partial t} + \text{div}(\rho \phi \, v) = \text{div}(\Gamma \, \text{grad } \phi) + q_{\phi} . \quad (4.25)$$

In Cartesian coordinates and tensor notation, the differential form of the generic conservation equation is:

$$\frac{\partial(\rho \phi)}{\partial t} + \frac{\partial}{\partial x_j}(\rho u_j \phi) = \frac{\partial}{\partial x_j} \left(\Gamma \frac{\partial \phi}{\partial x_j} \right) + q_{\phi} . \quad (4.26)$$

In the next chapter, the numerical methods used to solve the previous conservation equations will be presented. It should be noticed that the solution Code STAR-CD uses the coordinate – free vector form of the conservation equations. This is because of the ability of the program to use a general mesh system, i.e. the program can simulate any solution domain required. The fact that we gave the conservation equations here in the Cartesian coordinates is only to give an example of the form of these equations when using this type of coordinates. For more details, refer to the methodology part of the STAR-CD manual [80].

Chapter 5

Numerical Solution of the Governing Equations

5.1 General Formulation

The differential equations governing the conservation of mass, momentum and energy within the fluid presented in the previous chapter were discretized by the finite volume (FV) method [69, 70, 71]. Thus, they are first integrated over the individual computational cells and over a finite time increment, in the case of transient problems and then approximated in terms of the cell-centered nodal values of the dependent variables. This approach has the merit, amongst others, of ensuring that the discretized forms preserve the conservation properties of the parent differential equations.

For the purposes of the FV discretization, it is convenient to work with the following general coordinate-free form of the conservation equations:

$$\frac{\partial(\rho\phi)}{\partial t} + \text{div}(\rho\phi v) = \text{div}(\Gamma_\phi \text{grad}\phi) + q_\phi \quad (5.1)$$

An integral form of this equation may be written as:

$$\frac{\partial}{\partial t} \int_\Omega \rho\phi d\Omega + \int_S \rho\phi v \cdot d\vec{S} = \int_S \Gamma_\phi \text{grad}\phi \cdot d\vec{S} + \int_\Omega q_\phi d\Omega . \quad (5.2)$$

If Ω and S are, respectively, taken to be the volume Ω_p and discrete faces S_j ($j = 1, N_f$) of a computational cell, (see Figure 5-1) Equ. (5.2) becomes:

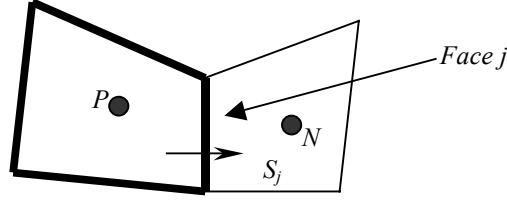


Figure 5-1 Illustration of typical cell with centered node P and neighbor cell with centered node N

$$\frac{\partial}{\partial t} \int_{\Omega_p} \rho \phi d\Omega + \sum_j \int_{S_j} (\rho \phi v - \Gamma_\phi \text{grad } \phi) \cdot d\vec{S} = \int_{\Omega} q_\phi d\Omega . \quad (5.3)$$

$$T_1 \qquad T_2 \qquad T_3$$

To solve the previous equation numerically, approximations must be done. Thus, the first term T_1 of the above form is discretized as:

$$T_1 \approx \frac{(\rho \phi \Omega)_p^n - (\rho \phi \Omega)_p^o}{\delta t} . \quad (5.4)$$

where the superscripts o and n refer to ‘old’ and ‘new’ time levels, respectively, separated by an interval δt .

The second term of Equ. (5.3) is split into the separate contributions C_j and D_j due to convection and diffusion, respectively, and each is expressed in terms of average values over cell faces, denoted by $(\)_j$:

$$T_2 \approx \sum_j (\rho v \phi \cdot \vec{S})_j - \sum_j (\Gamma \text{grad } \phi \cdot \vec{S})_j \equiv \sum_j C_j - \sum_j D_j . \quad (5.5)$$

The diffusion terms D_j are approximated by face-centered expressions of the form

$$D_j \approx \Gamma_{\phi,j} \left[f_j^l (\phi_N - \phi_P) + \left\{ \overline{\text{grad } \phi} \cdot \vec{S} - f_j^l \overline{\text{grad } \phi} \cdot \vec{d}_{PN} \right\}_j \right] . \quad (5.6)$$

where the first term in the brackets represents the normal diffusion between P and the neighboring cell-centered node N (see Fig. 5-1) and the second term within the curly brackets is the cross-diffusion. Terms f_j are geometrical factors, \vec{d}_{PN} is the distance vector between P and N , and $\Gamma_{\phi,j}$ is the (interpolated) face diffusivity.

The approximation of the convective terms C_j is given in the next section entitled “spatial flux discretization”.

The third term, T_3 , of Equ. (4.3) may in general contain components representing sources or sinks of the transported property, as well as additional flux terms; the exact form depends on the dependent variable and circumstances. Fluxes and other gradient-containing terms are approximated in a similar fashion to the C_i and D_j , while non-gradient quantities are evaluated using the cell-centered nodal quantities. For convenience, the result of this process is written in the general quasi-linear form

$$T_3 = S_1 - S_2 \phi_p. \quad (5.7)$$

5.2 Spatial Flux Discretization

The manner in which the convective and diffusive fluxes are expressed in terms of nodal ϕ values is one of the key factors determining accuracy and stability, for both steady-state and transient calculations. At the high Reynolds numbers often encountered in practice, the choice of convective flux approximation is particularly important.

There are essentially two main classes of convective flux approximation in widespread use, namely:

1. ‘Low-order’ schemes, which characteristically generate forms of discretized equation that are easy to solve, produce solutions which obey the expected physical bounds, but sometimes give rise to smearing out of gradients. The latter effect has come to be known as ‘numerical diffusion’ [72,73]. This is a form of truncation error that diminishes, as the grid is refined, but at an increased cost of calculation.
2. ‘Higher-order’ schemes, which had better preserved steep gradients, but may result in equations that are more difficult to solve (in extreme cases, may provoke numerical instabilities) and/or have solutions exhibiting non-physical spatial oscillations (‘wiggles’). These oscillations may, in some cases, lead to spurious values, e.g. negative species concentration or turbulent kinetic energy. This phenomenon is often termed ‘numerical dispersion’ [74]. It can be diminished too by grid refinement or by using monotone schemes (e.g. a blending methodology).

For this purpose, the C_j factors defined in Equ. (5.5) are written as

$$C_j = F_j \phi_j. \quad (5.8)$$

and

$$F_j = (\rho \vec{u}_r \cdot \vec{S})_j. \quad (5.9)$$

is the mass flux through face J where $\vec{u}_{r,j}$ is the interpolated velocity at the centerline of face j whose area is \vec{S}_j . The average value at the face ϕ_j is effectively interpolated from selected nodal values in accordance with the scheme used. The face values of auxiliary properties, such as ρ and Γ are obtained by interpolation, usually linear.

5.3 Temporal Discretization

As already noted, the FV equation applies over an arbitrary time increment δt spanning the ‘old’ and ‘new’ time levels. Two methods are available for temporal discretization. The first one is the fully implicit scheme. The second one is the second order Crank-Nicholson scheme.

5.3.1 Fully Implicit

Under this formulation, the fluxes prevailing over the time interval are calculated from the

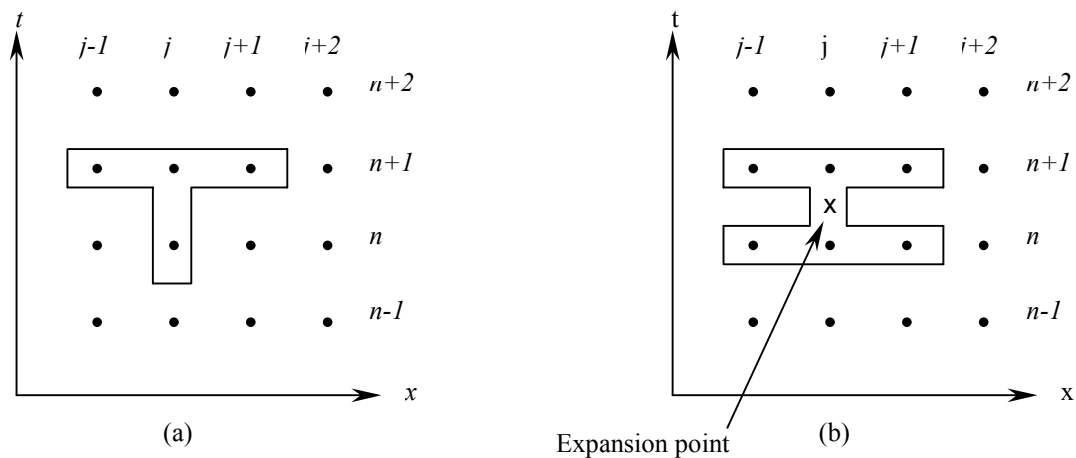


Figure 5-2 Difference ‘molecules’ for temporal discretization schemes.

new time-level values of the variables. The difference scheme for a one-dimensional situation is illustrated in Figure 5-2 (a)

As is well known [75], this practice avoids a stability-related time step restriction inherent in the otherwise attractive explicit approach, which becomes particularly onerous in regions of small mesh spacing and velocity or diffusion rate.

5.3.2 Crank-Nicholson

Whereas the fully implicit scheme is first-order accurate in time, the Crank-Nicholson scheme has a truncation error of order δt^2 and is hence second-order accurate in time. The difference scheme for this method is illustrated in Figure 5-2 (b) for a one-dimensional situation. The point $n+1/2, j$ shown in the figure is used as the expansion point for the second-order formulation. The scheme is however liable (like all other higher-order difference schemes) to generate unbounded extrema (over- and under-shots). This trend can be ameliorated by the use of smaller δt or by blending the scheme with the bounded fully implicit scheme using a manually selected blending factor.

5.4 Convective Flux Formulation

The formulation of Equ. (5.8) is valid for the default fully implicit scheme and assumes that the fluxes are obtained at the new time level, i.e.

$$C_j = F_j^{n+1} \phi_j^{n+1}. \quad (5.10)$$

Under the Crank-Nicholson scheme the convection flux is discretized as

$$C_j \equiv \frac{1}{2} \left(F_j^{n+\frac{1}{2}} \phi_j^{n+1} + F_j^{n+\frac{1}{2}} \phi_j^n \right), \quad (5.11)$$

where ϕ_j^{n+1} ϕ_j^n are interpolated at the cell faces according to the spatial discretization schemes described in the following section

$F_j^{n+\frac{1}{2}}$ is the mass flux, evaluated at time level $n+\frac{1}{2}$

The expression used for mass flux is:

$$F_j^{n+\frac{1}{2}} \equiv \frac{1}{2} (F_j^{n+1} + F_j^n). \quad (5.12)$$

As in the spatial central differencing (CD) scheme discussed on the next page, the Crank-Nicholson scheme produces lower numerical diffusion, but can be dispersive. Hence, an option is provided to blend it with the fully implicit scheme, in which case the convection flux is given by

$$C_j = F_j^{BD} [0.5 \gamma \phi_j^n + (1 - 0.5\gamma) \phi_j^{n+1}]. \quad (5.13)$$

and

$$F_j^{BD} = 0.5 \gamma F_j^n + (1 - 0.5\gamma) F_j^{n+1}. \quad (5.14)$$

It can be seen that for $\gamma = 1$, Eqs. (5.13) and (5.14) result in the Crank-Nicholson scheme of Equ. (5.11), whereas for $\gamma = 0$ they result in the fully implicit scheme of Equ. (5.10).

5.4.1 Low-Order Spatial Discretization Schemes

5.4.1.1 Upwind differencing (UD)

This low (first)-order scheme selects the nearest upwind neighbor value for ϕ (see Figure 5-3), thus:

$$C_j^{UD} \equiv F_j \begin{cases} \phi_p & , & F_j \geq 0 \\ \phi_{N+} & , & F_j < 0 \end{cases} \quad (5.15)$$

This form of interpolation preserves the correct physical bounds on ϕ under all conditions, but can lead to numerical diffusion [72,73].

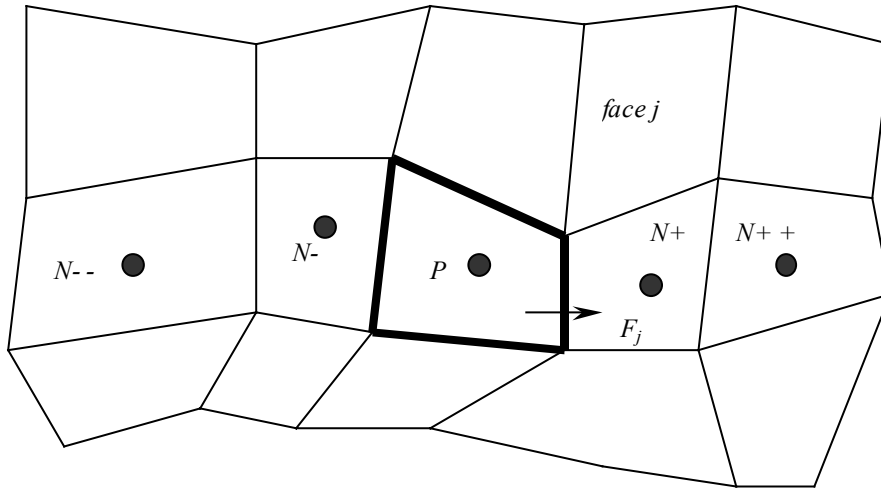


Figure 5-3 Node labeling convention for flux discretization.

5.4.2 Higher-Order Spatial Discretization Schemes

5.4.2.1 Linear upwind differencing (LUD)

This is a specially adapted; second-order accurate scheme formulated for non-structured meshes and derived from a scheme originally proposed for structured meshes [76]. It results in less numerical smearing than the UD scheme, but can produce solutions that are outside the physical bounds on ϕ (i.e. numerical dispersion).

5.4.2.2 Central differencing (CD)

The CD scheme, which is also second-order, simply interpolates linearly on nearest neighbor values, irrespective of flow direction, giving

$$C_j^{CD} = F_j [f_+ \phi_p + (1 - f_+) \phi_{N+}]. \quad (5.16)$$

where f_+ is the interpolation factor.

This scheme also produces less numerical diffusion, but can be dispersive [74].

5.4.2.3 Quadratic upstream interpolation of convective kinematics (QUICK)

This is a third-order-scheme which fits a parabola through two points upstream and one point downstream to get an interpolated value (see Figure 5-3), giving:

$$C_j^{QUICK} = F_j \begin{cases} f_- \phi_{N-} + f_+ \phi_{N+} + (1 - f_- - f_+) \phi_p & , \quad F_j \geq 0 \\ f_{++} \phi_{N++} + f_+ \phi_{N+} + (1 - f_+ - f_{++}) \phi_p & , \quad F_j < 0 \end{cases} \quad (5.17)$$

where f_- , f_+ and f_{++} are quadratic interpolation factors.

5.5 Final FV Equations

The final form of the discrete finite volume equation is obtained by substituting the various approximated terms back into Equ. (5.3) and then invoking the discretized continuity equation, which can be written as:

$$\frac{(\rho \Omega)^n - (\rho \Omega)^o}{\delta t} + \sum F_j = 0. \quad (5.18)$$

The F_j terms in the above equation are at time level $n+1$ for the fully-implicit scheme and at time level $n+1/2$ for the Crank-Nicholson scheme, as given by Equ. (5.12). For a blended scheme, the correct expression for these terms is given by Equ. (5.14).

The result, in its most compact form, is

$$A_p \phi_p^n = \sum_m A_m \phi_m^n + s_1 + B_p \phi_p^o. \quad (5.19)$$

where:

- A_m represents the effects of convection and/or diffusion
- The summation is over all neighbor nodes used in the flux discretization
- $B_p \equiv (\rho V)^o / \delta t$.

And

$$A_p \equiv \sum_m A_m + s_2 + B_p. \quad (5.20)$$

There exists an equation such as Equ. (5.19) for every computational cell (suitably modified, where necessary, to incorporate boundary conditions).

5.6 Solution Algorithms

Two different solution algorithms were used to solve the algebraic finite-volume Equ. (5.19) resulting from the discretization practices previously described. The SIMPLE algorithm was used to solve the steady state problem while the PISO algorithm was used for the transient one. They all have certain features in common, which described here before the individual algorithms are presented. The shared features are:

All employ forms of predictor-corrector strategy, enabled by the use of operator splitting, to temporarily decouple the flow equations from each other so that they can be solved sequentially.

Continuity is enforced with the aid of an equation set for pressure, which derived by combining the FV momentum and mass conservation equations. The solution sequence involves a predictor stage, which produces a provisional velocity field derived from the momentum equations and a provisional pressure distribution. The provisional fields are then refined in the corrector stage(s) by demanding simultaneous satisfaction, to some approximation, of both momentum and continuity balance.

In iterative calculations to the steady state, the above sequence is repetitively executed, with embedded updating of field- dependent coefficient arising from coupling and nonlinearity, until the solution is reached. Under-relaxation is employed as a stabilizing measure in this process. Within the sequence, the operator-split equation sets involve, at any stage, only one of the field variables, i.e. the vector set of unknowns, is split into a sequence of scalar sets. The algebraic equation sets are solved by iterative means, although this is not an essential practice.

5.6.1 The PISO Algorithm

The intention here is to convey the essence of PISO without burdening the explanation with the many detailed issues that are involved in its implementation in the complex circumstances of the commercial program STAR-CD from Computational Dynamics Limited. Accordingly,

the algorithm is first outlined in the context of a fixed Cartesian mesh aligned with the Cartesian velocity directions, as in its original formulation [77]. Following this, mention is made of the nature of the modifications and extensions made for the general mesh system and flow conditions of the commercial program STAR-CD.

5.6.1.1 Working equations

For the presentation purpose, the FV momentum equations are extracted from the general transport Equ. (5.19) in the form

$$A_P u_{i,p}^n = H(u_{i,m}^n) + B_P^o u_{i,p}^o + s_1 + D_P (p_{N+}^n - p_{N-}^n). \quad (5.21)$$

Where

$$H(u_{i,m}) \equiv \sum_m A_m u_{i,m}. \quad (5.22)$$

The last term in Equ. (5.21) is the FV approximation to the pressure gradient $\partial p / \partial x_i$, D_P being a geometric coefficient (see Figure 5-4).

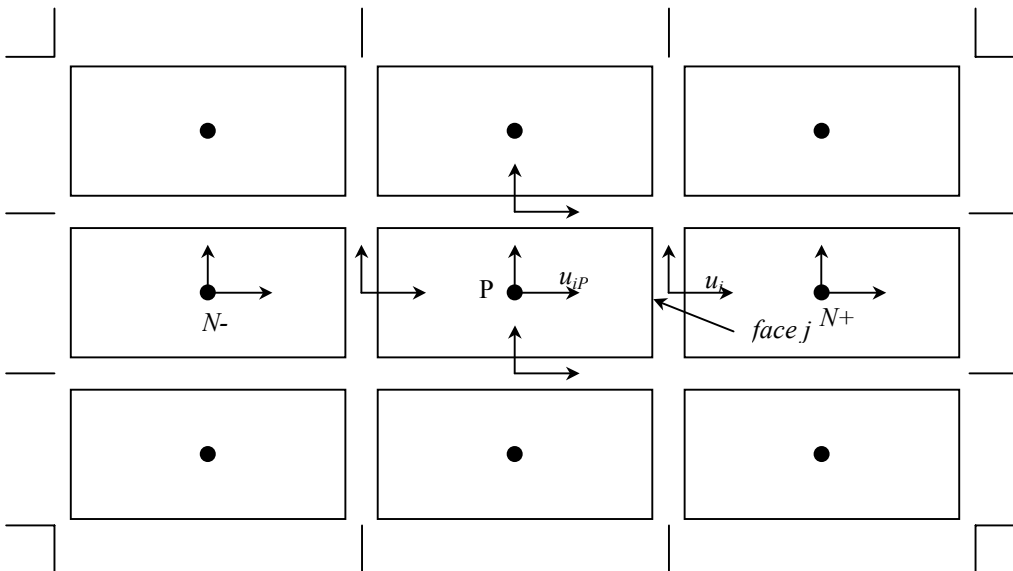


Figure 5-4 Arrangement of variables and notation for PISO implementation on Cartesian mesh.

The FV continuity Equ. (5.18) is written here as:

$$B_p^n - B_p^o + \sum_j (\rho^n u_j^n S_j) = 0. \quad (5.23)$$

where u_j are the velocities normal to the cell faces and S_j are the corresponding face areas.

In the collocated variable arrangement, the face velocities u_j need to be expressed in terms of the nodal velocities (in order to calculate the mass fluxes) and neighboring pressures (to allow formulation of a suitable pressure equation). This is done by assembling a cell-face momentum equation of the form

$$\overline{A_p} u_j^n = \overline{H}(u_{i,m}^n) + \overline{B_p^o} u_{i,p}^o + \overline{s_1} + \overline{D_p}(p_p^n - p_{N+}^n). \quad (5.24)$$

where the over bars denote a form of averaging on the nodal momentum coefficients appearing under them. This equation, when substituted into the continuity relation (5.23), yields a pressure equation of the form

$$A_p p_p^n = \sum_m A_m p_m^n + s_1. \quad (5.25)$$

where the 'source' term s_1 is a function of the nodal velocity fields u_i^n , u_i^o and other quantities. Thus, an equation set is produced from which the pressure may be calculated.

5.6.1.2 Solution sequence

Starting from initial values ϕ^o of the variable fields, PISO advances through a time increment δt in the following sequence of steps.

1. **Predictor stage.** Eqs. (5.21) are assembled and solved in the following operator-split form for the provisional nodal velocity field $u_i^{(1)}$:

$$A_p u_{i,p}^{(1)} = H(u_{i,m}^{(1)}) + B_p^o u_p^o + s_1 + D_p(p_{N+}^{(0)} - p_{N-}^{(0)}). \quad (5.26)$$

where $p^{(0)}$ corresponds to the pressure field at the start of the time step.

Following the solution of this equation, obtained by an iterative method, the provisional face velocities $u_j^{(1)}$ are calculated via Equ. (5.24), with the u_i^n and p^n replaced by $u_i^{(1)}$ and p^o , respectively.

2. **First corrector stage.** The operative nodal momentum equation is now taken to be

$$A_p u_{i,p}^{(2)} = H(u_{i,m}^{(1)}) + B_p^o u_p^o + s_1 + D_p (p_{N+}^{(1)} - p_{N-}^{(1)}). \quad (5.27)$$

and the face momentum equations are likewise approximated by replacing u_i^n and p in Equ. (5.24) by $u_i^{(2)}$ and $p^{(1)}$, respectively. Correspondingly, the pressure equation in its approximated form reads

$$A_p p_p^{(1)} = \sum_m A_m p_m^{(1)} + s_1. \quad (5.28)$$

where s_1 is now a function of the (known) nodal velocities $u_i^{(1)}$ and $u_i^{(o)}$.

Accordingly, these equations can be solved (here again by iteration) for the $p^{(1)}$ field, following which $u_i^{(2)}$, and $u_j^{(2)}$, can be obtained from Equ. (5.27) and its face counterparts. The resulting solution approximates that of the original Eqs. (5.21) and (5.23).

3. **Additional corrector stages.** Further correctors are performed in the same manner as the first one, using the generalized equations

$$A_p u_{i,p}^{(q+1)} = H(u_{i,m}^{(q)}) + B_p^o u_p^o + s_1 + D_p (p_{N+}^{(q)} - p_{N-}^{(q)}). \quad (5.29)$$

$$A_p p_p^{(q)} = \sum_m A_m p_m^{(q)} + s_1, \quad (5.30)$$

where $q = 1, 2, \dots$ is the corrector level. Note that the coefficients A_p are held constant. The solutions from the successive stages represent increasingly better approximations to the solution of the original equations, i.e. $u^{(q+1)}$ and $p^{(q+1)}$ tend towards u^n and p^n with increasing q .

After completion of the required number of correctors, judged according to practices described below, the solution produced is taken as the starting field for the next time step and

the sequence is repeated from Stage 1. If the calculation of scalar fields such as the temperature is required, it is performed in further steps executed after the final flow corrector.

In the original version of PISO [77], the recommendation was to perform just two correctors, on the basis that the splitting error at this stage is of order δt^2 as compared with the order δt truncation error. However, in STAR-CD, the number of correctors executed is not predetermined; rather, it is judged from an internal measure of the splitting error. This enhances the accuracy and reliability of the algorithm and is necessary if the scalar fields are strongly coupled to the flow.

The solution of the flow equations on the general form of mesh employed in STAR-CD is considerably more involved than for the Cartesian arrangement, for several reasons. First and foremost, the pressure calculation is complicated by the presence of additional pressure gradient terms in the momentum equations. The full expressions bear some similarity to the discretized diffusion flux expression given by Equ. (5.25) and the fact that the cell face mass fluxes F_i depend on all three Cartesian velocity components. Collectively, these features result in an extended form of pressure equation, the efficient solution of which has required extensive alterations to the PISO algorithm. For more detailed refer to STAR-CD User's manual [80].

Chapter 6

Benchmarking Computations

6.1 The Benchmark Problem

Before using any new commercial program, one must be nearly sure that this program is capable of satisfying the following conditions:

- It must solve a standard-problem (benchmark), which is similar to the problem under consideration.
- The solution of the standard-problem must be nearly right, in order to accept the solution of the new problem.

For benchmarking purpose, the work of Schäfer et al. [78] concerning the flow around a circular cylinder in a channel is considered. This work gives a very good example for benchmarking purposes because it shows many results for the same problem obtained with different numerical techniques. In addition, it delivers upper and lower bounds for the values representing the benchmarking which make it easy to control the new code.

6.2 Geometry and Boundary Conditions of the Problem

The geometry and the boundary conditions are given in Figure 6-1.

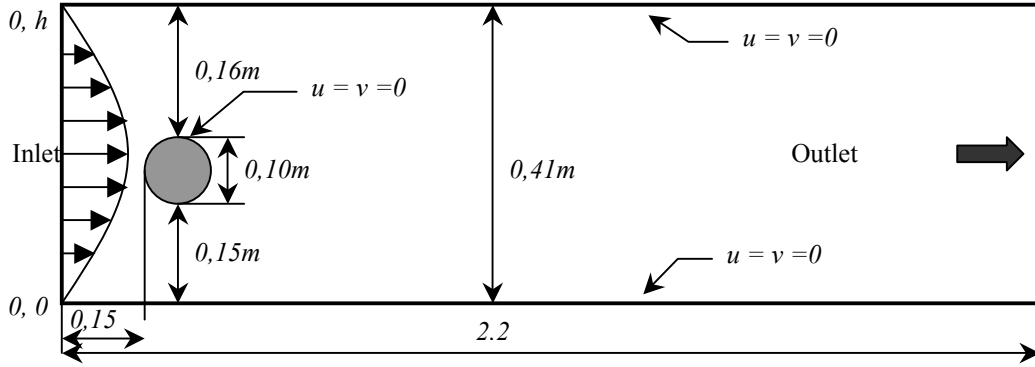


Figure 6-1 Geometry and boundary conditions of the benchmark test.

Some definitions are introduced to specify the values, which have to be computed. $h = 0.41$ m is the channel height and $d = 0.1$ m is the cylinder diameter. The Reynolds number is defined

by $Re = \frac{\bar{u} d}{\nu}$ with the mean velocity $\bar{u}(t) = 2u(0, h/2, t)/3$. The drag and lift forces are:

$$F_D = \int_S \left(\rho \mathbf{v} \frac{\partial \vec{V}_t}{\partial n} n_y - P n_x \right) dS. \quad (6.1)$$

$$F_L = \int_S \left(\rho \mathbf{v} \frac{\partial \vec{V}_t}{\partial n} n_x - P n_y \right) dS. \quad (6.2)$$

With the following notations: circle S, normal vector n on S with x-component n_x and y-component n_y . The drag and lift coefficient are:

$$c_D = \frac{2F_D}{\rho \bar{u}^2 d}. \quad (6.3)$$

$$c_L = \frac{2F_L}{\rho \bar{u}^2 d}. \quad (6.4)$$

In Eqs. (6.3) and (6.4) it is assumed that the width of the channel is 1.0.

The length of recirculation is $L_a = x_r - x_e$ where $x_e = 0.25$ m is the x-coordinate of the end of the cylinder and x_r is the x-coordinate of the end of the recirculation area. As a further reference value the pressure difference $\Delta P = \Delta P(t) = P(x_a, y_a, t) - P(x_e, y_e, t)$ is defined, with the front and end point of the cylinder $(x_a, y_a) = (0.15, 0.2)$ and $(x_e, y_e) = (0.25, 0.2)$, respectively.

6.3 Test Cases

The range of testing will be expanded to cover both steady and unsteady state flow (although the main problem is unsteady). It was thought that this makes the testing process more difficult and hence increases the program's reliability to solve the main problem with an acceptable accuracy. It helps also in getting the necessary experience needed for the main problem (grid design, discretization method, ...etc.).

6.3.1 Case a) Steady Flow

The in-flow condition is:

$$u(0, y) = \frac{4u_m y(h-y)}{h^2}, \quad v=0. \quad (6.5)$$

with $u_m = 0.3$ m/s, yielding the Reynolds number $Re = 20$. The following quantities should be computed: drag coefficient c_D ; lift coefficient c_L , length of recirculation zone L_a and pressure difference ΔP

6.3.2 Case b) Unsteady Flow

The inflow condition is:

$$U(0, y, t) = \frac{4u_m y(h-y)}{h^2}, \quad v=0. \quad (6.6)$$

with $u_m = 1.5$ m/s, yielding the Reynolds number $Re = 100$. The following quantities should be computed: drag coefficient C_D , and lift coefficient C_L as function of time for one period $[t_o, t_o + 1/f]$ (with $f = f(C_L)$ is the frequency of the lift coefficient), maximum drag coefficient $C_{D \max}$, maximum lift coefficient $C_{L \max}$, and pressure difference $\Delta P(t)$ at $t = t_o + 1/2f$. The initial data ($t = t_o$) should correspond to the flow state with $C_{L \max}$.

6.4 Results

6.4.1 Case a) Steady Flow

6.4.1.1 The numerical results

If the configuration were fully symmetric, the steady flow would yield zero lift force on the cylinder. Due to the asymmetry, there is a small lift force, as the flow rate is different above and below the cylinder. Figure 6-2 shows the velocity vectors diagram of the flow around the cylinder.

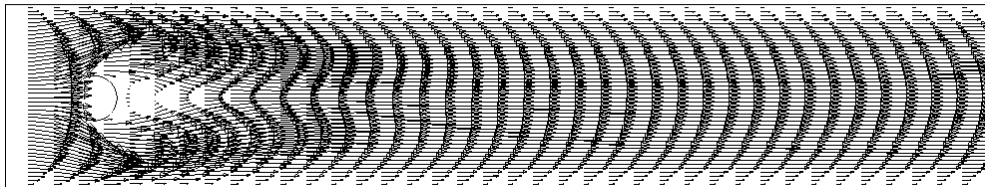


Figure 6-2 Velocity vectors in the laminar 2D flow around a circular cylinder in a channel.

As seen in the figure, the wake behind the cylinder seems to be symmetric about the gap axes, although the cylinder is not in the center of the channel. The effect of the presence of the cylinder vanishes at about 10 diameters behind the cylinder and the velocity distribution retains its parabolic shape.

Table 6-1 shows the results obtained from STAR-CD compared with the results found in [78]. It is clear that the results lay within the bounds of the benchmark results. In addition, the memory capacity and the calculation time were both acceptable. The conversion of the program was noticeably fast. It required only 1000 iterations to reach a change in the weighted residuals less than 10^{-5} , which was the conversion criterion of the program.

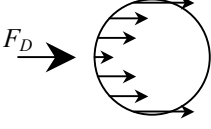
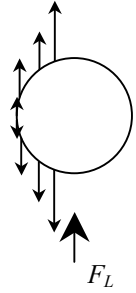
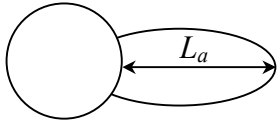
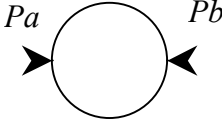
	C_D	C_L	L_a	ΔP
Definition	 $c_D = \frac{2F_D}{\rho u^2 d}$	 $c_L = \frac{2F_L}{\rho u^2 d}$	 $L_a = x_r - x_e$	 $\Delta P = \Delta P(t) = P(x_a, y_a, t) - P(x_e, y_e, t)$
Upper bound [78]	5.5700	0.0104	0.0842	0.1171
Lower bound [78]	5.5900	0.0110	0.0852	0.1176
Current results	5.5842	0.0114	0.0842	0.1172

Table 6-1 Results for the steady test case compared with the benchmark results.

6.4.1.2 The gained experience during this test phase

It took effort and too many trails to achieve these results. The affecting parameters that control the accuracy of the solution could be summarized as follows:

6.4.1.2.1 The solution grid

When constructing the mesh, the following parameters found to be very important:

- The construction of the surface of the cylinder should be done with a sufficient number of faces to get an approximate cylindrical contour with acceptable accuracy. It was found that this parameter is very important to get accurate solution. For example, Niedergesäß [79] used a structured grid and took only 16 faces to define the cylindrical contour, and as a result, his computations deviated from the benchmark values of [78] by a factor of 7 % although a fine net was used to cover the solution domain (12760 cells). The best C_D he

could get was 5,87704 which located outside the bounds defined by [78]. In order to obtain results within the prescribed benchmark, a much bigger number of cells should be used to define the cylindrical contour. To overcome this difficulty, an unstructured mesh was adapted to give an acceptable cylindrical contour, and in the same time keeps the total number of cells to a moderate value. With the aid of this unstructured grid, we could use 240 faces to define the cylinder's surface with a total number of cells of about 27000. Without using of such a grid the number of cells would be more than 100000, which exceeds the limits of the used computer.

- The grid must be fine near the walls where the gradient of the velocities is very high. This condition could be satisfied easily using a non-linear mesh distribution.
- All the calculations should be done using the double precision procedure. This was the only way to get inside the bounds defined by [78]
- The maximum number of iterations assigned to solve the momentum equations should not be less than 100, while the number assigned to solve the pressure correction equation should be 10 times this value (i.e. 1000)

Figure 6-3 illustrates a sample unstructured mesh (the actual one used is finer but this one is only for demonstration purpose).

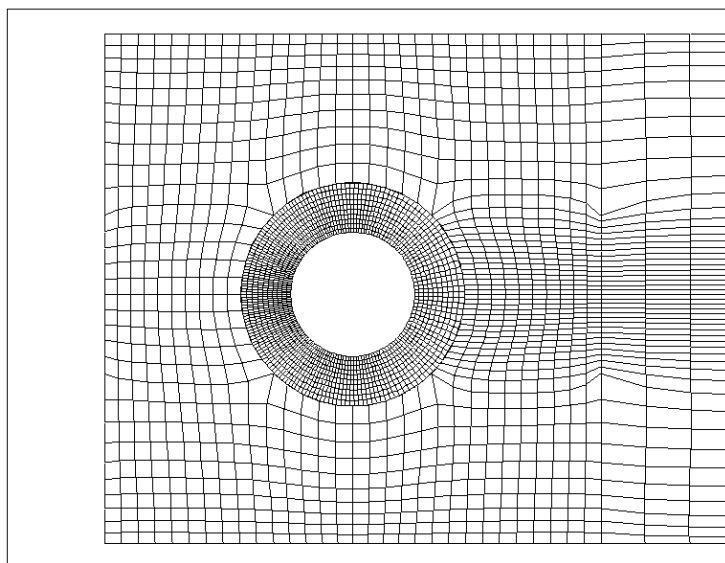


Figure 6-3 Part of sample unstructured mesh used to define the test-problem geometry.

6.4.1.2.2 The discretization scheme

All the discretization schemes available in STAR-CD [80] have been tested. The only one, which gave us acceptable results, was the QUICK scheme described by Equ. (5.17). It really needs more computational time compared with the other schemes, but it is worth the time because the other schemes did not give accurate enough results.

6.4.1.3 Benchmark Test Extension

6.4.1.3.1 Steady flow edge-Reynolds number.

After this stage, an extended benchmark test was considered. The same problem will be solved for a Reynolds Numbers ranged from *five* until the limit of the steady state (i.e. until a converged solution exists). The purpose of this stage is to know the limit of the Reynolds number that gives steady state solution. Figure 6-4 shows the velocity vectors for Reynolds number until 40, which is the highest number could be reached.

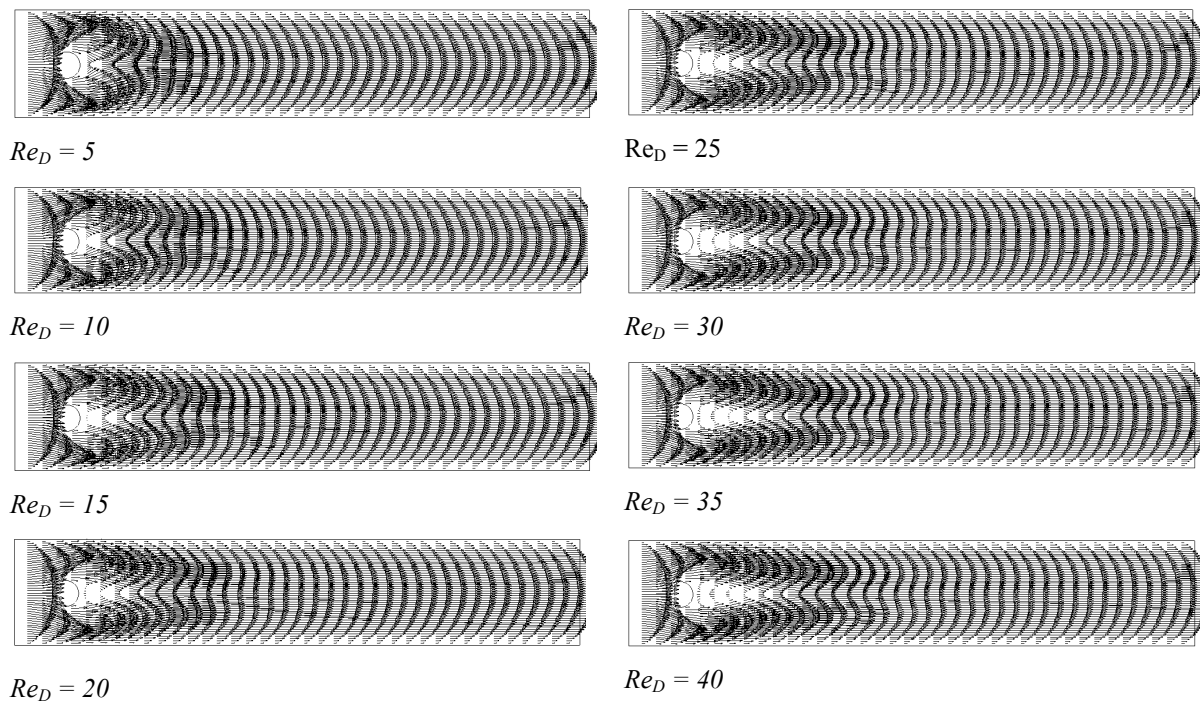


Figure 6-4 The development of the wake behind the cylinder with the increase of Re number for the benchmark problem.

As can be seen, with the increase in Reynolds number the length of circulation L_a also increases. More than $Re = 40$, fluctuations begin to appear and the wake behind the cylinder loses its symmetry and the problem tends to be transient. No solution could be obtained after this value using the steady state techniques and therefore would not be given.

Figures 6-5 and 6-6 show the variation of drag and lift coefficient with Reynolds number for the benchmark problem. The effect of cylinder asymmetry about the centerline of the channel vanishes with the increase in Re . After $Re = 30$ the C_L is almost 0.0. This is because the asymmetry force is very small compared to the term $\rho \bar{U}^2 d / 2$.

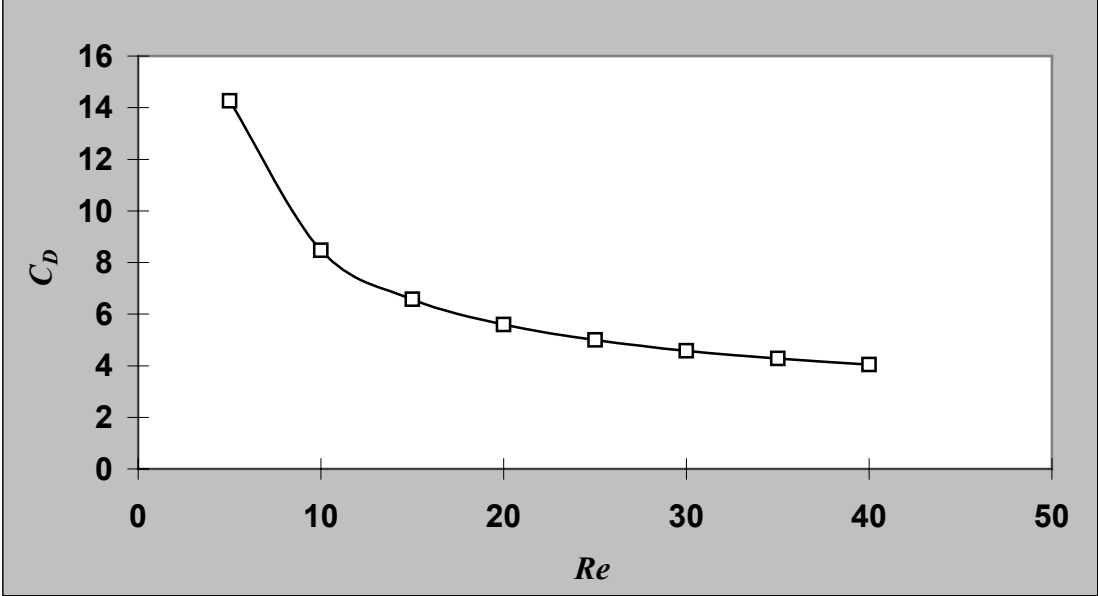


Figure 6-5 C_D Versus Re for the benchmark problem.

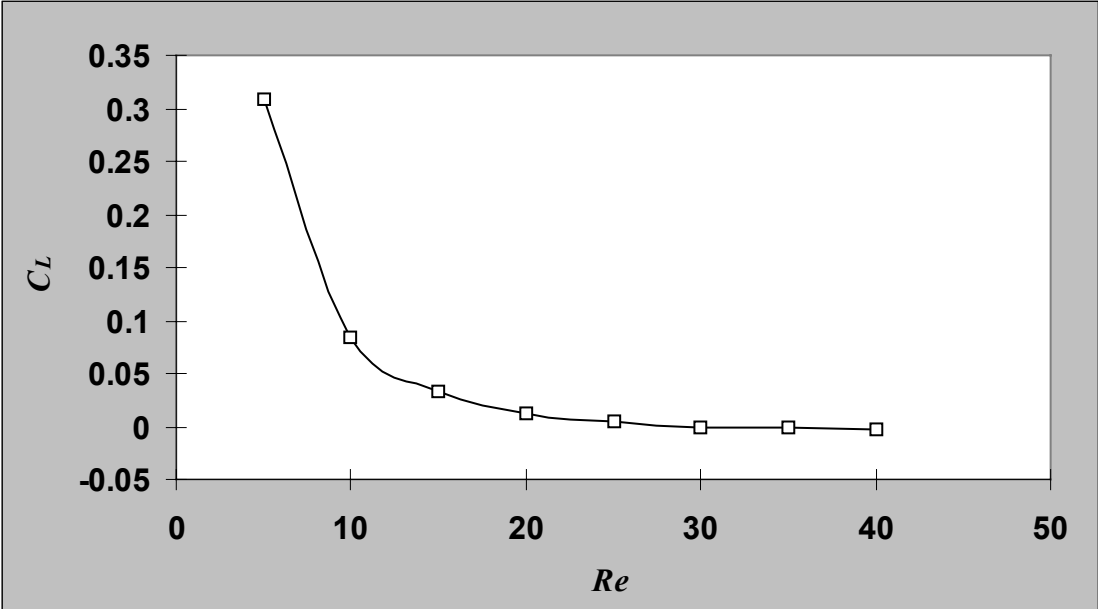


Figure 6-6 C_L Versus Re for the benchmark problem.

6.4.1.4 The ability to simulate the free flow condition

One of the most interesting problems is the steady, free, two-dimensional incompressible and viscous flow past one circular cylinder. It would be very useful to test the programs ability to solve such a problem. As a reference work the paper of F. Nieustadt and H. B. Keller [81] has been selected which used the semi-analytical method of series truncation to solve this problem. The main problem for any FV program is that the domain of solution must be bounded. As the problem here concerning an infinite domain, the boundary condition should be chosen carefully to simulate the free stream conditions. J. Li et al. [65] solved the unsteady case of this problem ($100 \leq Re \leq 500$) and used the following geometrical and boundary conditions to simulate the problem as given in Figure 6-7:

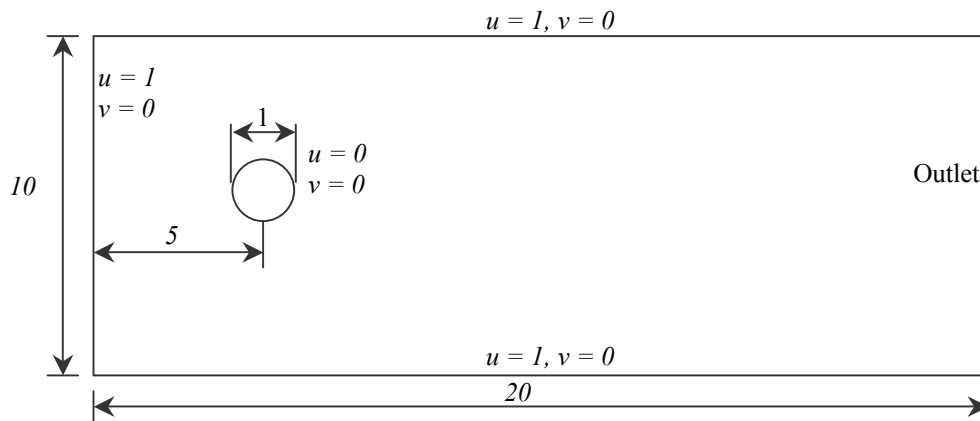


Figure 6-7 Computational domain and boundary conditions used to simulate free flow condition.

The same domain and boundary conditions were used to solve the steady case ($Re=20$). Figure 6-8 shows the velocity distribution on the flow axis behind the cylinder. Here an unstructured mesh like the one used in the benchmark problem has been used but very much finer (47,000 elements instead of 27,000). The Figure shows a good agreement between current results and that of [81].

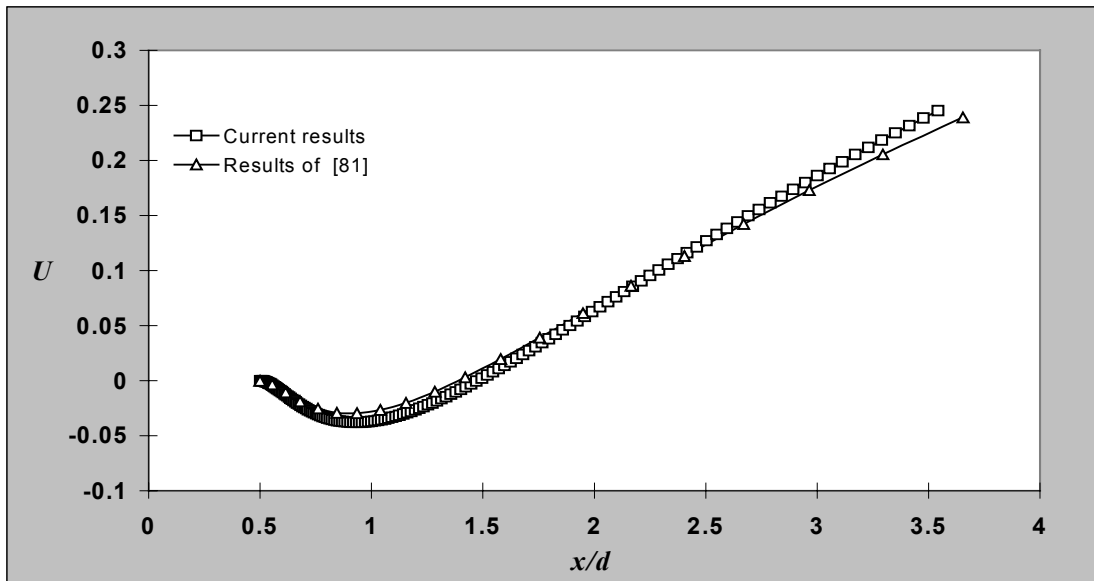


Figure 6-8 Comparison between the current result and that of F. Nieuwstadt [81].

6.4.2 Case b) Unsteady Flow

6.4.2.1 The numerical results

When the Reynolds number is increased beyond a critical value (which for a cylinder in infinite stream is about 40), the flow becomes unsteady and vortices are shed from the cylinder. The same grid from the steady solution was used to solve the problem in the unsteady case. Table 6-2 shows a comparison between the current results and that of the benchmark test.

	$C_{D\ max}$	$C_{L\ max}$	ΔP
Lower bound [78]	3.2200	0.9900	2.4600
Upper bound [78]	3.2400	1.0100	2.5000
Current Results	3.2340	0.9950	2.4930

Table 6-2 Results for unsteady test case compared with the benchmark results.

The same problem was investigated by Muzaferija et al. [82]. They used a second-order three time-level implicit scheme for time integration. Starting impulsively from rest, the flow goes through a development stage and eventually becomes finally periodic. Due to vortex

shedding, both the drag and lift forces oscillate. Figures 6-9 and 6-10 show the oscillation of both the drag and lift coefficient of Muzaferija et al. [82] for the finest grid used (80,000 CVs), compared with our results.

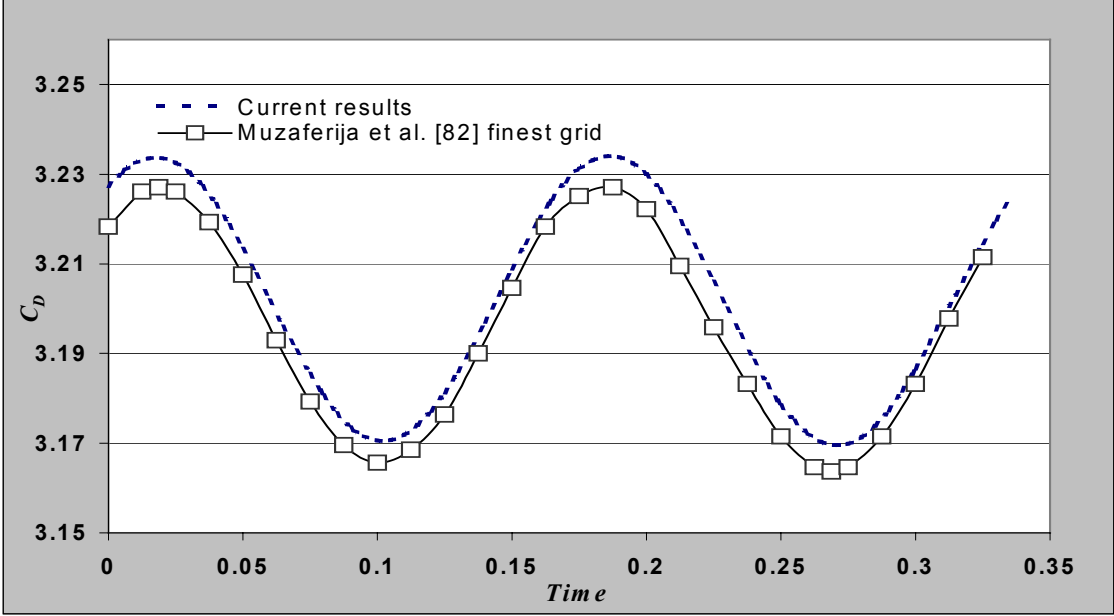


Figure 6-9 Variation of the Drag Coefficient as a function of time.

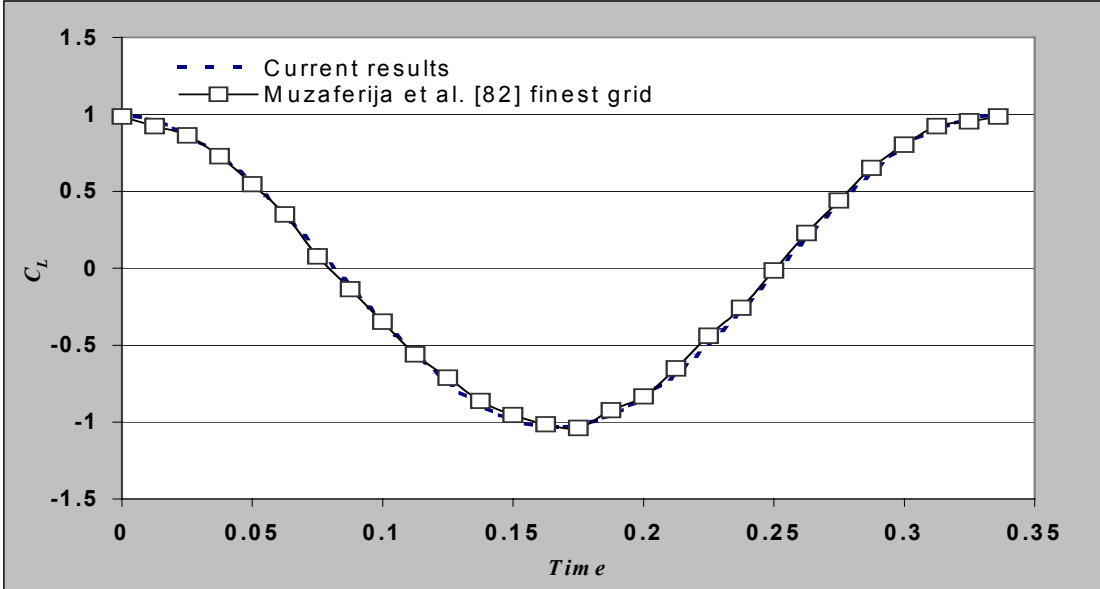


Figure 6-10 Variation of the Lift Coefficient as a function of time.

The drag and lift forces oscillate at different frequencies. The drag has twice the frequency as the lift. The reason is that the drag force has one maximum and one minimum during the growth and shedding of each vortex, while the sign of the lift force depends on the location of

the vortex i.e. whether it is above or below the cylinder. In case of a symmetric configuration, the lift coefficient would oscillate around zero; in this case it oscillates between $C_{L, min} = -1.0325$ and $C_{L, max} = 0.9950$ (Muzaferija et al. [82]. $C_{L, min} = -1.0210$ and $C_{L, max} = 0.9870$). The drag coefficient oscillates between $C_{D, min} = 3.1705$ and $C_{D, max} = 3.2340$ (Muzaferija et al. [82]. $C_{D, min} = 3.1650$ and $C_{D, max} = 3.2280$).

Figure 6-11 shows instantaneous isobars and velocity vectors. The closed pressure contours indicate the location of vortex centers, where the pressure has a local minimum. This figure is nearly the same as in [82]

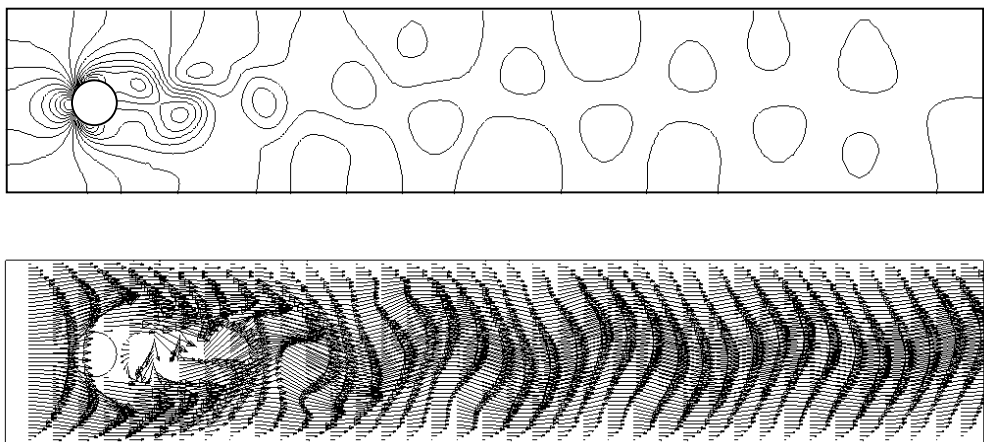


Figure 6-11 Instantaneous isobars (above) and velocity vectors (below) in the laminar 2D flow around a circular cylinder in a channel at $Re = 100$.

6.4.2.2 The gained experience during test phase

6.4.2.2.1 Time step

When choosing the time step, one should consider the Courant number Co as a dimensionless quantity given by:

$$Co = \frac{|\bar{v}| \Delta t}{l} \tag{6.7}$$

where $|\bar{v}|$ and l are characteristic velocity and length, respectively. For optimum results, the user should calculate the Courant number in two ways:

1. **Cell-wise**, by setting $|\bar{v}|$ to an estimated local velocity and l to the corresponding local mesh dimension (e.g. cell diagonal). The time step should be chosen such that the maximum Courant number does not exceed 100 .
2. **Globally**, by setting $|\bar{v}|$ to the estimated average velocity in the flow field and l to a characteristic overall dimension of the model (e.g. channel length in this case here). The time step should be chosen so that it is commensurate with the time scale of the physical process being modeled. In this case, the time step should be chosen such that the maximum Courant number derived from this criterion is typically in the range 100 to 500 . Both Courant numbers (Cell-wise and Globally) are calculated every time step and the maximum Cell-wise Courant number is reported so the user has always the complete information about the time step used.

It was found that the first Courant number (Cell-wise) plays the main role in choosing the time step. One should not expect an accurate solution if the local value of Courant number exceeds 100 . For all calculations done in this work, the used time step produced a maximum cell-wise Courant number much less than 50 .

6.4.2.2.2 Temporal discretization

Only the Crank-Nicholson scheme succeeded to give an accurate solution. The full implicit scheme failed to provide a solution that could compete with the solution of Crank-Nicholson scheme. It might be that is due to the complexity of the problem that requires a great level of accuracy.

6.4.2.3 Benchmark test extension

Like in the laminar case, an extension for the benchmark problem is intended to test the ability of STAR-CD to solve such a problem with higher Reynolds numbers. The main objective of this stage is to know the ability of STAR-CD to solve this problem for higher Reynolds numbers larger than the benchmark. Figure 6-12 shows the velocity vectors and pressure field for Reynolds number = 400 . It is shown that the strength of the pressure change behind the cylinder is now stronger. One realizes that more isobars are now located near the cylinder. This is due to the increase in velocity resulted from the growth of Reynolds number. A solution until $Re_D = 500$ could be achieved with a reasonable CPU time.

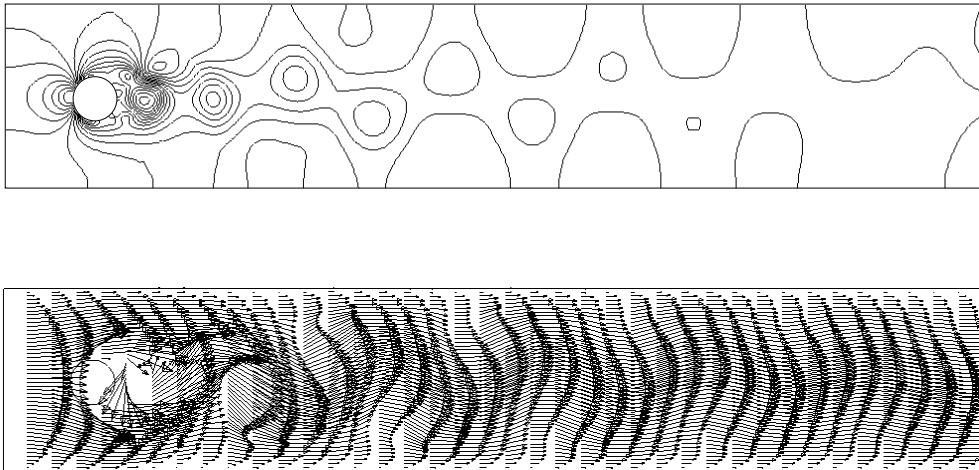


Figure 6-12 Instantaneous isobars (above) and velocity vectors (below) in the laminar 2D flow around a circular cylinder in a channel at $Re = 400$.

Trial runs until $Re_D = 1000$ are also done. But the CPU time is dramatically increased because a minor step (0.0001 sec) is used to achieve an adequate Courant number [80]. That means, 10 real time seconds (the time used to simulate the problem) needs 100000 steps that means weeks of calculations on the available computer.

From the entire above one can conclude that the described code has the ability to solve problems, which are similar to this benchmark with an acceptable accuracy.

In the next chapter, the collected experience gained until now will be implemented to solve the main problem of this work.

Chapter 7

Two Cylinders in a Uniform Stream.

7.1 Introduction

In this section, the flow field between the two cylinders in a parallel fluid stream and the effect of changing s/d in the flow characteristics will be studied. The pitch to diameter ratio s/d will be changed from 3.0 to 1.5. Because of the high complexity of the problem, the value of Reynolds number will be fixed in this chapter at 500 and s/d will be the only parameter under consideration. The effect of changing Reynolds number will be discussed in a later chapter. All other parameters will not be changed. The domain of solution (Figure 2-1) will be that of Li et al. [65] (which has been taken for benchmark of the calculations in section 6.4.2.2). The domain length to cylinder diameter ration n/d will be 55, i.e. 35 diameters more than that taken by Li to minimize the effect of the outlet as possible. The ratio of the height to cylinder diameter h/d is taken to be 12.0, not 10 because of the presence of the second cylinder. However, Li studied the effect of lateral boundary limits on the vortex shedding. It was found that, if the ratio of the lateral boundary width to the cylinder diameter is greater than *five*, the lateral effect could be neglected. The ratio b/d will get the same value of 5.0.

As mentioned before, the fluid taken here is air. By setting the cylinder diameter to be 1.0 m, the required Reynolds number will be defined by selecting the corresponding value of the entrance velocity u_∞ .

As a last test for the used code, variable combinations of u_∞ and d have been taken to keep Reynolds number constant in each case. There were no changes in the obtained results.

All the gained experience from the benchmark test was applied to the problem including grid structure, the discretization scheme, time step and temporal discretization scheme. Figure 7-1 shows a mesh sample used to discretize the solution domain. A magnified part of the mesh is also illustrated and it shows how dense the mesh is near the walls. The number of cells was

about 46000 cells. The time step chosen was about $1/100$ of the vortex shedding frequency to effectively capture the vortex shedding process keeping in mind the limit of Courant number discussed before. All calculations are performed using the double precision calculations option.

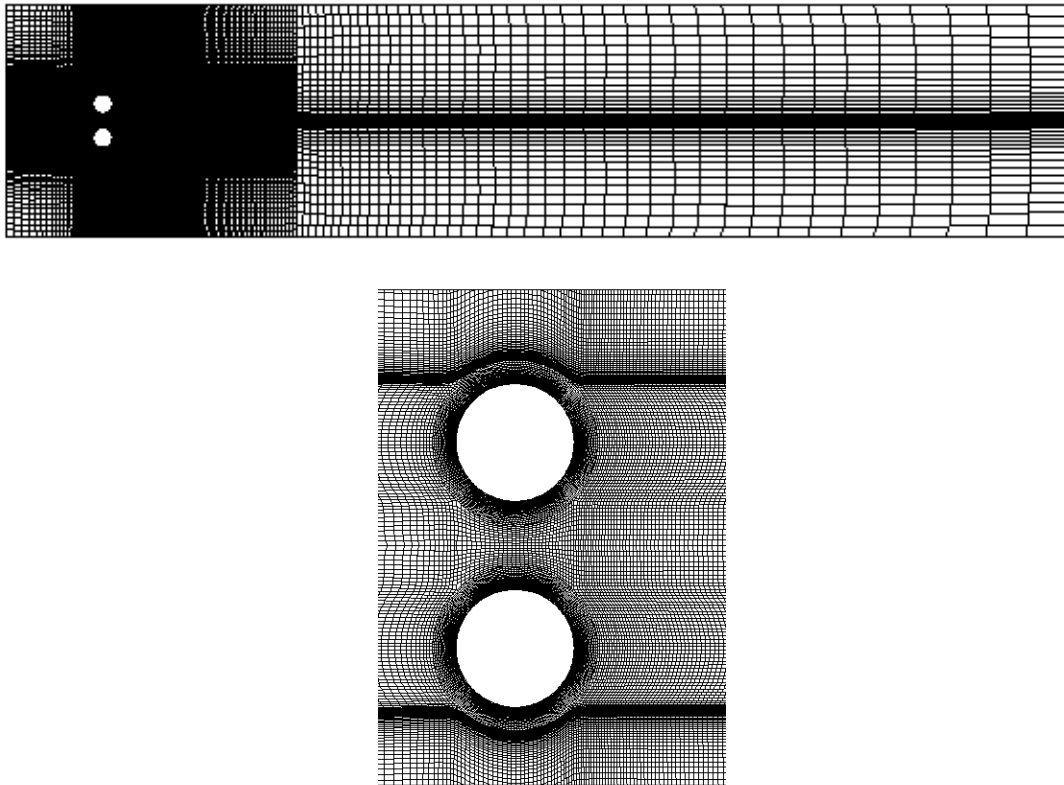


Figure 7-1 A typical mesh used to discretize the solution domain for pitch to diameter ratio $s/d=1.75$.

7.2 Normalizing the Results

During the calculations phase, all the results are given in a dimensional form. This is because the used code (STAR-CD) accepts only dimensional quantities. To generalize the solution, one must represent the results in a non-dimensional form. Therefore, some dimensionless quantities should be defined, and all the results will be expressed in terms of it. Let us define:

$X = \frac{x}{d}$ as a normalized x distance,

$Y = \frac{y}{d}$ as a normalized y distance,

$U = \frac{u}{u_\infty}$ as a normalized velocity in x direction,

$V = \frac{v}{u_\infty}$ as a normalized velocity in y direction,

$T = \frac{t}{f}$ as a normalized time, where f is the vortex shedding frequency,

$P = \frac{p}{\frac{1}{2} \rho_\infty U_\infty^2}$ as a normalized pressure,

$\Theta = \frac{\vartheta - \vartheta_\infty}{\vartheta_o - \vartheta_\infty}$ as a normalized temperature in case of constant wall temperature,

and $\Theta = \frac{\vartheta - \vartheta_\infty}{\frac{q_o d}{k}}$ moreover, as a normalized temperature in case of constant wall heat flux.

All the results will be expressed in terms of these quantities.

The fluid flow results include: 1.) flow fields represented by velocity vectors; 2.) normalized pressure distribution P on cylinders' surface; 3.) lift and drag coefficients and 4.) Strouhal number. These results are discussed first, followed by a discussion of heat transfer results.

7.3 Fluid Flow Results

7.3.1 The Vortex Shedding and Flow Pattern behind the Cylinders

At the beginning, it is important to understand the flow pattern of the problem by observing the changes occurred in the velocity field behind the cylinders with respect to time. To clearly represent the interference between two cylinders, three case studies were chosen:

1. the case of $Re_D = 500$ and $s/d = 3.0$,
2. the case of $Re_D = 500$ and $s/d = 2.0$,
3. the case of $Re_D = 500$ and $s/d = 1.5$.

This is because the flow behavior changes completely from the first case to the last one.

Bearman et al. [68] have photographed the flow at this Reynolds number in a smoke channel. The flow behavior of the present problem will be compared with that of Bearman by using the velocity vectors obtained from the numerical solution and one will try to understand the flow pattern and make a comparison between current results and those of Bearman.

Starting with the case of $s/d = 3.0$, Figures 7-2 show the velocity vectors for that case. As a result, for each time step, there is a magnified velocity-vectors diagram of the upper cylinder. It will help to understand the formation and shedding of vortices near the cylinders.

At the beginning of the cycle ($T = 0.0$ Fig. 7-2-2a) there is almost one vortex behind each cylinder. The edge of the jet flow is directed towards the vortex streets. The flow changes its direction to form a second vortex (the blue color represents lower velocity magnitude). It is seen that the vortex street flow impacts with each other at a certain distance leading to a local increase in the velocity magnitude (the red color represents higher velocity magnitude).

By increasing the time ($T = 1/8$ in Figure 7-2-2b), the vortex behind each cylinder is moved away from the jet flow (vertically) and advances horizontally. In addition, the whole velocity pattern advances to the right and the movement of the wake behind each cylinder seems to resist the separated flow from the separation point away from the jet flow.

At $T = 2/8$, it is seen that a new vortex is formed near the separation point away from the jet flow. The old vortex is now in its way to vanish. It is also seen that all the vortices are advancing in the downstream direction.

By further increase in time ($T = 3/8, 4/8$ and $5/8$), the newly formed vortex is moving in the opposite direction of the old vortex (to and not away from the jet flow). This is the supposed “phase change” of the vortex formation process.

In the last two time steps, it is seen that a new vortex is formed near the separation point at the jet flow. This is the so-called old vortex found at time step $T = 0.0$.

The vortex formation and shedding is markedly symmetric about the axis of the gap for both half cycles. One can realize the clear couple of the vortex shedding at each cylinder. The jet formed in the gap between cylinders gives flow to both streets, which decrease its velocity locally (the blue color represents lower velocity magnitude). This behavior is totally reversed when the shedding process changes its phase (i.e. when the lift coefficient reaches its minimum and starts to increase). That means, instead of giving flow to the streets, it receives flow from them.

Proceeding to $s/d = 2.0$, a magnified velocity-vectors diagram is not necessary because the two cylinders are now closer and the available space is sufficient to represent the velocity diagrams behind the cylinders. Figures 7-3 show the vortex shedding at this value of s/d . As can be seen, the vortex formation and shedding process is still similar to the previous case. The vortices in both streets are still coupled, but there is a slight asymmetry about the gap axis.

Now the results of the case $s/d = 1.5$ will be represented. Figures 7-4 show the velocity vectors behind the two cylinders. As seen in the figures, everything has been changed. The flow in the gap between the cylinders is seen to be biased towards one of the cylinder. As seen in the figures, the flow would remain biased in this direction for some time before swapping to the other side. This is the so-called *bistable nature* of the biased flow.

As mentioned before, the same Reynolds number was used for the photos of Bearman et al. [68]. There is a very good agreement between our results and those of Bearman. The same flow behavior was reported in [68] although the ratio s/d taken was 1.85. The *bistable nature* of the flow was found to take place even when $s/d = 1.5$. This agrees with the results of Bearman who found that the *bistable nature* of the flow takes place even at $s/d = 1.85$ but not

agree with the results of Ishigai, et al. [61], who said that the *bistable nature* of the flow is found to take place only when $s/d = 1.25$. This could be due to the different Reynolds numbers considered.

There is a great degree of irregularity in the vortex street behind the cylinders. The flow is confused with no apparent dominant vortex structure. In addition, the swapping of the jet flow from one cylinder to the other is found to be irregular with the time. More details about this point will be given when discussing the Strouhal number.

In addition, the ratios $s/d = 1.25, 1.75, 2.25,$ and 2.5 have been studied. When $s/d \geq 2.0$ the flow acts in a way similar to that described by Figures. 7-2 and 7-3, i.e. coupled vortices in both streets with symmetry about the gap axes. When s/d is less than 2.0 , the *bistable nature* of the flow is found to take place and the irregularity of the flow behind the cylinders increases with the decrease of s/d .

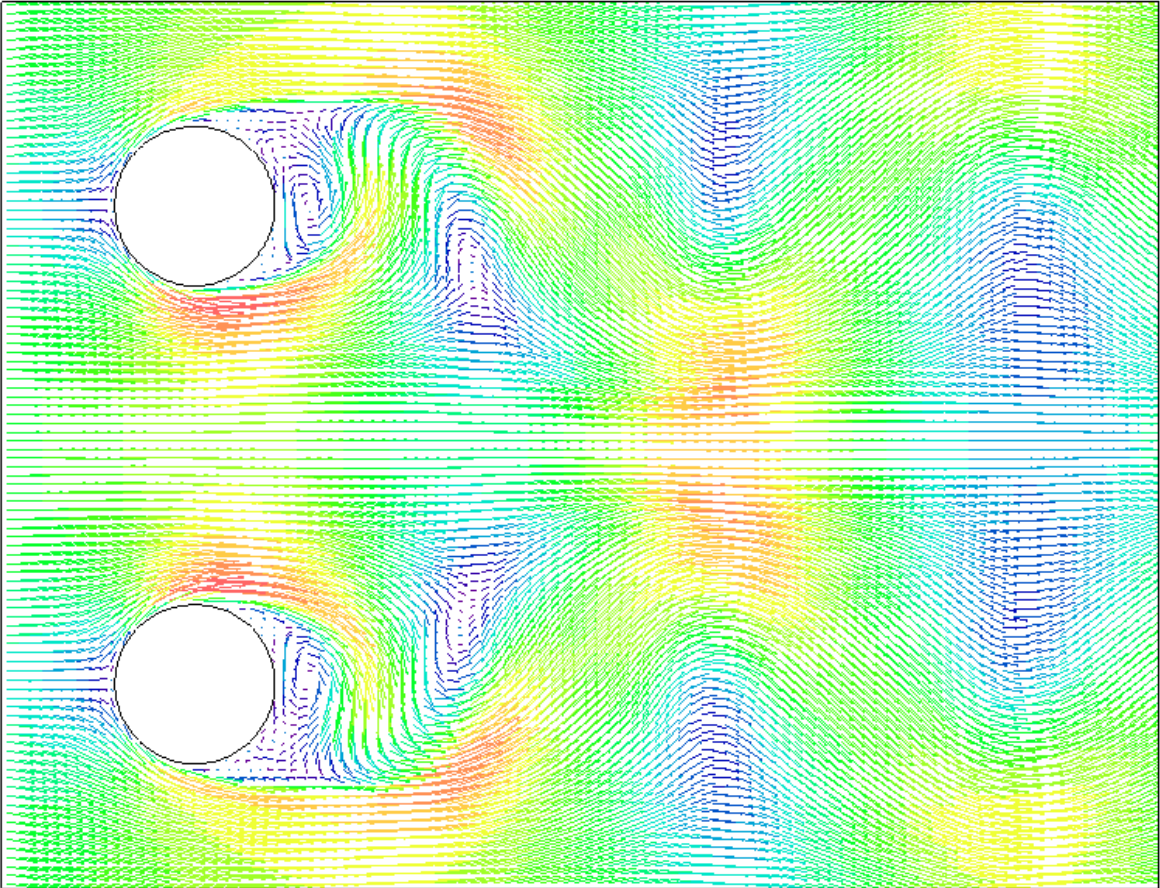


Figure 7-2-1 The vortex formation and shedding process for the case $Re = 500$ and $s/d = 3.0$ ($T = 0.0$ Magnified).

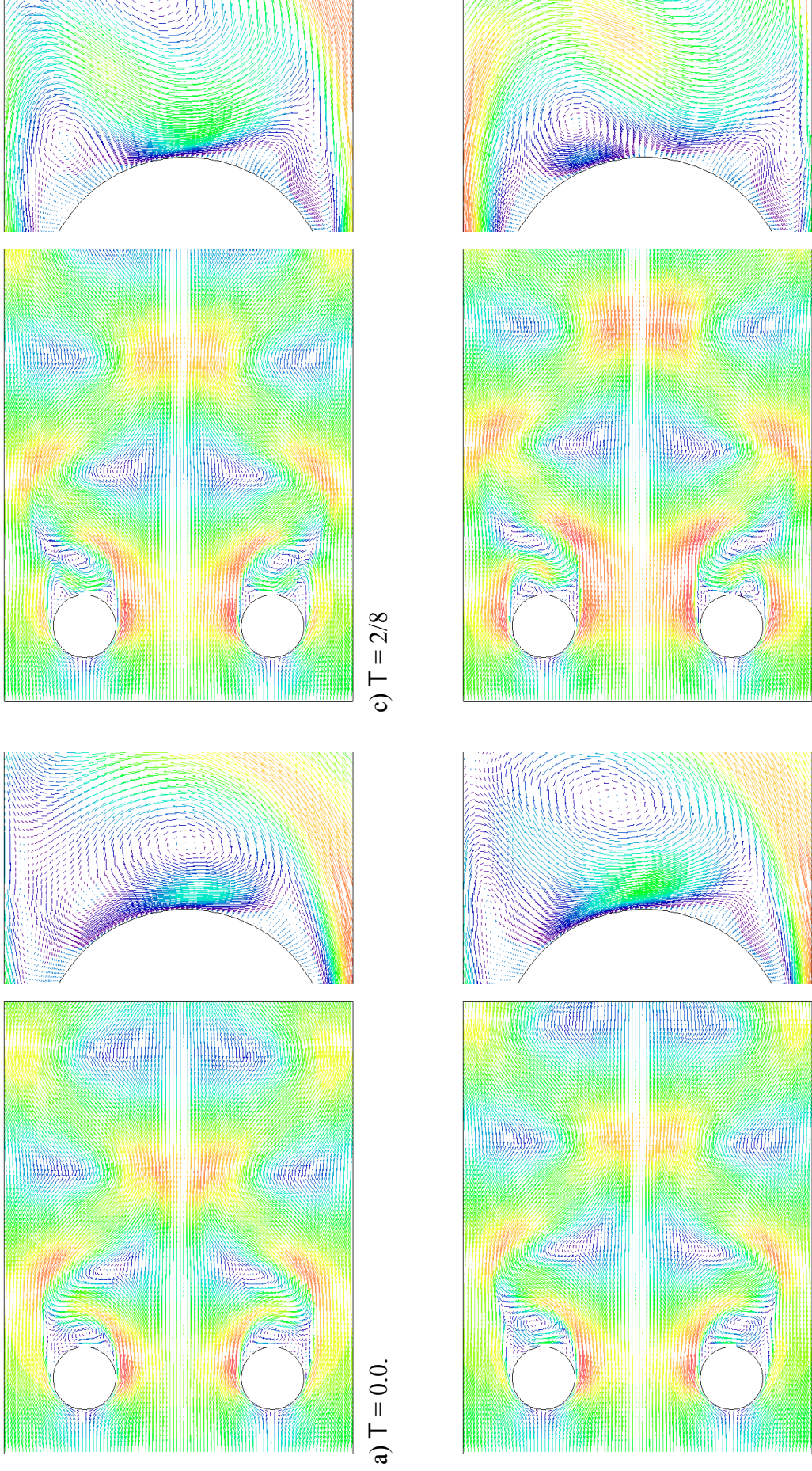


Figure 7-2-2 The vortex formation and shedding process for the case $Re = 500$ and $s/d = 3.0$ (the first half cycle).

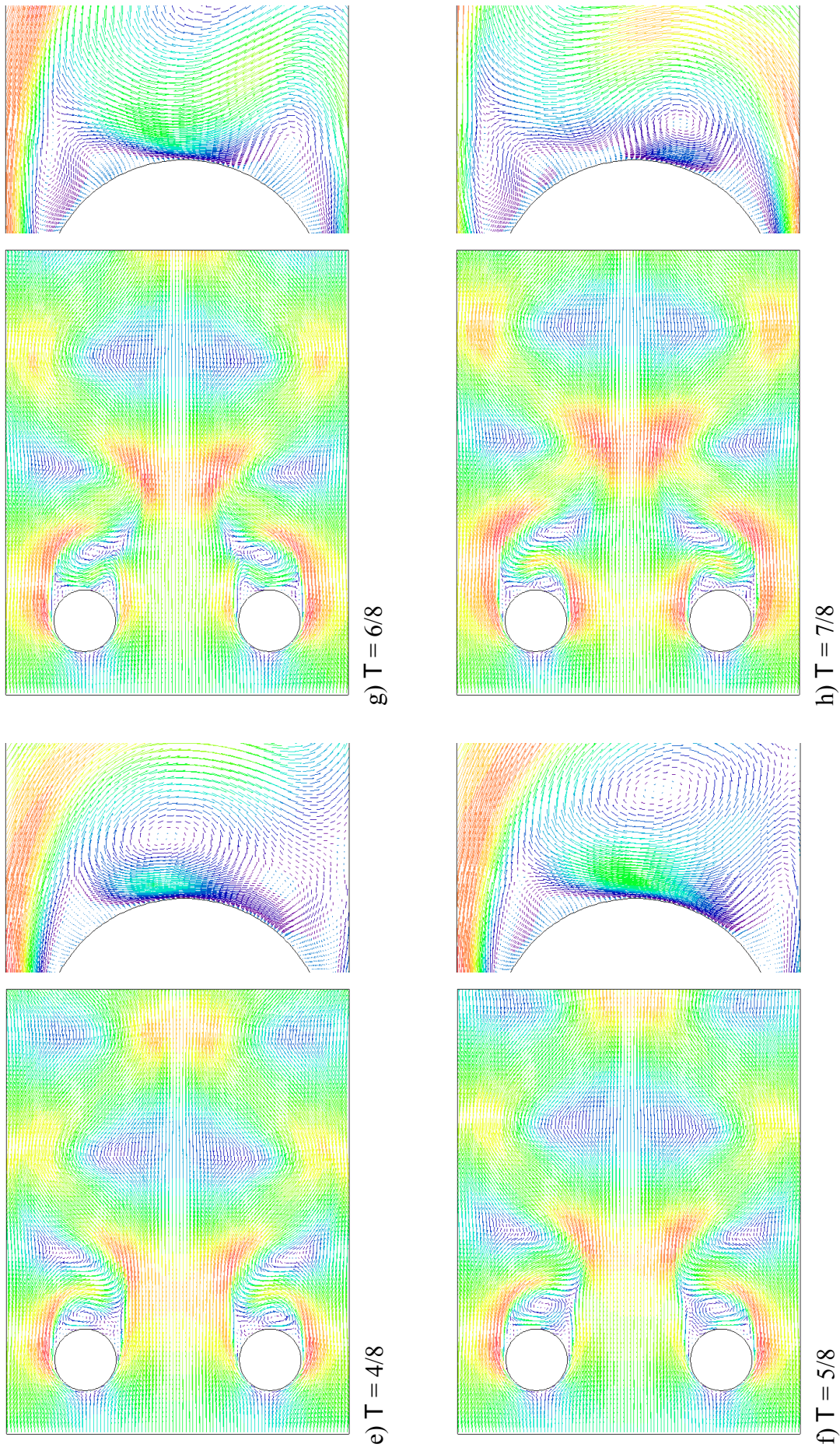
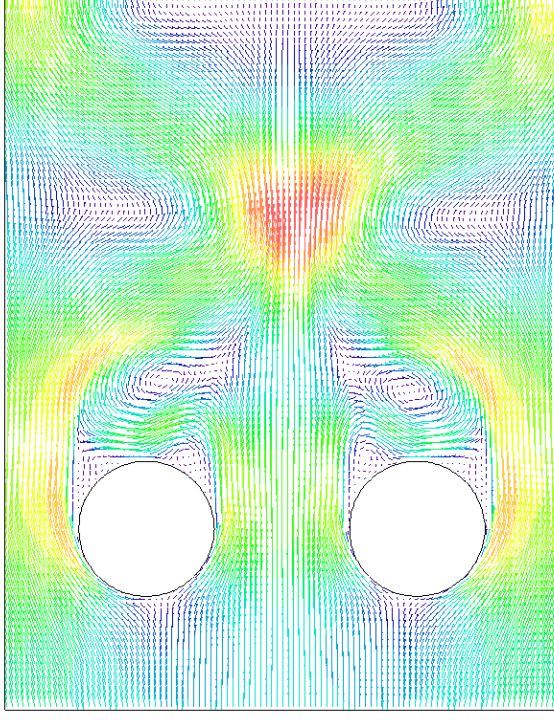
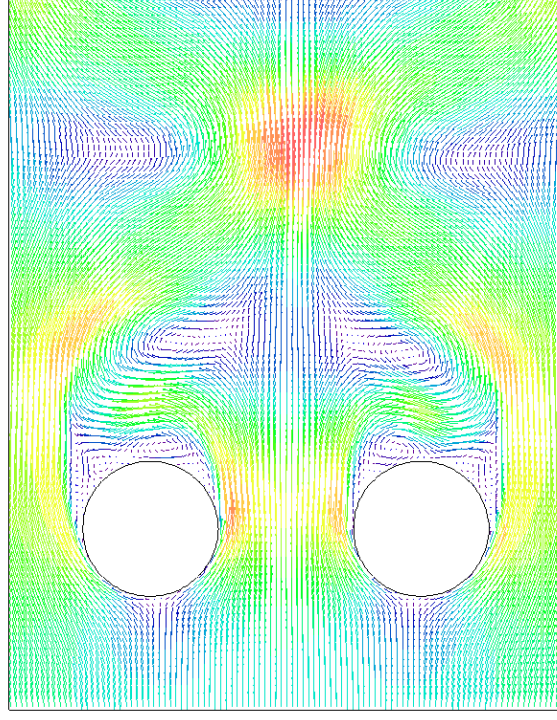


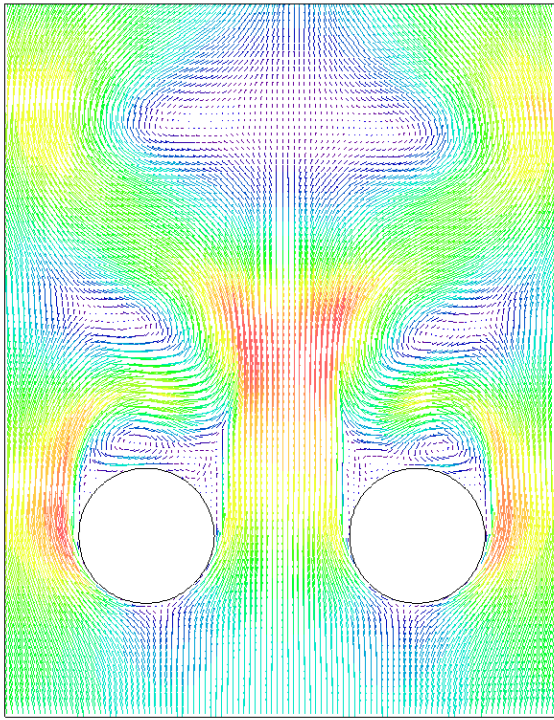
Figure 7-2-3 The vortex formation and shedding process for the case $Re = 500$ and $s/d = 3.0$ (the second half cycle)



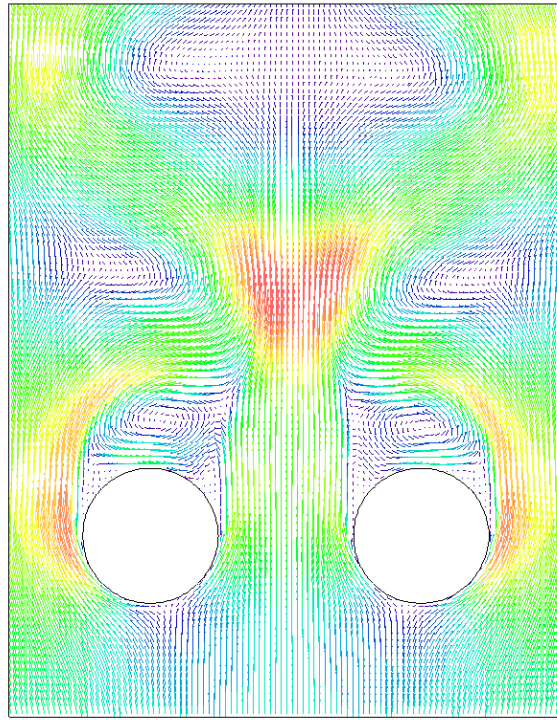
c) $T = 2/8$



d) $T = 3/8$

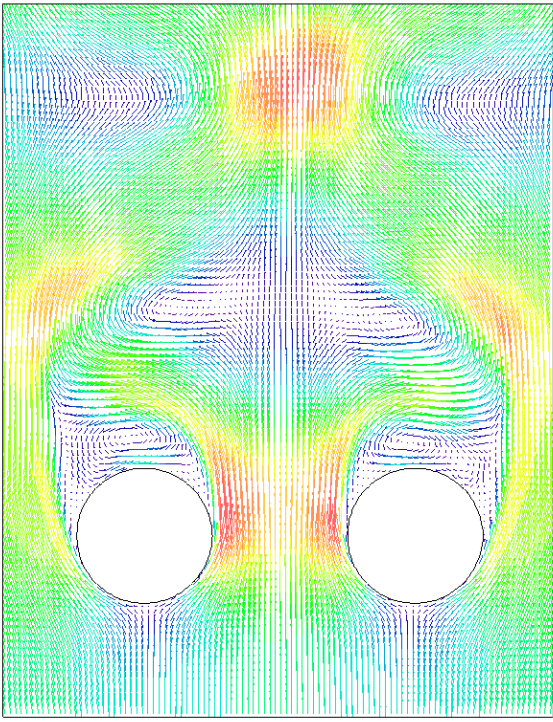


a) $T = 0.0$.

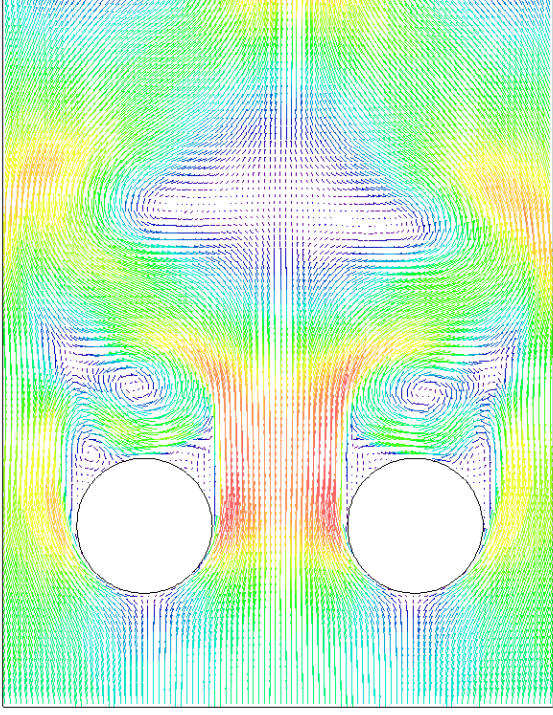


b) $T = 1/8$

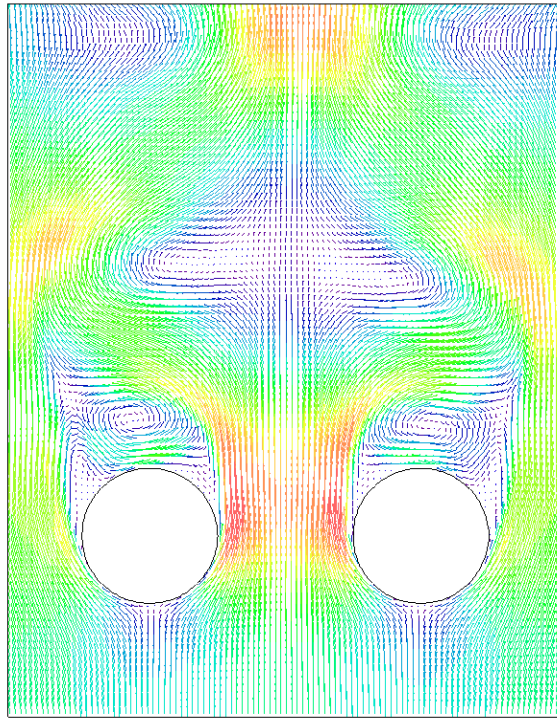
Figure 7-3-1 The vortex formation and shedding process for the case $Re = 500$ and $s/d = 2.0$ (the first half cycle).



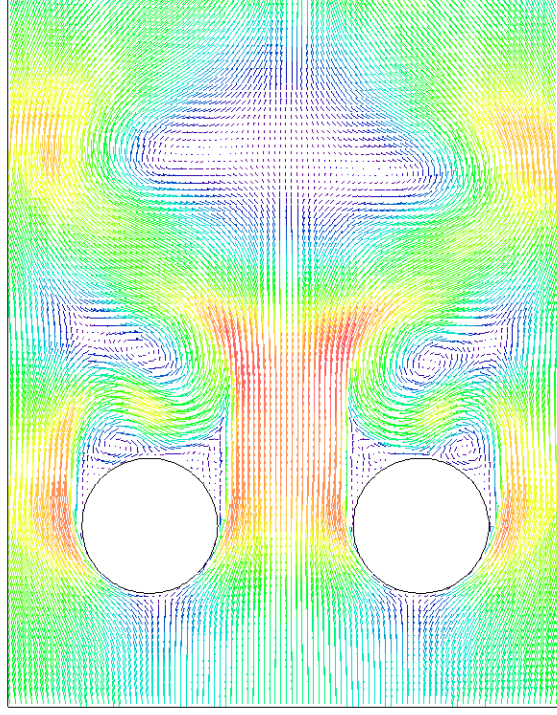
e) $T = 4/8$



g) $T = 6/8$



f) $T = 5/8$

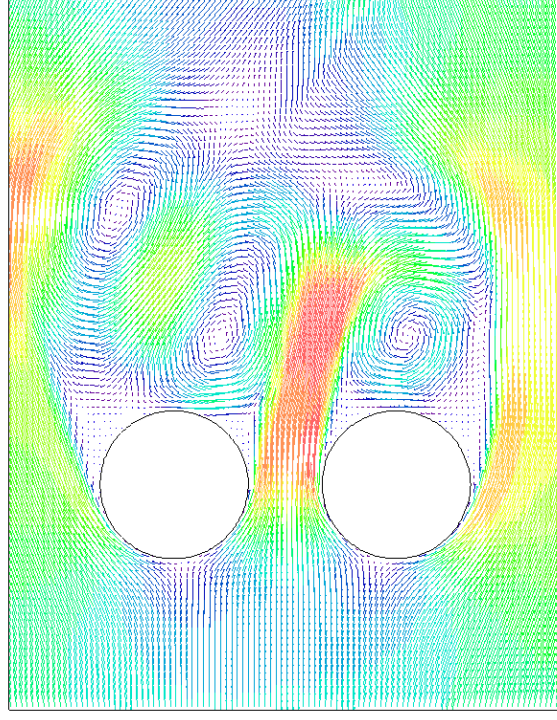


h) $T = 7/8$

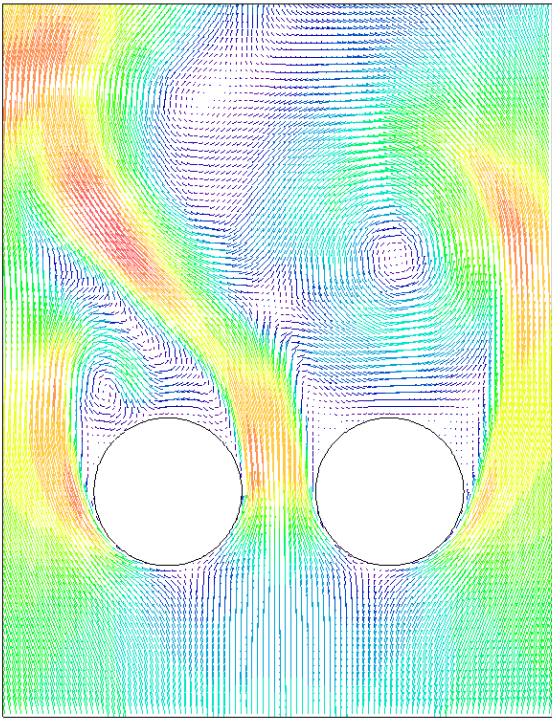
Figure 7-3-2 The vortex formation and shedding process for the case $Re = 500$ and $s/d = 2.0$ (the second half cycle).



c) $T = 2/8$



d) $T = 9/8$



a) $T = 0.0$.

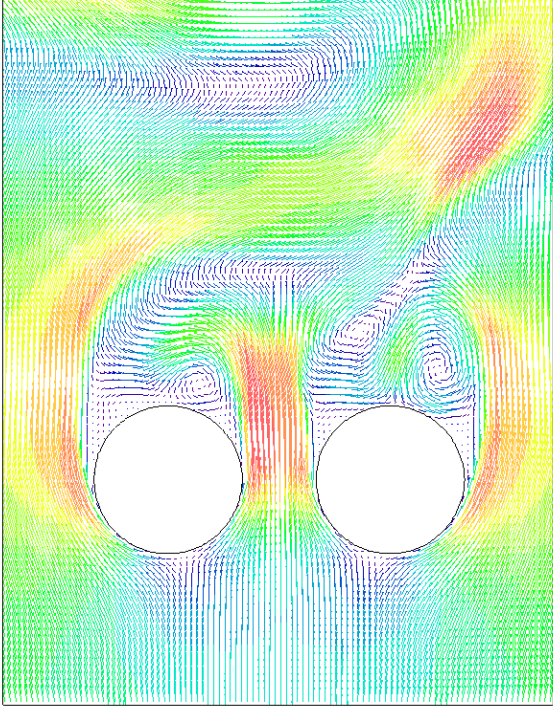


b) $T = 1/8$

Figure 7-4-1 The vortex formation and shedding process for the case $Re = 500$ and $s/d = 1.5$.



e) $T = 12/8$



g) $T = 18/8$



f) $T = 14/8$



h) $T = 20/8$

Figure 7-4-2 The vortex formation and shedding process for the case $Re = 500$ and $s/d = 1.5$.

7.3.2 Pressure Distribution

7.3.2.1 Pressure field

The pressure field gives a better understanding about the vortex streets behind the cylinders. The closed pressure contours indicate the location of vortices centers, where the pressure has local minimum.

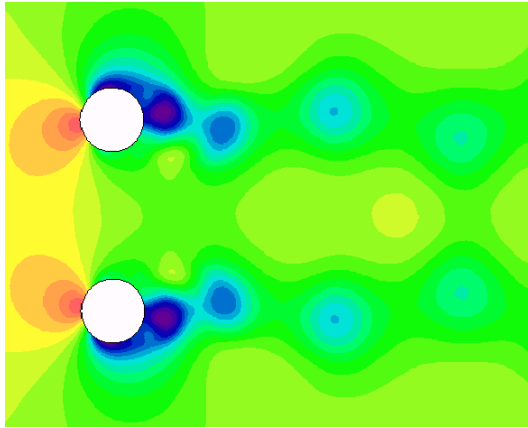
Figure 7-5 shows the instantaneous pressure field around the cylinders for a range of pitch to diameter ratios s/d . The time at which each figure is captured is selected to represent the main characteristics of the pressure field at the value of s/d . The red color represents the highest-pressure value (positive), while the dark lily represents the lowest pressure value (negative). The closed blue pressure contours indicate the locations of vortex centers, where the pressure has a local minimum.

As seen in the figure, for the case $s/d = 3.0$ there are two clearly defined vortex streets. The pressure reaches its maximum at the forward stagnation point. Behind the cylinders, -in the wake- the pressure takes a negative value. In the street, the core of each vortex is represented by a closed contour. There is also a clear symmetry around the gap centerline.

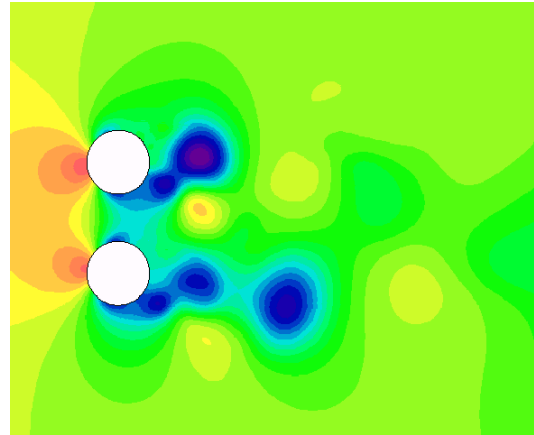
This symmetry takes place until $s/d = 2.25$ (not shown). At a pitch to diameter ratio of 2.0 , it is found that the symmetric situation starts to change specially behind the cylinders. After a certain distance from the cylinders, we can realize that the vortices are symmetric.

Furthermore, by decreasing s/d until 1.75 we see that there is no more symmetry about the gap axes. Although there are two vortices shed from the cylinders, we see that after a certain distance the two streets join each other to form one street of vortices.

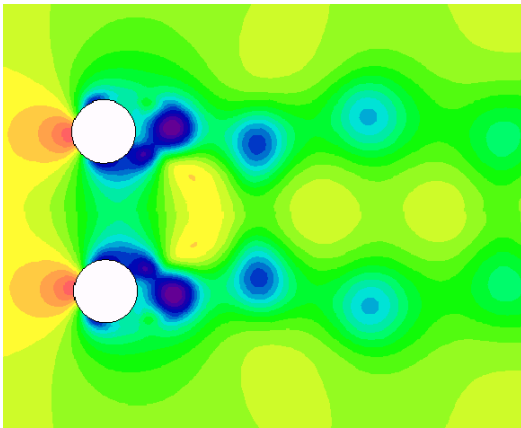
By decreasing s/d more and more, we see that the vortices behind the cylinders join each other earlier than before. There are usually a large wake and small wake formed behind the cylinders. The same trend continues at $s/d = 1.25$. For that extreme case ($s/d = 1.25$), we cannot define any real vortex street at all. There is one big vortex behind one cylinder. This vortex changes its shape and position with the time. It can also seen that the vortex shedding becomes weak for the values of $s/d \leq 1.75$.



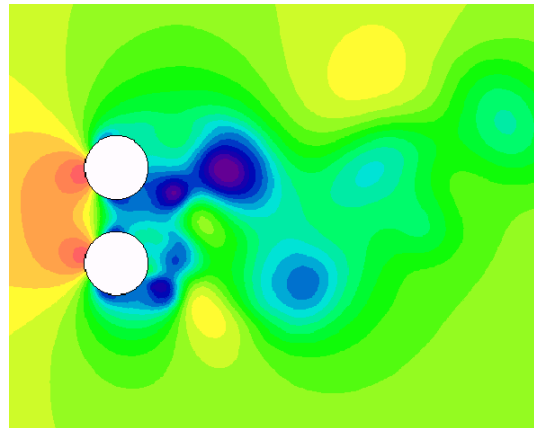
$s/d = 3.0$



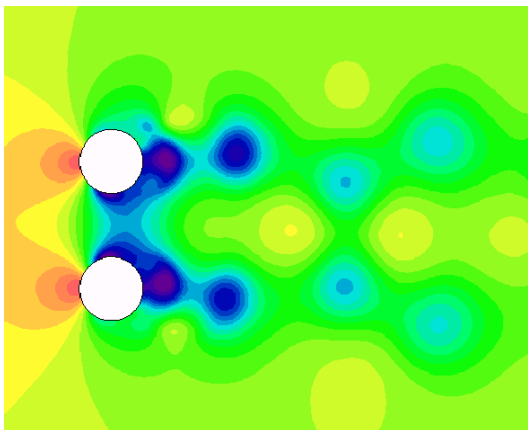
$s/d = 1.75$



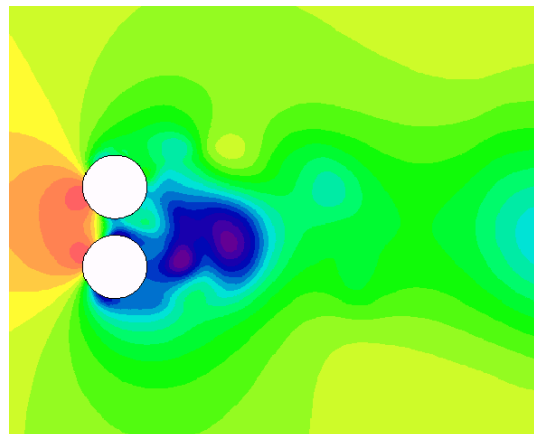
$s/d = 2.5$



$s/d = 1.5$



$s/d = 2.0$



$s/d = 1.25$

Figure 7-5 Instantaneous pressure field variation with the change in s/d .

7.3.2.2 Normalized pressure distribution on the surface of the cylinders

7.3.2.2.1 Instantaneous pressure variation

The pressure distribution on the surface of the cylinders will be now analyzed. To represent the instantaneous pressure variation with time on different surface points, two cases will be studied: the case of $s/d = 2.5$ and $s/d = 1.5$. Nine surface points are considered where θ is the angle measured counter clockwise from the rear (base) point of the cylinder.

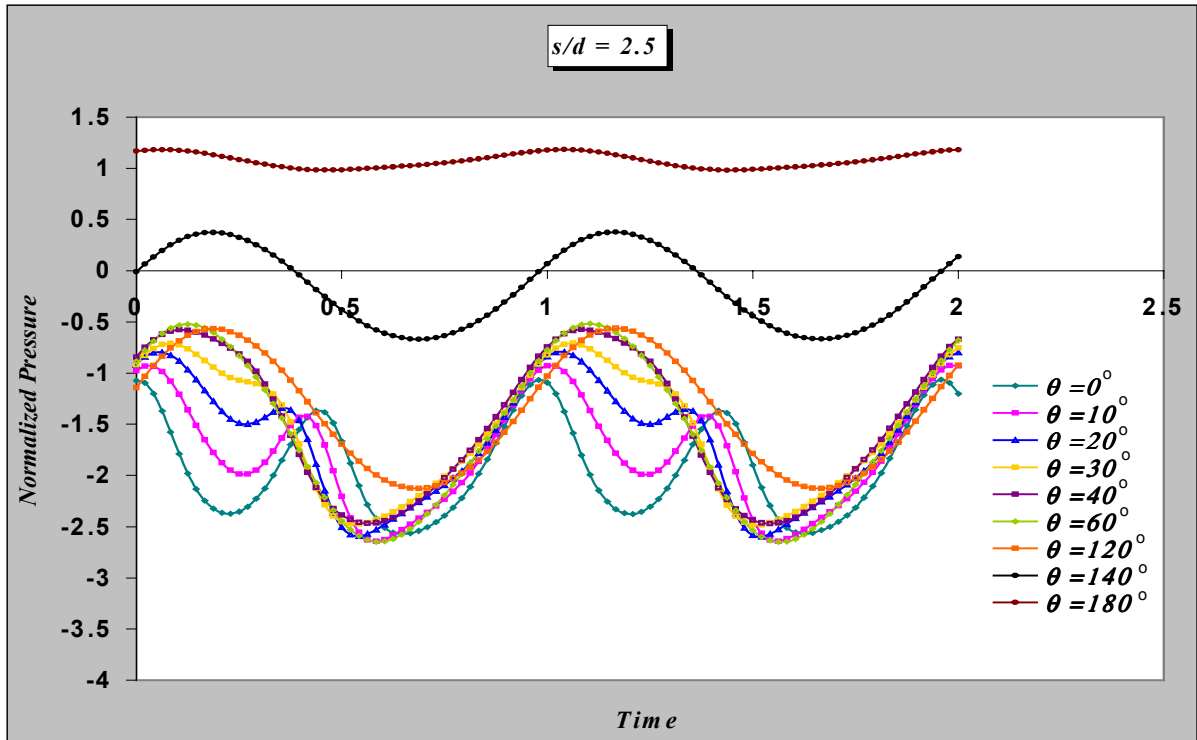
For the first case (Figure 7-6-a), the pressure variation with time takes a sinusoidal form for all the points under consideration. At the base point ($\theta = 0^\circ$), the pressure variation has two maxima and two minima during a one C_L cycle. By increasing θ we see that time variation of the pressure trends to have only one single maximum and one single minimum during one C_L cycle. Furthermore, by increasing θ until reaching the forward base point ($\theta = 180^\circ$) we see that the time variation of the pressure is not so strong and we can consider it almost constant.

For the second case (Figure 7-6-b), there is a difference in the zone between the two separation points. For example, at $\theta = 0^\circ$ one cannot define a repetitive change of pressure. The pressure increases and decreases smoothly but not in a harmonic way. By increasing θ , the pressure variation seems to have a more wavy form and concedes with the trend of the previous case. Far a way from the separation point, the pressure variation starts to have the wavy form with one maximum and one minimum for one cycle.

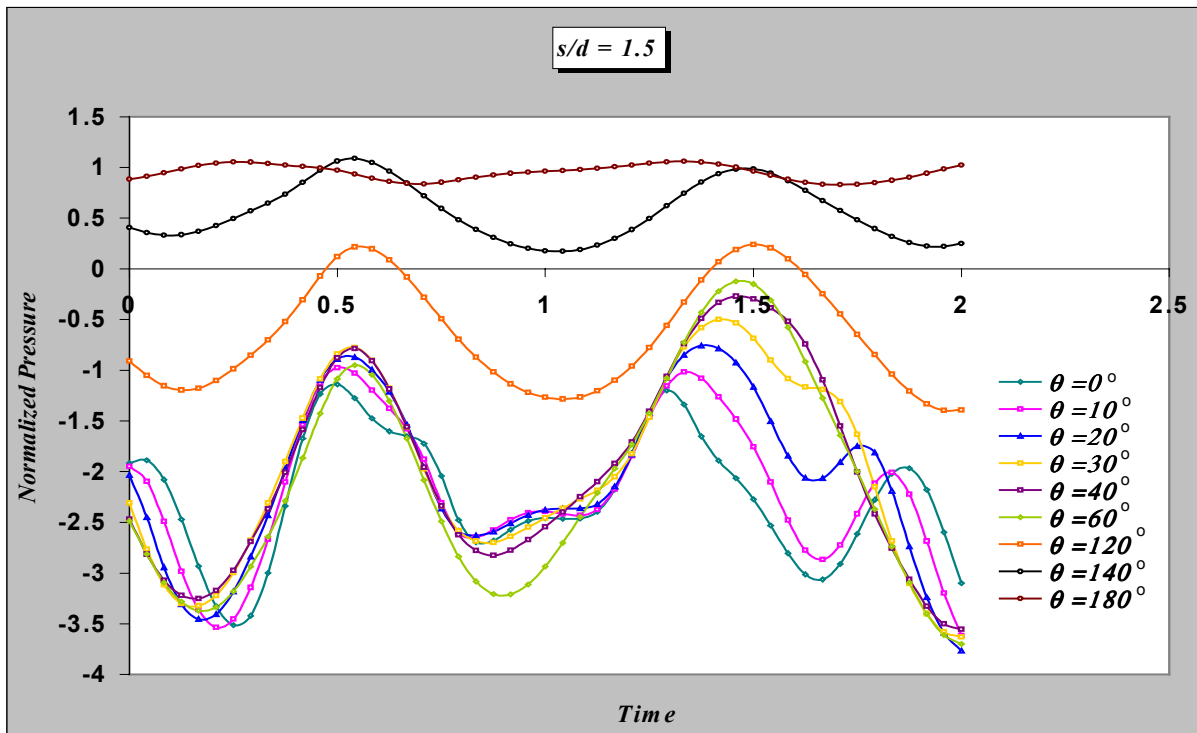
The previous two cases represent the main pressure variation groups, which are found to take place in this work. Until $s/d \geq 2.0$, the time change of pressure is similar to the first case. For $s/d < 2.0$ the change is similar to the second case.

7.3.2.2.2 Mean pressure distribution on the surface of the cylinders

We will now look at the mean pressure distribution on each surface of the cylinders. This view will help us to determine the effect of the presence of the second cylinder in the location of the forward stagnation point of each cylinder where the stagnation point is defined to be the point that has the maximum pressure on the surface. Figure 7-7 shows the normalized pressure distribution on the surface of the upper cylinder for different ratios of s/d .



a)



b)

Figure 7-6 Instantaneous normalized pressure on different surface points of the lower cylinder for the cases $s/d = 2.5$ and $s/d = 1.5$.

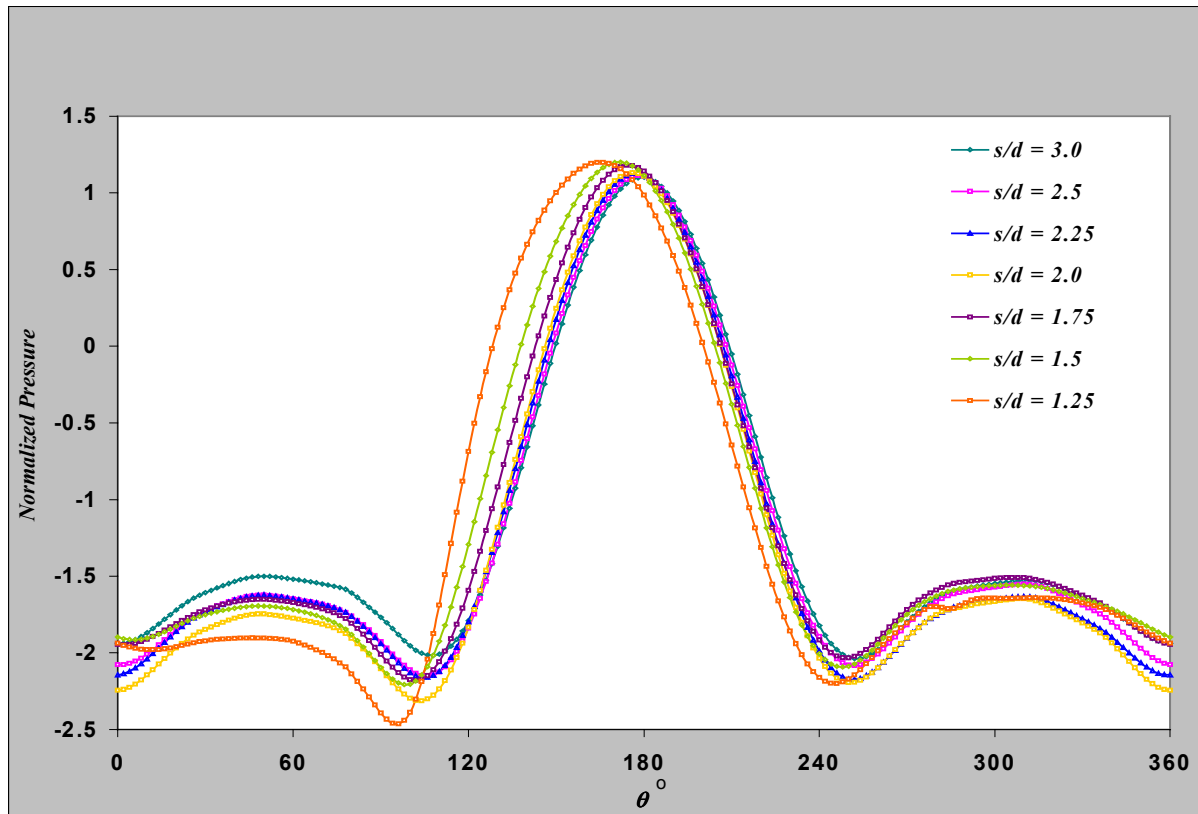


Figure 7-7 Normalized mean pressure distribution on the surface of upper cylinder for a range of s/d .

The angle θ is measured from the rear (base) point of the cylinder in clockwise direction. For all values of s/d , the flow is found to be symmetric about the front stagnation point in the region between the two separation points except for the cases $s/d = 1.5$ and $s/d = 1.25$ where there is a slight variation in the location of each separation point.

The movement of the stagnation point due to the proximity of the other cylinder is represented in Figure 7-8. The angle α represents the location of the front stagnation point measured from the base point in a clockwise direction. The change of the location of the stagnation point due to the change in s/d is more rapid in the range $s/d \leq 2.0$. By increasing s/d , the stagnation point moves toward its normal location (i.e. $\alpha = 180^\circ$). Also decreasing the gap between the cylinders until $s/d = 0.0$ will shift the stagnation point to be at $\alpha = 270^\circ$.

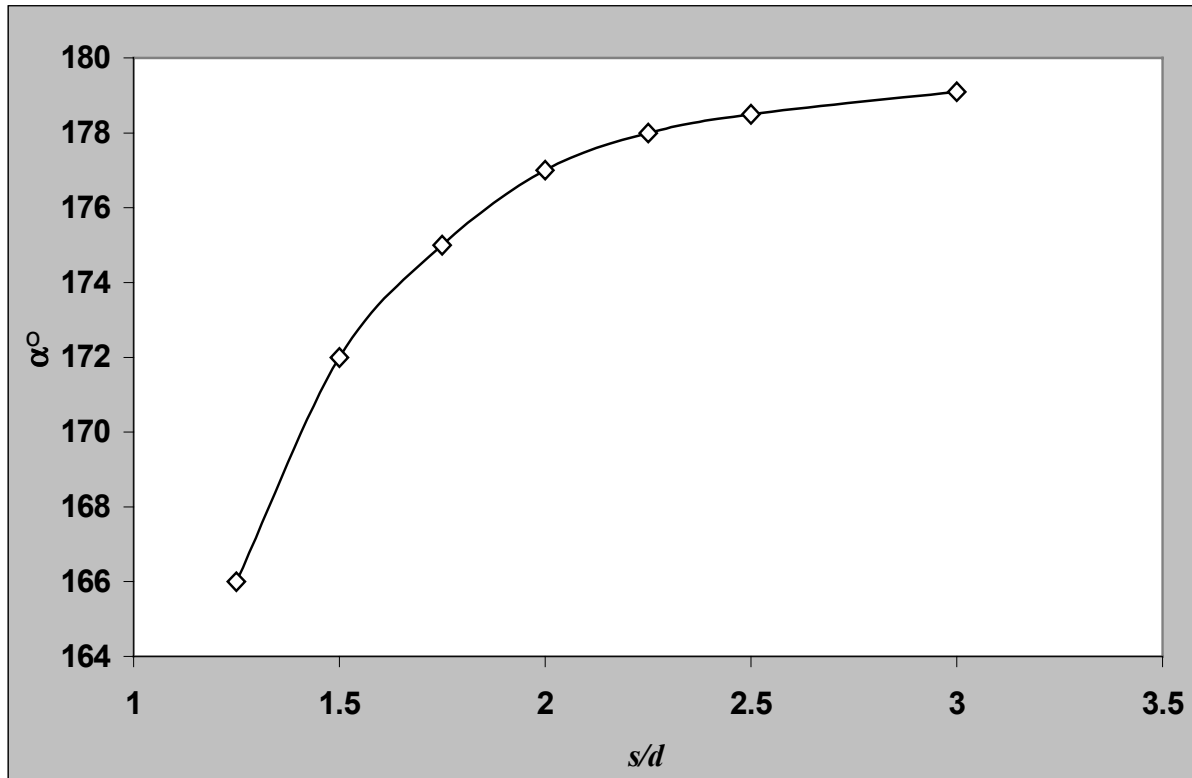


Figure 7-8 The movement of the front stagnation point due to proximity of the other cylinder.

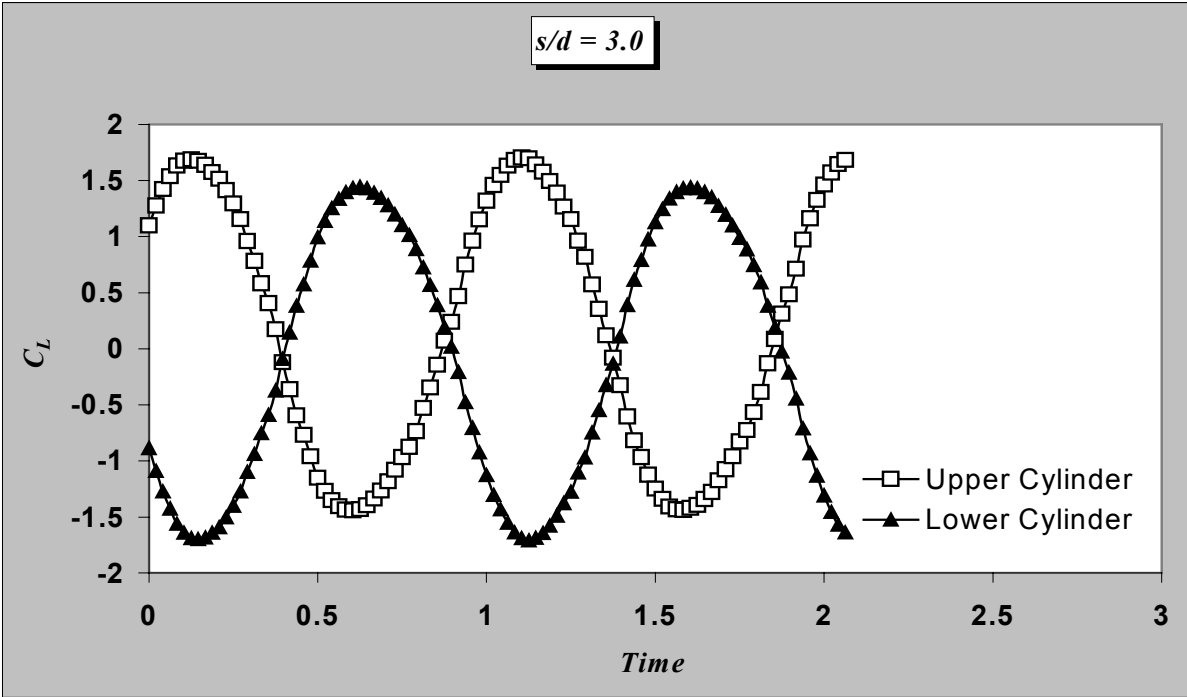
7.3.3 Lift, Drag Coefficients and Strouhal Number

7.3.3.1 Lift coefficients

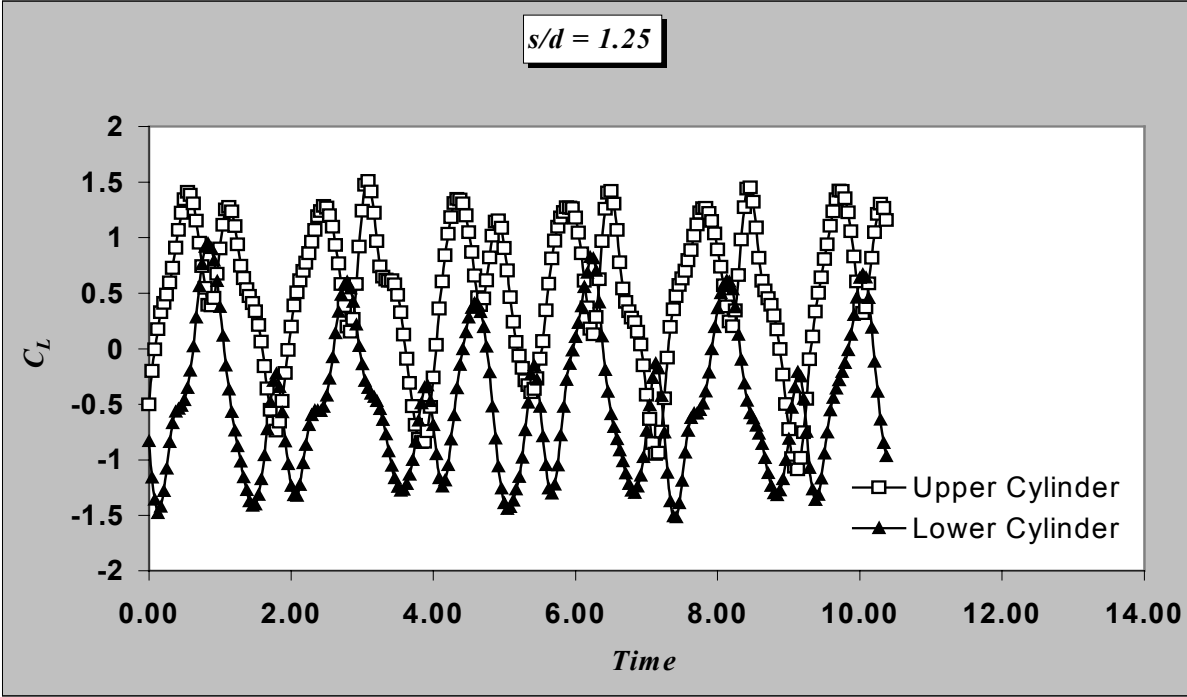
The bistable nature of the flow around two cylinders means that in the range of spacings $s/d \leq 2.0$ there are two bistable forces experienced by the cylinders. Two different forces act on the two cylinders, only for some time, and change over. These forces should always be taken into account. There is an additional feature of the biased flow. The gap flow biased to one side will produce a resultant force on the cylinder, which is deflected relative to the free stream direction. Hence, there will be a component of the force acting perpendicular to the free stream direction, which could be called a lift force.

Figure 7-9 shows the time variation of the lift coefficient for the cases $s/d = 3.0$, and 1.25 . As seen in this graph, the time variation of lift coefficient for first case takes a sinusoidal form. There is a very small phase difference between the two cylinders. This may be due to a

numerical error because of the complexity of the problem. As could be seen, the time variation of C_L for



a)



b)

Figure 7-9 Time history of lift coefficient fluctuation for the cases $s/d = 3.0$ and $s/d = 1.25$.

the lower cylinder is a mirrored image of that for the upper cylinder. In addition, due to the jet flow in the gap, each time variation curve is not symmetric about the gap's centerline.

For the case $s/d = 1.25$ the variation is very different. The time variation of C_L has two different peak values, and a repetitive cycle could only be found every two normal cycles of the case $s/d = 3.0$. For example, due to the biased nature of the flow, the lift coefficient of the upper cylinder takes a minimum value at about $T = 0.88$ and the other minimum is at $T = 1.79$.

7.3.3.2 Strouhal number

For the cases $s/d \geq 2.0$ the calculated Strouhal number was about 0.21. This agrees well with the data found in the literature for two cylinders arranged side by side. The Strouhal number is approximately equal to that of a single cylinder for the range $s/d \geq 2.0$. These results also agree well with those of Ichioka et al. [67]. For the range $s/d \leq 2.0$, we could not characterize a definite value for Strouhal number because the waveform of the lift fluctuation is greatly disturbed and the vortices discharged from the cylinders are no longer generated as a regular Karman vortex street because of the effect of the interference of the interaction between jet stream and vortices.

7.3.3.3 Drag coefficients

As seen in Figure 7-10 for the case $s/d = 3.0$, the drag and lift forces oscillate at different frequencies: the drag has twice the frequency as the lift. The reason (as mentioned before) is that the drag force has one maximum and one minimum during the growth and shedding of each vortex, while the sign of the lift force depends on the location of the vortex i.e. whether it is above or below the cylinder. As expected, for smaller values of s/d , the time variation of C_D loses its waveform but for one cycle, there are usually two minima and two maxima.

Figure 7-11 represents the variation of mean drag coefficient vs. s/d . The mean value for $s/d \leq 2.0$ is obtained by integration over a very long period. For other values of s/d , the integration is done for only one cycle. As seen in the graph, the drag coefficient reaches a minimum value at $s/d \cong 1.75$. It increases again until $s/d \cong 2.0$ and then decreases by increasing s/d . This trend coincides well with the results represented in [57].

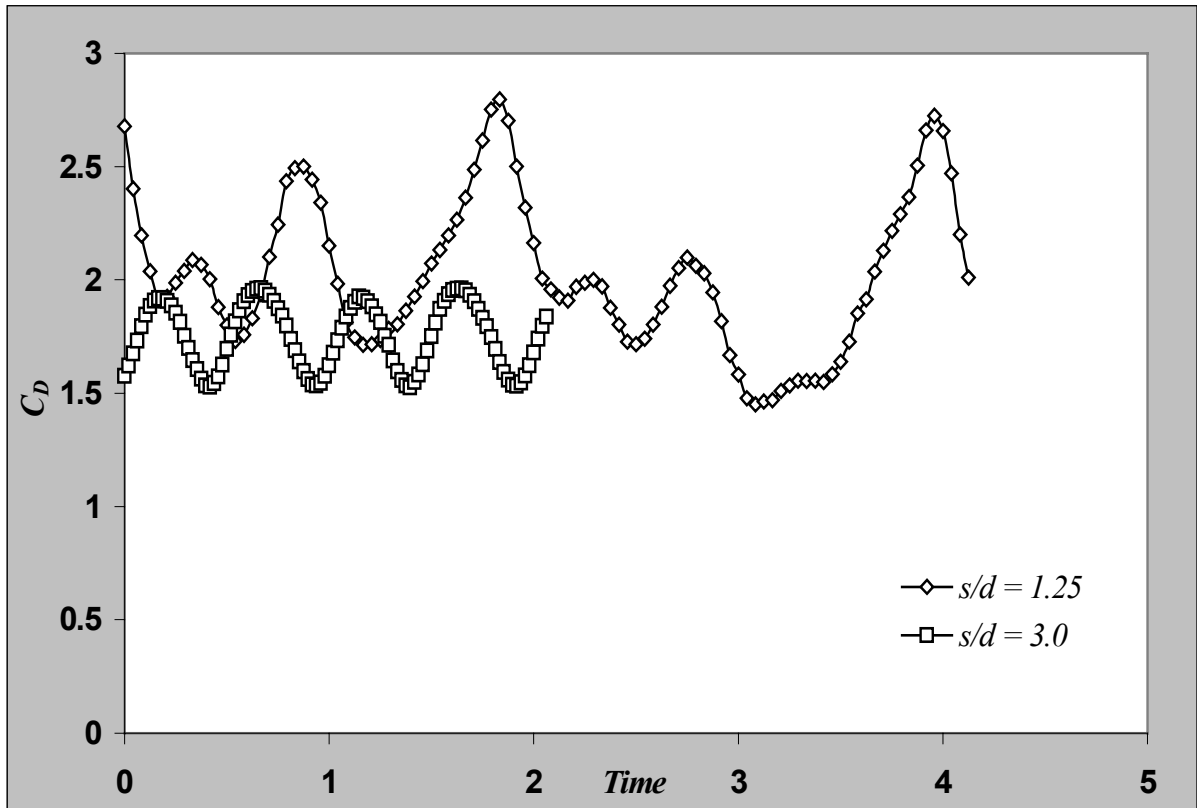


Figure 7-10 Time variation of the drag coefficient of the upper cylinder.

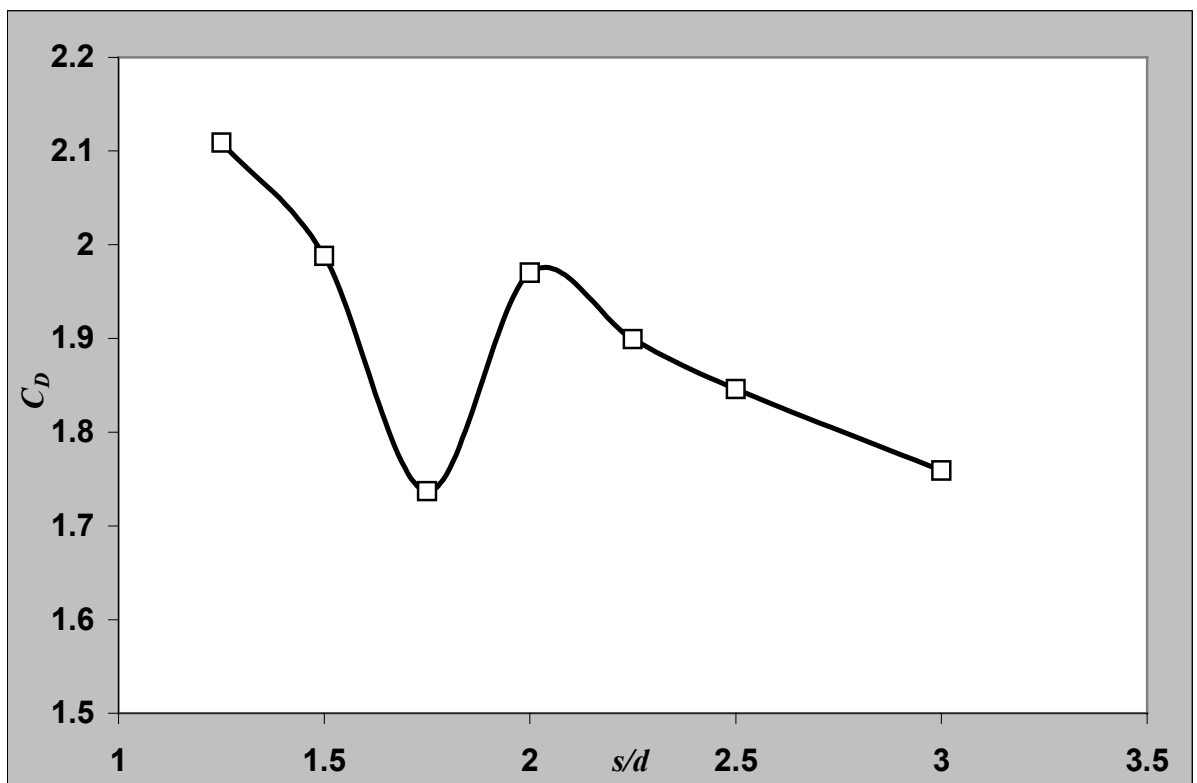


Figure 7-11 Mean drag coefficient vs. pitch to diameter ratio for the case $Re = 500$.

Chapter 8

Heat Transfer Results

Convective heat transfer results are highly dependent on the quality of the predicted flow field. Therefore, a thermal field is a good verification of the accuracy of a predicted flow field, but not necessarily a guarantee. It becomes guaranteed when a good comparison with existing experimental fidelity of the flow field is established. In this chapter, heat transfer results for the cases studied in chapter 7 will be represented as follows:

1. Thermal fields shown by temperature contours;
2. Instantaneous and mean local Nusselt number around the cylinders and
3. Average Nusselt number for both cylinders as a one unit.

All this results will be given as a function of s/d

A temperature difference of 100 K is taken between the cylinders' wall and the free stream in case of constant wall temperature, or a wall heat flux of 10 W/m^2 in case of constant wall heat flux. This should not play any role because the properties of the fluid are taken to be constant.

The solution of the energy equation could be done after getting a converged oscillating solution for the momentum equation. There is no need to solve all equations simultaneously. This will reduce the required total computation time because of the fact, that the flow field is the driver of the thermal field in this type of problems.

8.1 Constant Wall Heat Flux

8.1.1 Thermal Field

As known for forced convection problems, the thermal profile downstream of the cylinder is the legacy of the prediction of the flow profile. Thus, the movement of the thermal field is driven by the motion of the flow field. The reverse is true in the limiting case of natural convection, where the thermal field is the driver. The thermal field in mixed convection is adjusted according to the relative magnitudes of natural and forced convection.

Figure 8-1 shows the normalized instantaneous thermal field as a function of time for one complete cycle of the lift coefficient for the case $s/d = 3.0$. As can be seen, the thermal boundary layer is thinnest at the forward stagnation point as expected. The hottest region is found to be between the two stagnation points. The shape of the forward part of the thermal boundary layer is almost constant with the time and only the part affected by the vortices is changing with time. There are usually three hot spots directly behind each cylinder. The location of two of these hot spots is almost constant with time and is found to be at each separation point. The location of the third hot spot changes its location according to the location of the active vortex behind the cylinder. The thermal field represents clearly the process of the vortex growth and shedding. It is found to be symmetric about the gap centerline. As the used fluid is air (low thermal conductivity), the hot region in the thermal field is found to be very thin.

Figure 8-2 represents the same results but this time for the case $s/d = 2.0$. The thermal field shows a slight asymmetry about the gap centerline. The three hot spots behind each cylinder are still found and behave like in the previous case.

The last case represented by Figure 8-3 shows the thermal field for the case $s/d = 1.5$. The thermal field represents very well the disturbance occurred in the Vortex Street and shows that the vortex shedding process is no longer coupled. There is no symmetry at all around the gap centerline. Sometimes two of the three hot spots disappear so one finds only one spot (e.g. $T=1/8$ at the upper cylinder), or one spot disappears so there are only two spots (e.g. $T=4/8$ at the upper cylinder).

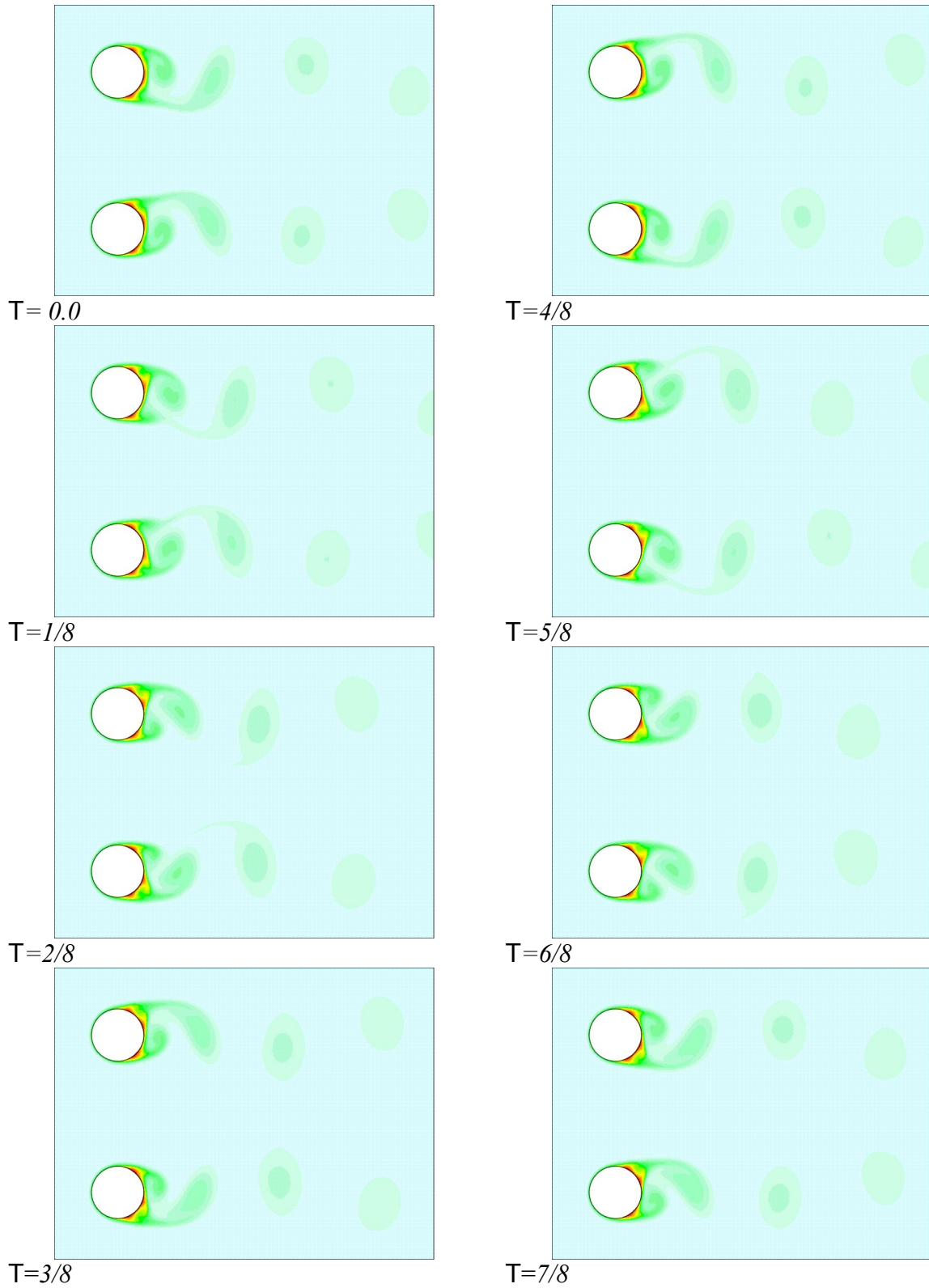
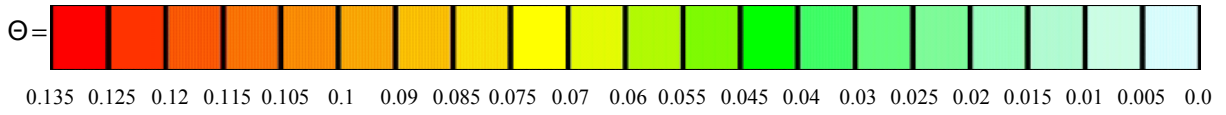


Figure 8-1 Normalized instantaneous thermal field for $s/d = 3.0$.

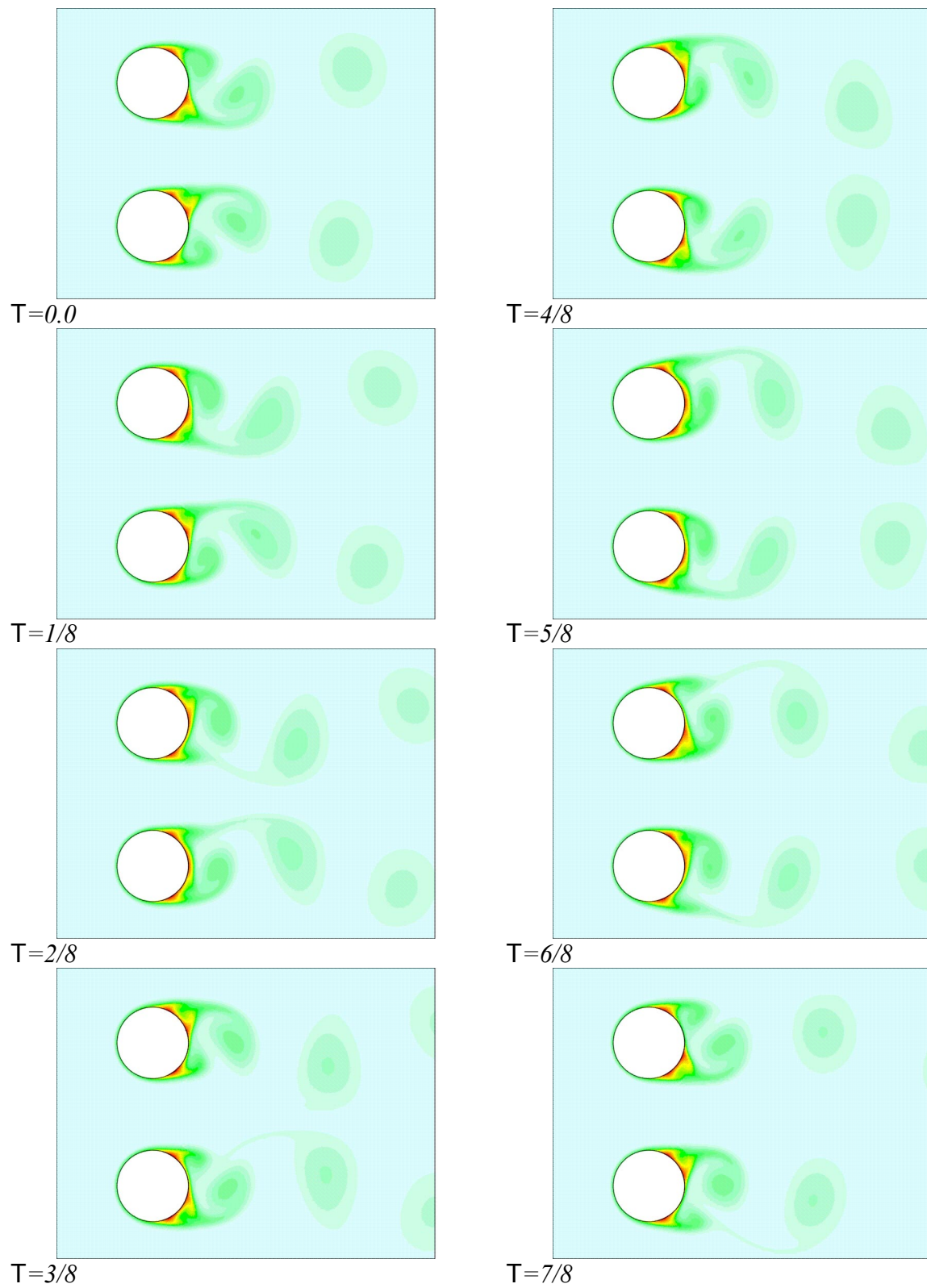
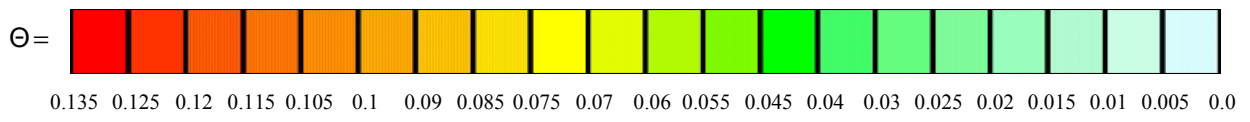


Figure 8-2 Normalized instantaneous thermal field for $s/d = 2.0$.

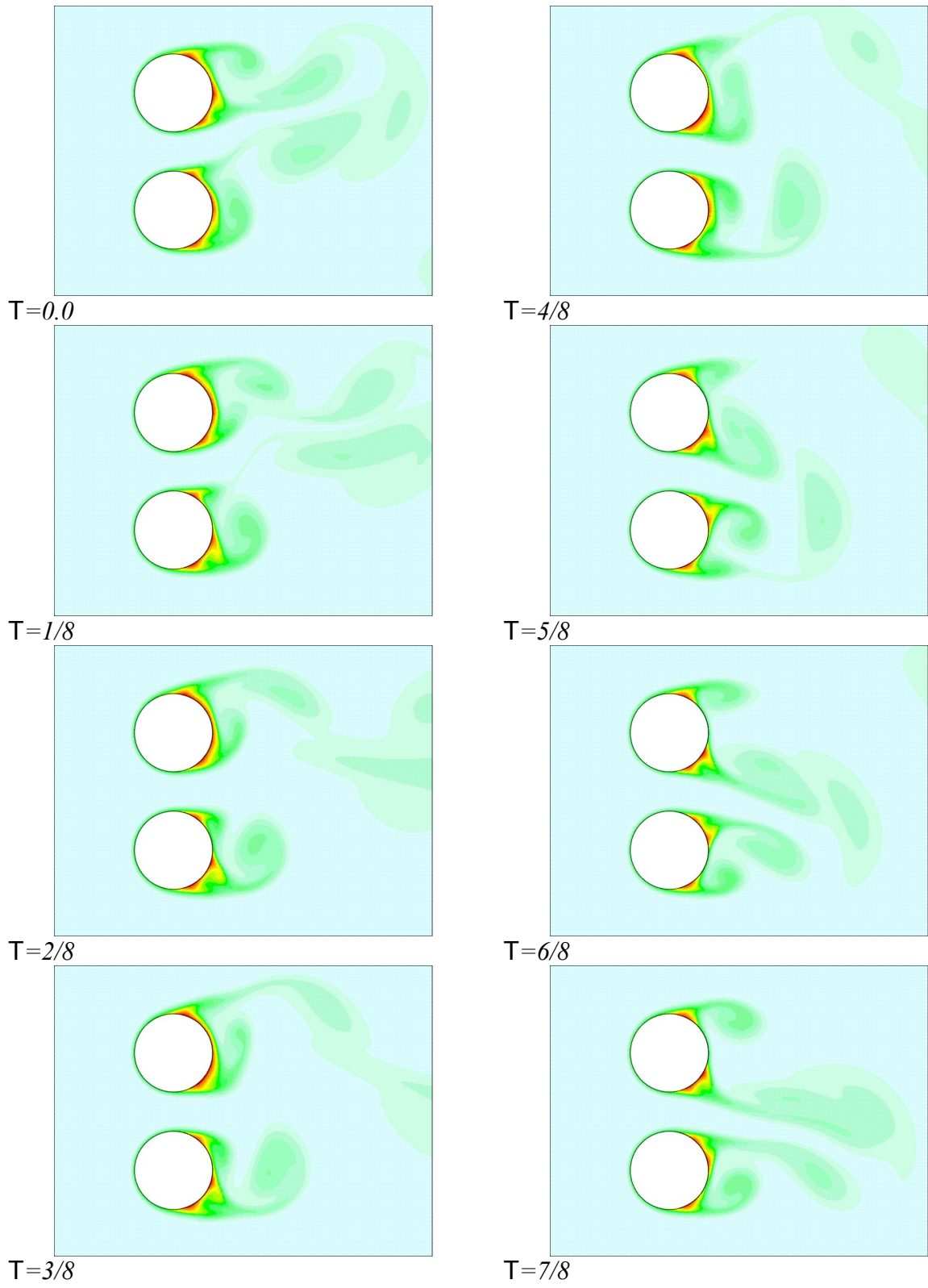
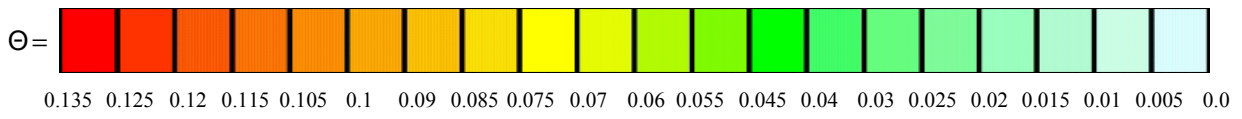


Figure 8-3 Normalized instantaneous thermal field for $s/d = 1.5$.

8.1.2 Local Nusselt Number around the Cylinders

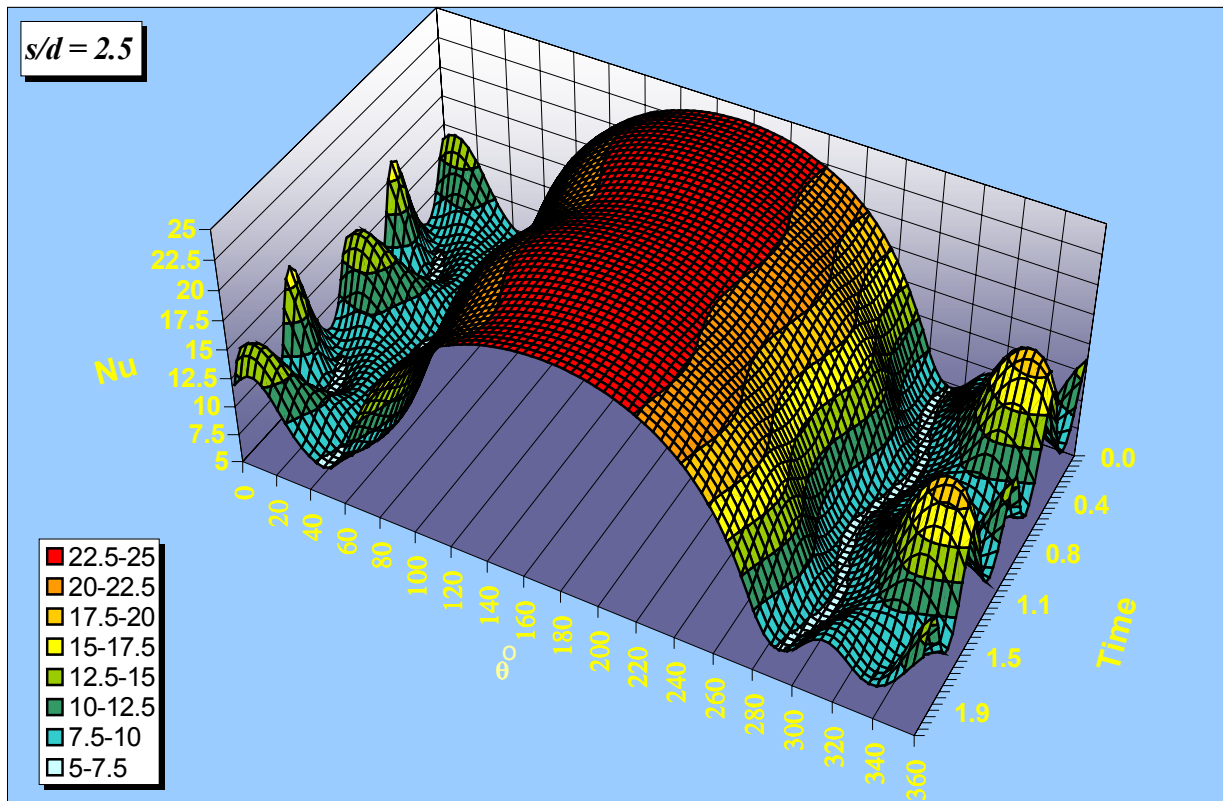
8.1.2.1 Instantaneous local Nusselt number

The local values of the Nusselt number were calculated as follows:

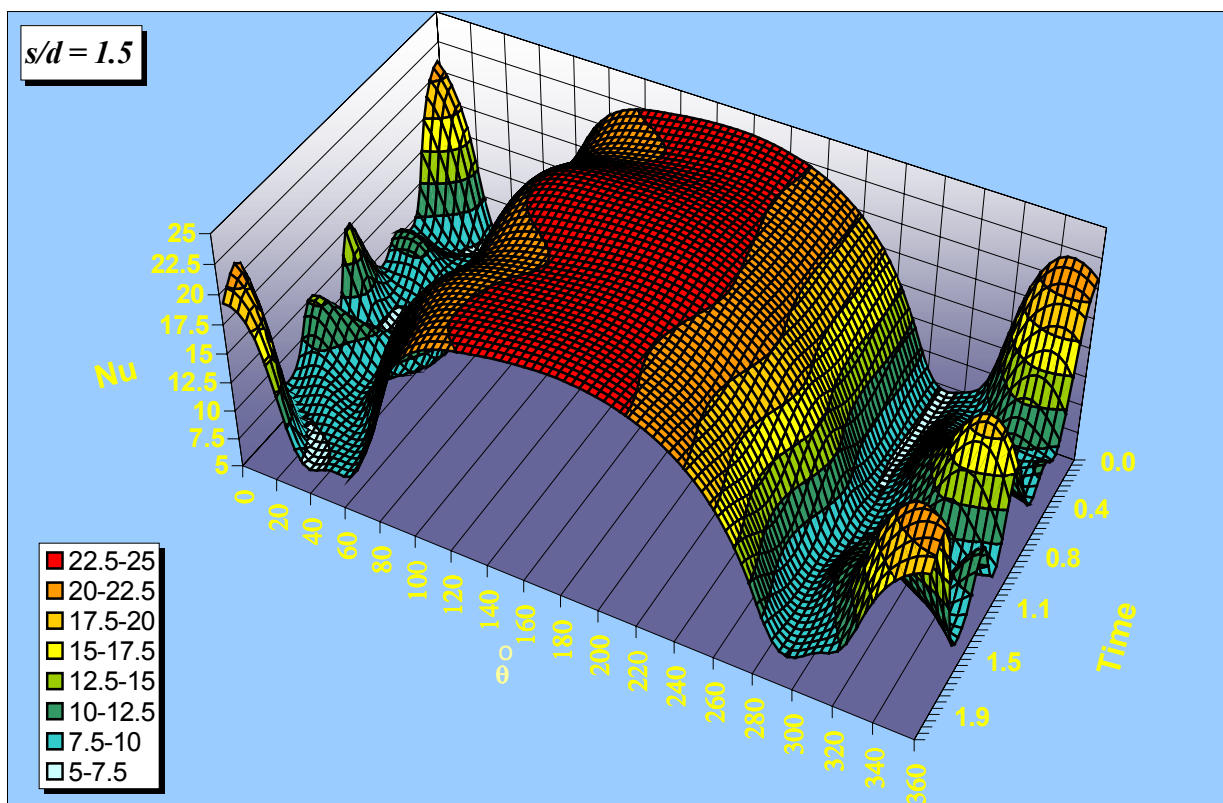
$$Nu_D(\theta, T) = \frac{h(\theta, T)d}{k} = \frac{q_o d / k}{\vartheta_o(\theta, T) - \vartheta_\infty} = \frac{1}{\Theta_o(\theta, T)}. \quad (8.1)$$

Figure 8-4 (a) shows the time behavior of the local Nusselt number calculated at the surface of the lower cylinder for a pitch to diameter ration $s / d = 2.5$. The angle θ is measured from the rear (base) point in the counterclockwise direction. Starting from the point $\theta = 0^\circ$, it is seen that the time variation of the Nusselt number takes a wavy form with two maxima and two minima per one lift coefficient cycle. There is a difference in magnitude between the two maxima but the two minima are almost the same. By increasing θ , the Nusselt number has the same trend with larger deference in magnitude between the two maxima than that at the point $\theta = 0^\circ$. At the point where θ is about 20° , there is one Nusselt number cycle per one lift coefficient cycle with a decrease in the amplitude of fluctuation. This trend remains until the separation point. Then the Nusselt number reaches its minimum with an almost constant value. Going further behind the separation point, it is seen that a rapid increase in Nusselt number accompanied with decayed fluctuations takes place until reaching the forward stagnation point at which the Nusselt number is almost constant with time. By increasing θ more and more, it is found that the Nusselt number is almost symmetric between the two separation points (the upstream part of the cylinder). After reaching the second separation point (at the outer part of the lower cylinder), the change in Nusselt number with the time starts to reverse its trend and two Nusselt number cycles per one lift coefficient cycle take place. It is important to notice that the local values of Nusselt number in the range $290^\circ < \theta < 360^\circ$ are higher than that values in the range of $0^\circ < \theta < 70^\circ$. This is a direct effect of the presence of the second hot cylinder, which decreases the Nusselt number locally in its neighborhood.

Figure 8-4 (b) shows the same results but this time for a pitch to diameter ration $s / d = 1.5$. As expected, the time variation of the Nusselt number at the points located between the two separation points behind the cylinder loses its wavy form. This is because of the flow pattern in this region drives the thermal field as said before. The values of Nusselt number at the



a)



b)

Figure 8-4 Instantaneous Nusselt number on the surface of the lower cylinder for the cases $s/d = 2.5$ and $s/d = 1.5$.

upstream part of the cylinder seems to be similar to the previous case but there is no symmetry about the forward stagnation point. There is an apparent deflection in the change in Nusselt number with θ towards the region behind the cylinder and near to the jet flow. This is because of the stagnation point displacement discussed before which as a result affects the Nusselt number distribution at the surface of the cylinder.

The same results for the upper cylinder will not be repeated. It was found that that for the case of $s/d = 2.5$ a symmetry about the gap axes takes place. For the case $s/d = 1.5$ the symmetry was found to take place only in the upstream part of the cylinder in the region between the two separation points.

8.1.2.2 Mean local Nusselt number

Now the distribution of the mean Nusselt number around the upper cylinder will be given. The mean value of Nusselt number is defined as:

$$Nu_{D,mean}(\theta) = \frac{1}{T_o} \int_0^{T_o} Nu_D(\theta, T) dT \quad (8.2)$$

where T_o is the integration time over which the $Nu_{D,mean}$ is calculated. It is equal to 1.0 (i.e. one complete cycle of the lift fluctuation) in case of sinusoidal variation in $Nu_D(\theta, T)$. For the cases when the variation of lift coefficient loses its wavy time variation it is important to take as much time as possible when calculating the mean value of Nusselt number. Because of the limited computer facilities available, the time taken was 20.0 in all these cases.

It must be stated that the angle θ is measured as before and as a result, the region near the jet lies this time in the range $290^\circ < \theta < 360^\circ$. Figure 8-5 gives the distribution of the mean Nusselt number on the surface of the upper cylinder for the studied values of s/d .

The cases of s/d in the range between 3.0 and 2.0 show no deference in Nusselt number for the points between the forward stagnation point ($\theta = 180^\circ$) and separation point away from the jet flow ($\theta \cong 70^\circ$). In the range $\theta > 180^\circ$ there is a slight difference between the curves of Nusselt number until reaching the second separation point ($\theta \cong 290^\circ$). The region between the base point ($\theta = 0^\circ$) and the separation point away of the jet flow ($\theta \cong 70^\circ$) shows an increase in the local values of Nusselt number as the value of s/d decreases. While in the range between the base point ($\theta = 0^\circ$) and the separation point near the jet flow ($\theta \cong 290^\circ$) there is

no significant change in the local values of Nusselt number with the change in s/d and as stated before, the presence of the second cylinder decreases the local Nusselt number in this region.

As the jet flow becomes biased (i.e. $s/d < 2.0$), the dome shape of Nusselt number loses its symmetry and the effect of the presence of second cylinder becomes more dominant. For the extreme case ($s/d = 1.25$) there is a noticeable drop in the local values of Nusselt number in the region nearer to the second cylinder (i.e. $290^\circ < \theta < 360^\circ$)

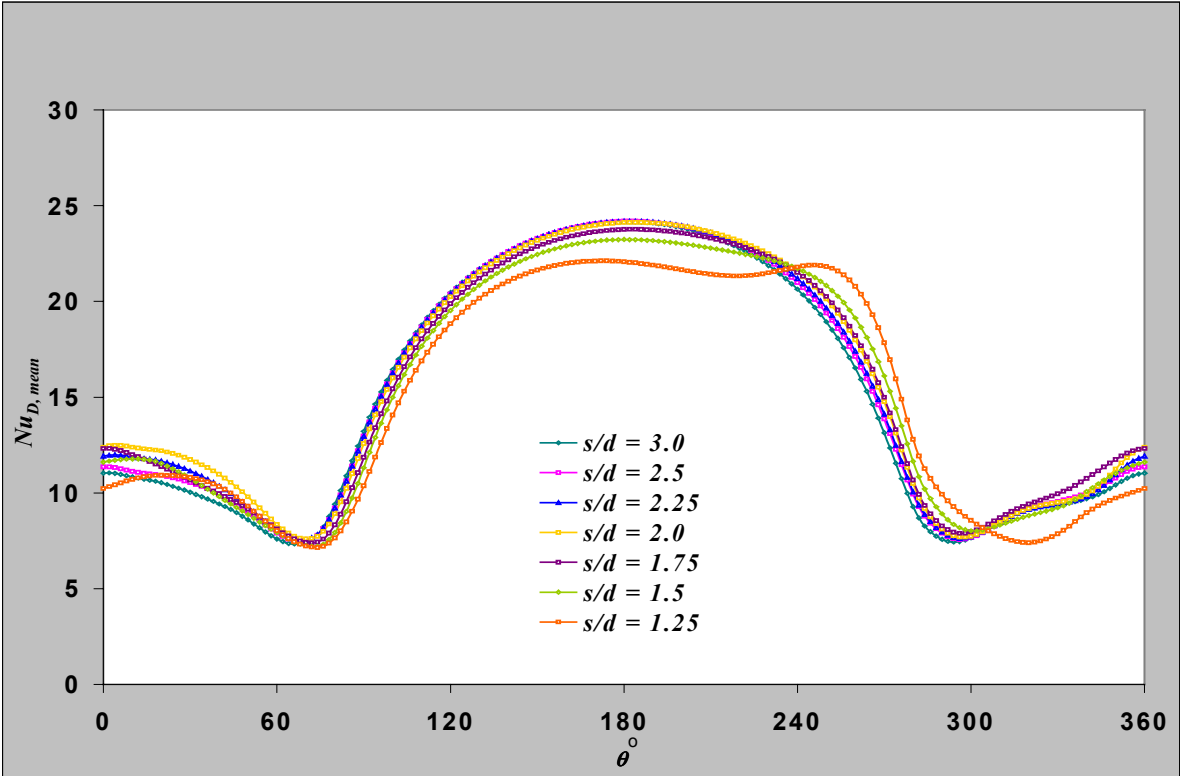


Figure 8-5 Local values of the mean Nusselt number on the surface of the upper cylinder for different pitch to diameter ratios.

8.1.2.3 Mean average Nusselt number

Practically, it is impossible to distinguish between the first and the second cylinder in any practical situation. For the engineers, it is very important to handle both cylinders as one unit and to define $Nu_{D, average}$ as the average total Nusselt number for both cylinders as one unit. It is defined as follows:

$$Nu_{D,average} = 0.5 \left[\left(\frac{1}{2\pi} \int_0^{2\pi} Nu_{D,mean(\theta)} d\theta \right)_{first\ cylinder} + \left(\frac{1}{2\pi} \int_0^{2\pi} Nu_{D,mean(\theta)} d\theta \right)_{second\ cylinder} \right] \quad (8.3)$$

Figure 8-6 shows that the mean average Nusselt number reaches its peak value at a pitch to diameter ratio of about 2.0. This result is very important for engineering aspects because in this case the mean surface temperature of the cylinder surface will be minimum. It is also shown that in the range of $s/d < 2.0$ the change in $Nu_{D, average}$ is very sensitive for the change in s/d , which is not that case when $s/d > 2.0$.

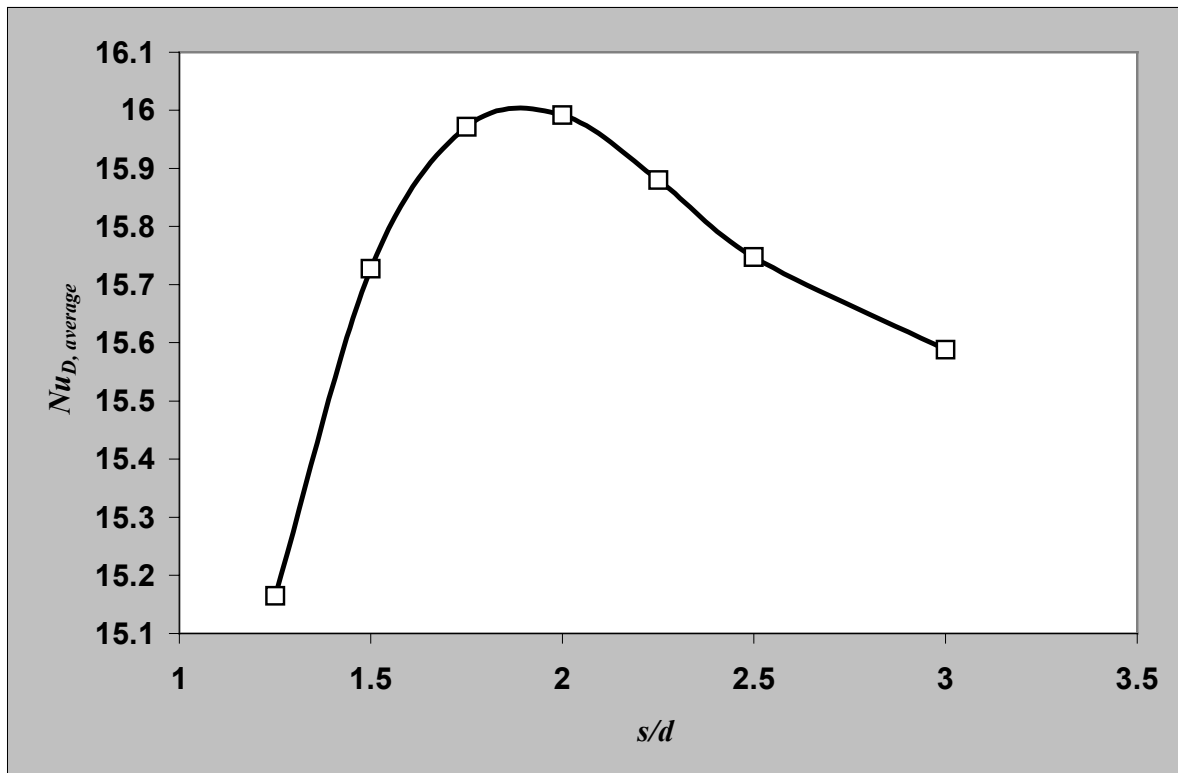


Figure 8-6 Average Nusselt number for both cylinders as one unit V.S. pitch to diameter ratio s/d .

8.2 Isothermal Walls

The second mode of heat transfer used in this analysis for the same case study (i.e. $Re = 500$ and $1.25 \leq s/d \leq 3.0$) will be discussed now. In this mode, the surface temperature of both

cylinders is kept constant during the entire computations. It is important to understand the difference between the two cases:

- In the first case (constant wall heat flux), a certain amount of heat must be removed from the surface of the cylinder and this is done by an increase in the surface temperature over that of the cooling fluid. This increase in the surface temperature is a representation of the quality of the heat transfer process at each surface point (i.e. the higher the surface temperature, the lower heat transfer coefficient)
- In the second case (constant surface temperature), the amount of heat removed from the cylinder is determined by the local values of the heat transfer coefficient (i.e. the higher the heat transfer coefficient, the higher the local heat flux at the surface of the cylinder).

8.2.1 Thermal Field

Like the previous case, we will start to discuss the thermal field at the beginning. Figure 8-7 shows the normalized instantaneous thermal field in case of $s/d = 3.0$ for a one complete cycle of the lift coefficient. As discussed earlier, the flow field is also the driving force of the thermal field. The symmetry about the gap axes is well defined during the whole cycle. Because of the bad thermal properties of the fluid used (air with low thermal conductivity), it is seen that a thin thermal boundary layer is formed around the cylinder in the upstream side of its surface. In addition, the thermal field characterizes the vortex street very well. Also the process of vortices generation and shedding is clearly represented. Behind the cylinders it is seen also that there are three hot spots (like the previous case), two of them are fixed (at separation locations) and the position of the third is depending on the place of generation of the newborn vortex. Figures 8-8 and 8-9 show the thermal field for the rest two case studies ($s/d = 2.0$ and $s/d = 1.5$). As seen, the thermal field is found to be still driven from the flow field. For the three cases it can be seen that the thermal field behind the cylinders is closer to the highest temperature than that where the wall heat flux was constant. This is because of the difference between the two cases where in the case of constant wall temperature, the upstream part of the cylinder has also the highest temperature and this is not the situation when the wall heat flux was constant.

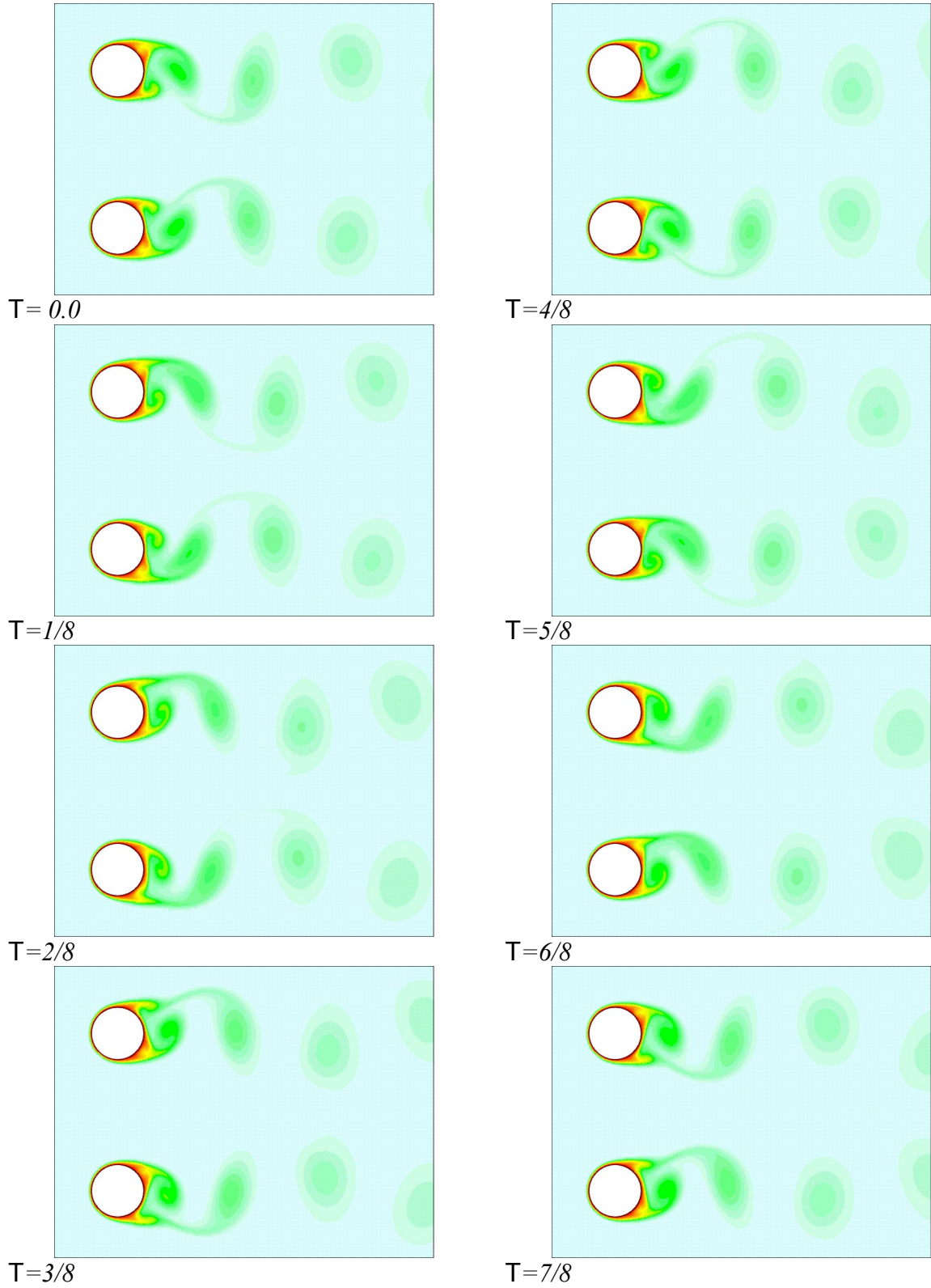
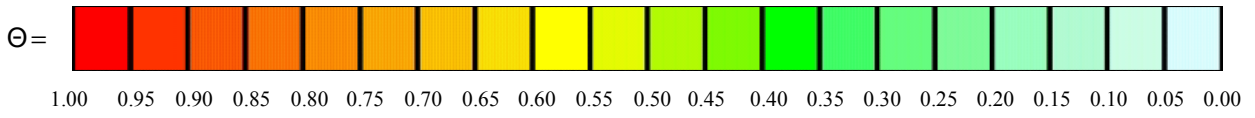


Figure 8-7 Normalized instantaneous thermal field for $s/d = 3.0$.

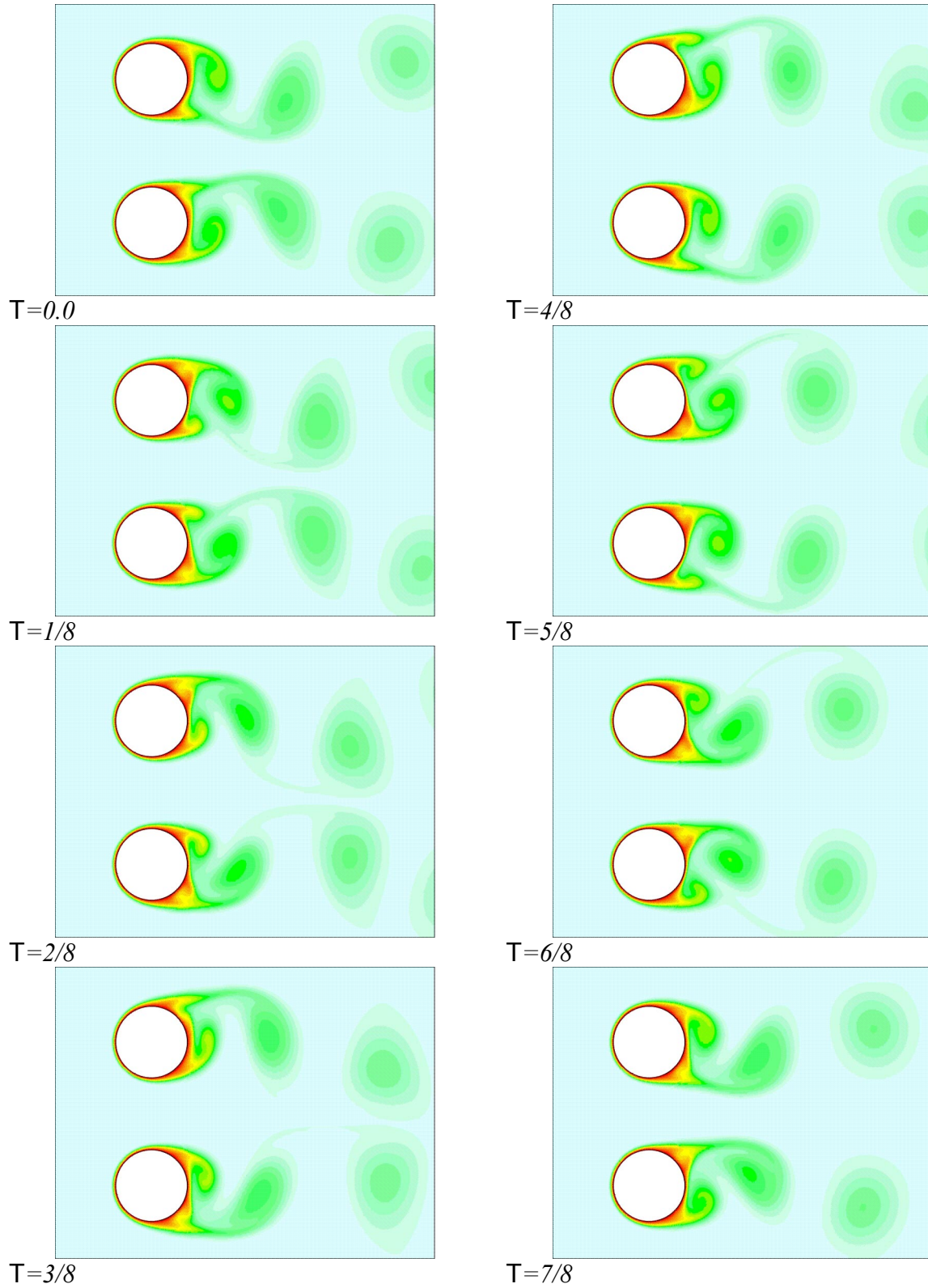
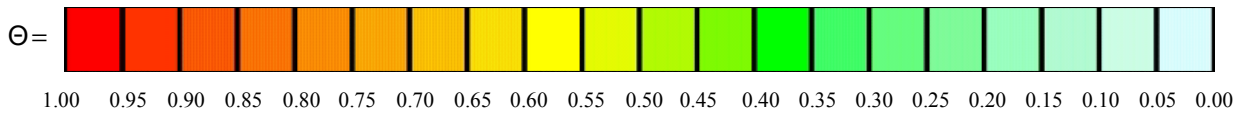


Figure 8-8 Normalized instantaneous thermal field for $s/d = 2.0$.

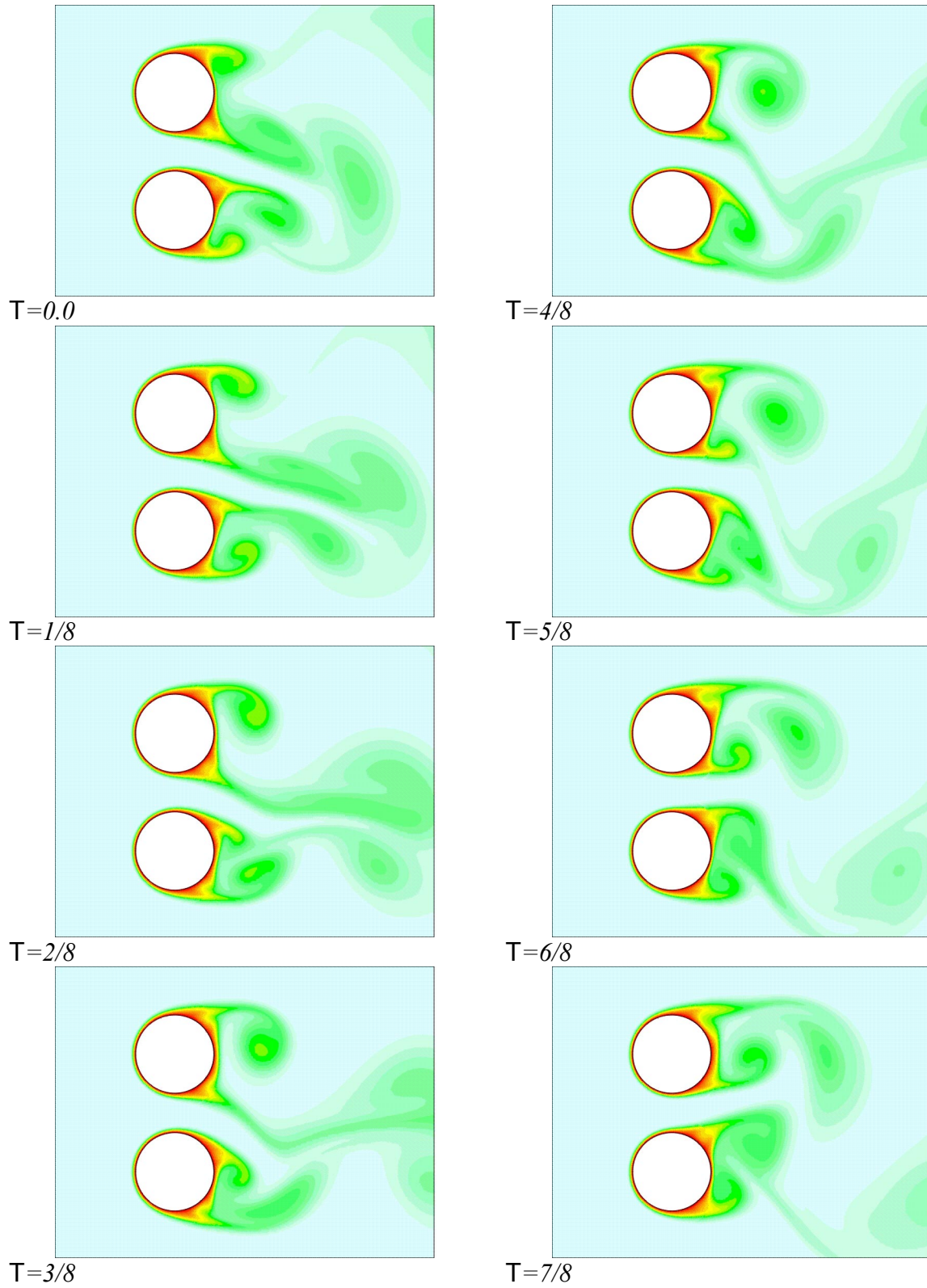


Figure 8-9 Normalized instantaneous thermal field for $s/d = 1.5$.

8.2.2 Local Nusselt Number around the Cylinders

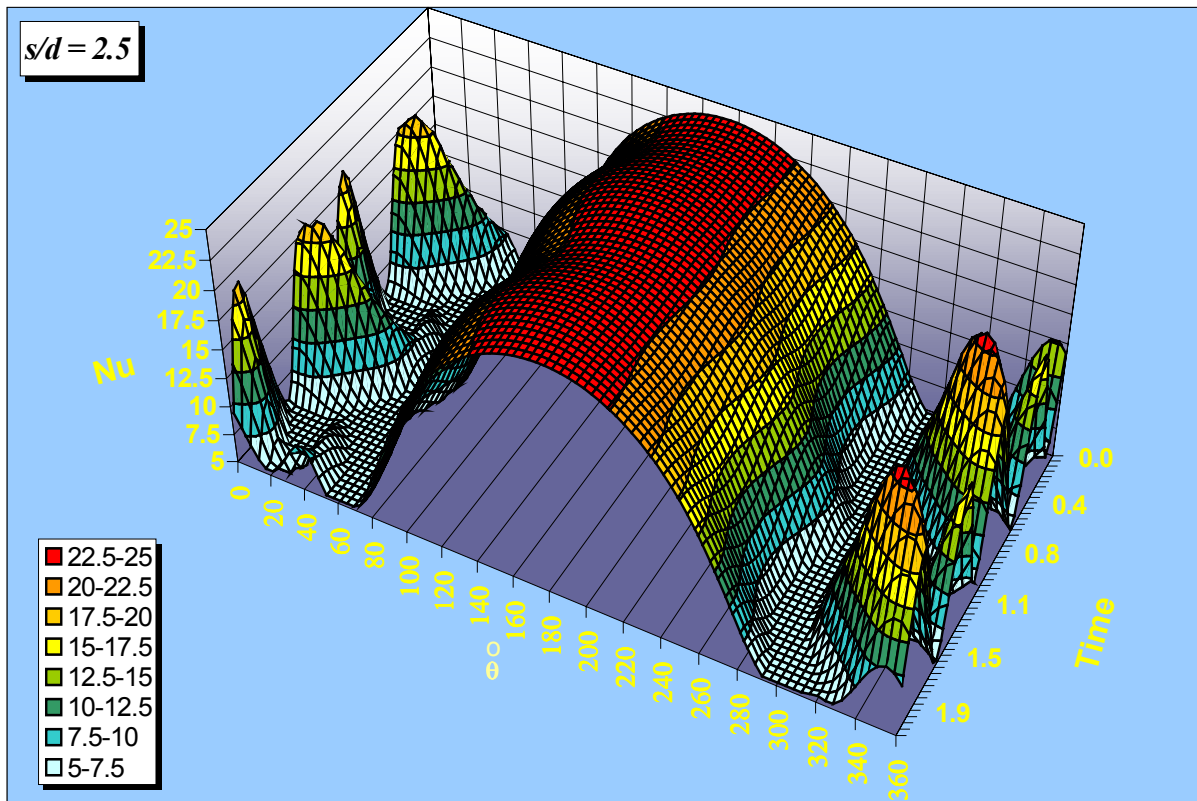
8.2.2.1 Instantaneous local Nusselt number

The local values of the Nusselt number were calculated as follows:

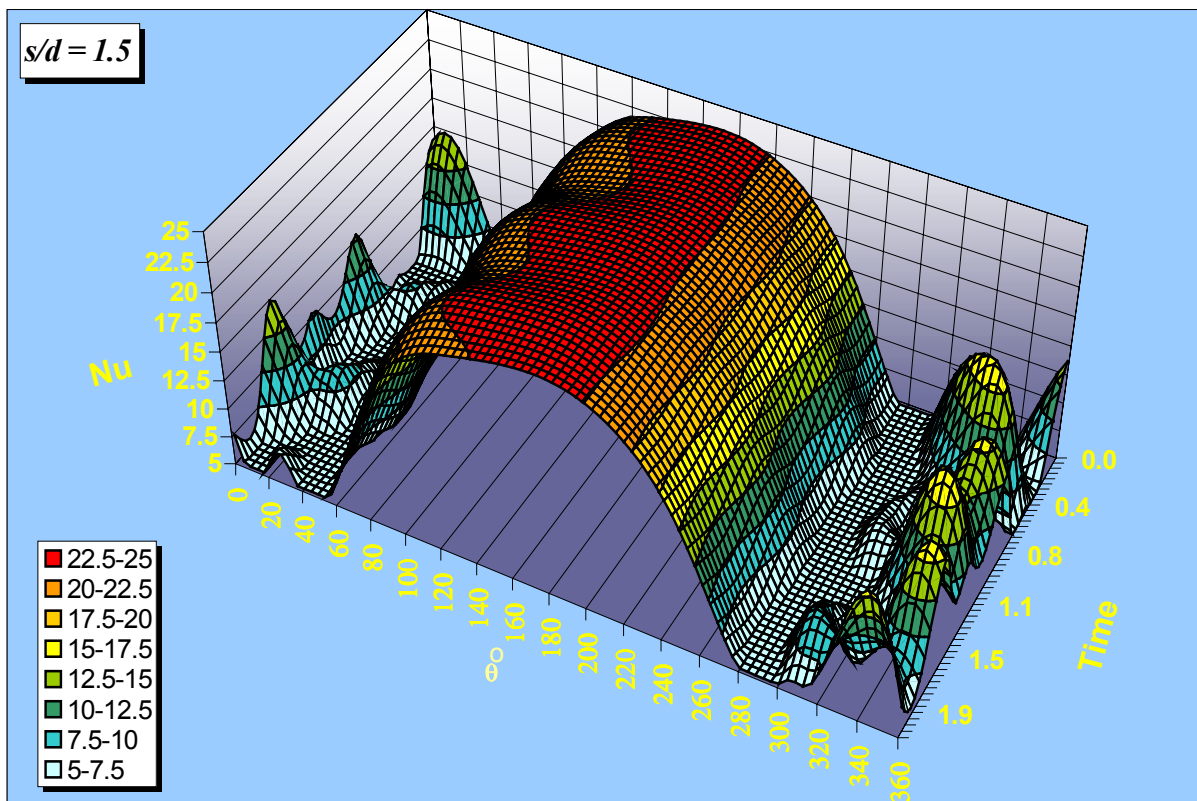
$$Nu_D(\theta, T) = \frac{h(\theta, T)d}{k} \quad (8.4)$$

Figure 8-10a shows the time behavior of the local Nusselt number calculated at the surface of the lower cylinder for a pitch to diameter ration $s/d = 2.5$. The angle θ is measured from the rear (base) point in the counterclockwise direction. Starting from the point $\theta = 0^\circ$, it is seen that the time variation of the Nusselt number has a wavy form with two maxima and two minima per one lift coefficient cycle. Unlike the case of constant wall heat flux, the two maxima are the same. By increasing θ , the Nusselt number has the same trend with two full symmetric cycles per one lift coefficient cycle but the second maximum starts to vanish. At the point where θ is about 20° , there is one Nusselt number cycle per one lift coefficient cycle with a decrease in the amplitude of fluctuation. Like the case of constant heat flux, this trend remains for the reset points. At the separation point, Nusselt number reaches its minimum value with an almost constant time variation. Comparing Figure 8-10a with Figure 8-4a we see that in case of constant wall surface temperature, the local values of Nusselt number around the separation points are lower than that in case of constant wall heat flux. Furthermore, increasing θ leads to a fast increase in Nusselt number accompanied with decrease in time oscillations. Reaching the forward stagnation point, the Nusselt number is almost constant with time and reaches its maximum. In addition, Nusselt number distribution between the two separation points at the upstream part of the cylinder is found to be symmetric about the forward stagnation point. The presence of the second cylinder seems to decrease the local values of Nusselt number in the region nearer to the cylinder. However, the value of the local Nusselt number in the downstream part is generally higher than that in case of constant wall heat flux.

Figure 8-10b shows the same results but this time for a pitch to diameter ration $s/d = 1.5$. The time variation of the Nusselt number at the points located between the two separation points behind the cylinder loses its sinusoidal form. This is a direct reaction of the flow field in this region. The values of the Nusselt number at the upstream part of the cylinder seems



a)



b)

Figure 8-10 Instantaneous Nusselt number on the surface of the lower cylinder for the cases $s/d = 2.5$ and $s/d = 1.5$.

to be similar to the previous case but there is no symmetry about the forward stagnation point this time. There is a marked deflection in the change in Nusselt number with θ towards the region behind the cylinder and near to the jet flow. This is because of the stagnation point displacement discussed before.

8.2.2.2 Mean local Nusselt number

The mean Nusselt number around the upper cylinder is calculated using Equ. 8.2 and is represented in Figure 8.11. The same values of T_o are used like the case of constant wall heat flux. The angle θ is measured, as before starting from the base point behind the cylinder in a counterclockwise direction. The local Nusselt number distribution on the cylinder is almost symmetric about the forward stagnation point for the upstream part of the cylinder for s/d in the range between 2.0 and 3.0. A deflection in the distribution starts to take place by decreasing s/d to values less than 2.0. At $s/d = 1.25$ the deflection of the curve is very clear and the peak value of Nusselt number is reached at an angle of about 260° . The jet flow enhances the heat transfer process at the part of the cylinder surface nearer to it. It is usually accompanied with a decrease in the local values of Nusselt number at the other side away from the jet flow.

In the region behind the cylinder between the two separation points it could be realize that making the cylinders closer to each other usually has no effect till $s/d = 2.0$. Behind this value, it is seen that in the region nearer to the second cylinder (i.e. $290^\circ < \theta < 360^\circ$) there is an increase in the local values of Nusselt number for that case $s/d = 1.75$. By decreasing s/d further more we see a drop in the local values of Nusselt number and it is most clearly represented in the case of $s/d = 1.25$. In the region behind the cylinder and a way from the jet flow (i.e. $0^\circ < \theta < 70^\circ$) it is realized that in the extreme case when $s/d = 1.25$ the local values of Nusselt number are higher than those of the other ratios of s/d . This is due to the fact that at this pitch to diameter ratio, more cold fluid prefers not to go through the gap between the cylinders due to the increased hydraulic resistance, which gives the part of the cylinder away from the jet better heat transfer conditions.

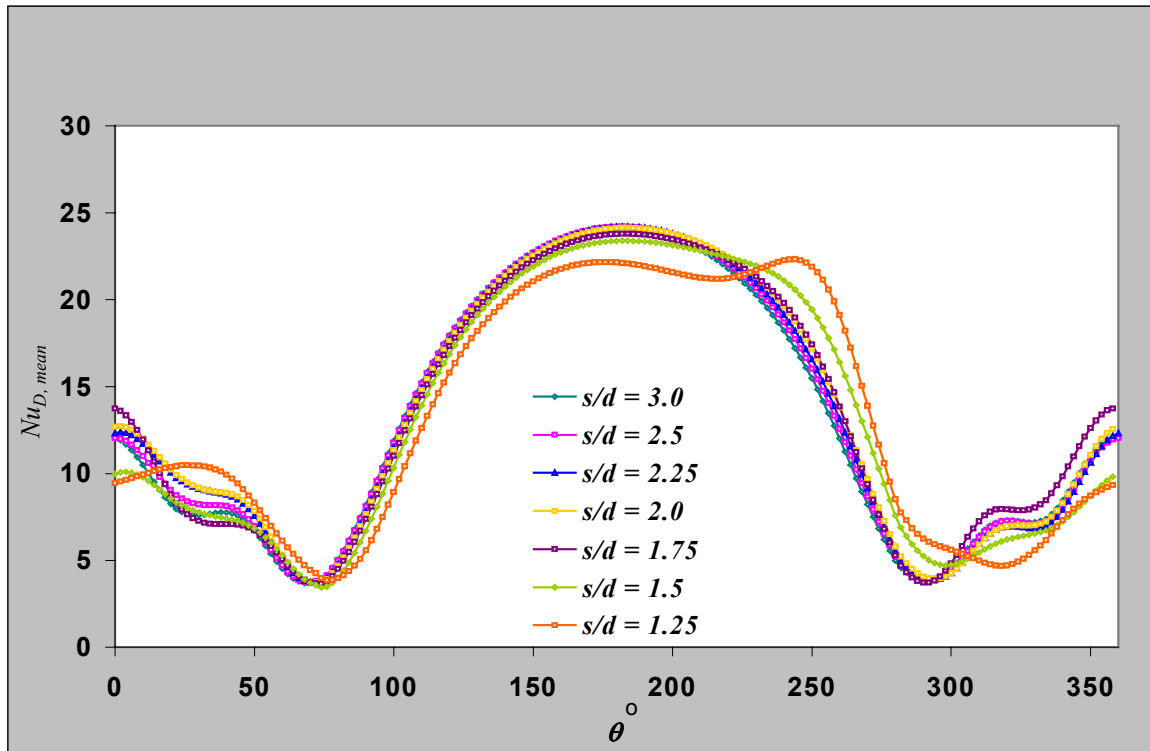


Figure 8-11 Local values of the mean Nusselt number on the surface of the upper cylinder for different pitch to diameter ratios.

8.2.2.3 Mean average Nusselt number

For the same reasons listed in 8.1.2.3, the average Nusselt number for both cylinders as one unit will be illustrated. Figure 8-12 gives the average Nusselt number for both cylinders as one unit vs. pitch to diameter ratio s/d . Like the previous case, the Nusselt number reaches its maximum value when s/d takes a value of about 2.0. The change in Nusselt number shows a little dependence on the change in s/d but for optimization reasons it is recommended to take $s/d = 2.0$ because at this value the heat transfer rate from the cylinders reaches its maximum.

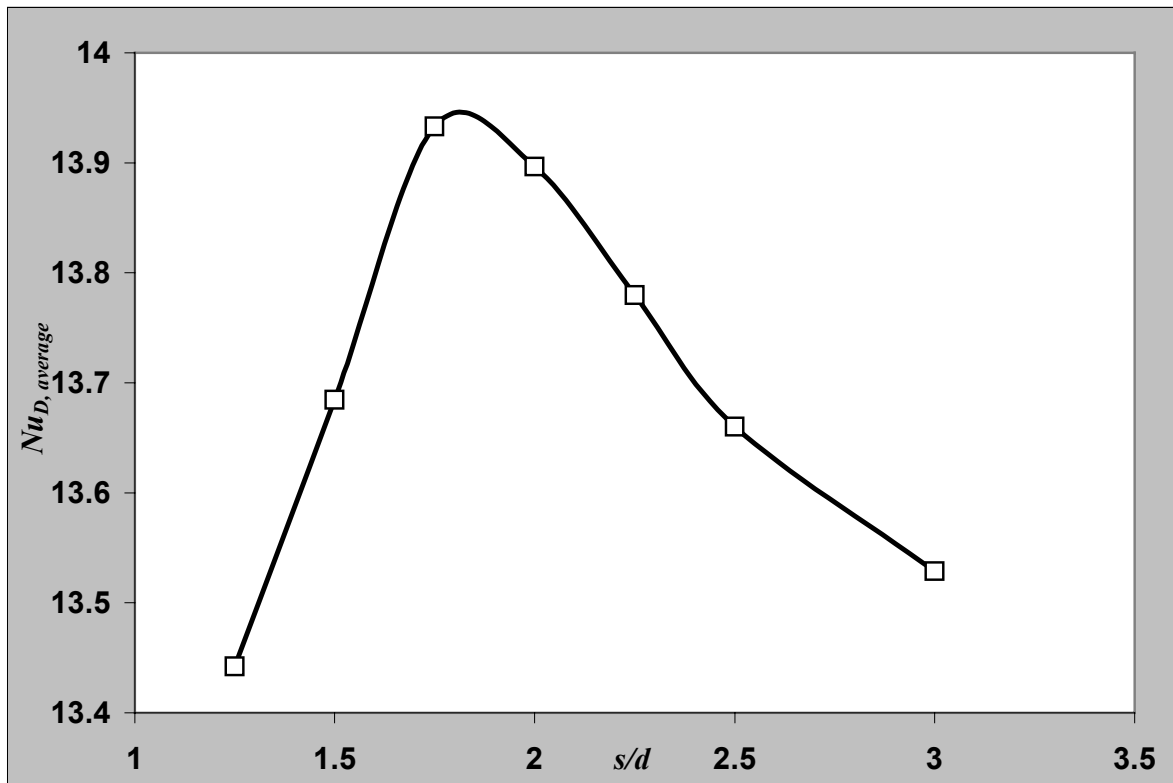


Figure 8-12 Average Nusselt number for both cylinders as one unit V.S. pitch to diameter ratio s/d .

Chapter 9

Effect of Reynolds Number on Heat Transfer Characteristics

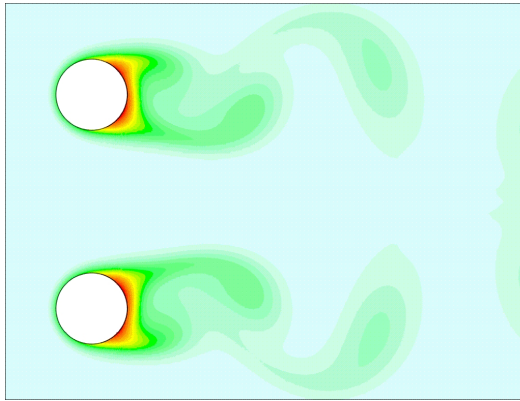
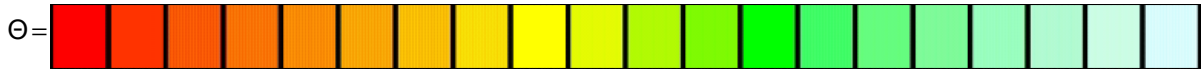
In this chapter, the effect of Reynolds number on the heat transfer characteristics will be studied for both cases, the problem of constant wall heat flux and of isothermal walls. Again, the same range of pitch to diameter ratio s/d will be of interest. The thermal field as well as the Nusselt number will be calculated in order to explain the effect of Reynolds number on the heat transfer behavior of this problem.

9.1 Constant wall heat flux

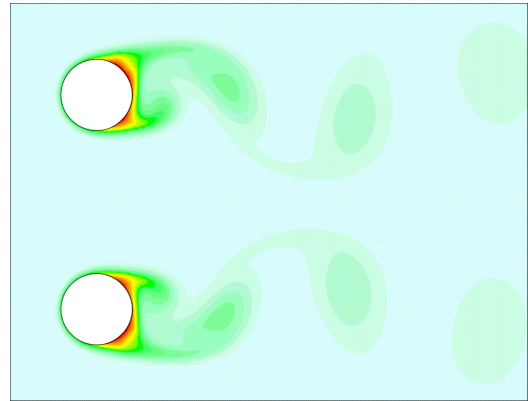
9.1.1 Thermal Field

Figure 9-1 shows the normalized instantaneous thermal field for the case of pitch to diameter ratio $s/d = 3.0$ and have Reynolds numbers ranging from 100 to 500. Starting with the case $Re_D = 100$ it is seen that the wake behind the cylinders is relatively hot. The red-yellow regions prove this statement. The thermal field corresponds also to the flow field (the vortex street) and the coupled vortex shedding between the two streets is to be realized. By increasing the Reynolds number, the wake behind the cylinders becomes cooler in comparison to the previous case. By further increase of the Reynolds number, the effective hot region behind the cylinders becomes smaller. This can be shown particularly for the case of $Re_D = 500$ where the length of the first vortex attached to the cylinder is the shortest one. From the previous, the following statements could be summarize:

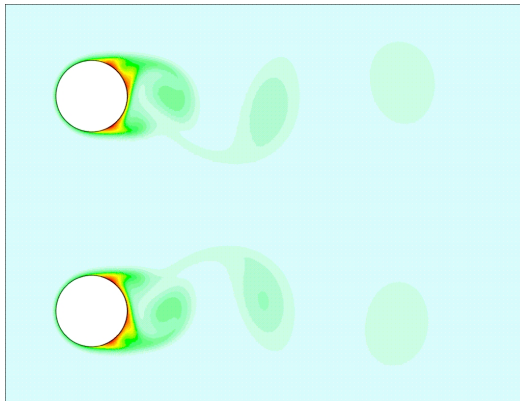
1. The coupled vortex street takes place for the range of Reynolds numbers under study.
2. The wakes behind the cylinders become colder by increasing the Reynolds number.



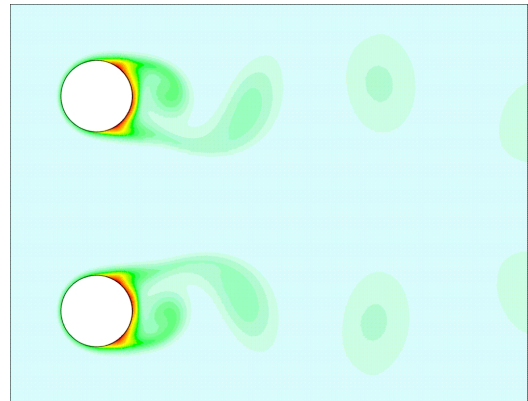
a) $Re_D = 100$



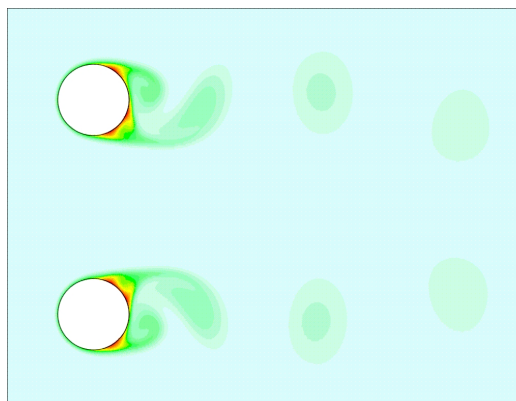
b) $Re_D = 200$



c) $Re_D = 300$



d) $Re_D = 400$



e) $Re_D = 500$

Figure 9-1 Normalized instantaneous thermal field for the cases $s/d = 3.0$ and Re_D ranging from 100 to 500.

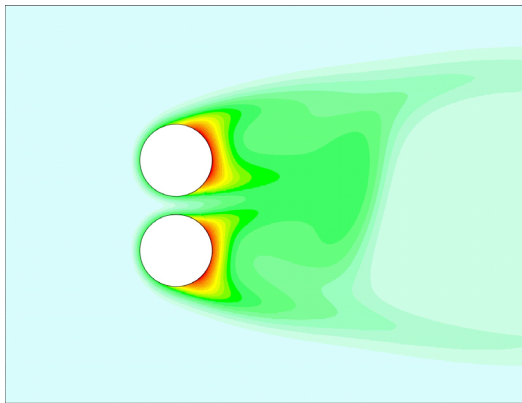
Figure 9-2 shows the thermal field when the pitch to diameter ratio s/d is reduced to 1.25. A very interesting result is found for the case a) when the Reynolds number takes a value of 100. This diagram shows that the biased effect of the jet between the cylinders does not take place at this value of Reynolds number. Only a very weak jet between the cylinders can be seen and the rest of the flow prefers to surround the cylinders building a relatively hot region behind these bodies. The time dependent behavior of this thermal field (which is not illustrated) showed no big changes in the wake shape with the time.

By increasing the Reynolds number to 200, the so-called biased flow starts to occur again. It is seen that the irregularity in the flow behind the cylinder begins and the cylinder surface get colder by rising the Reynolds number. Any growth in Reynolds number leads to a shorter hot wake behind the cylinders. From the above results, the following statements could be summarize:

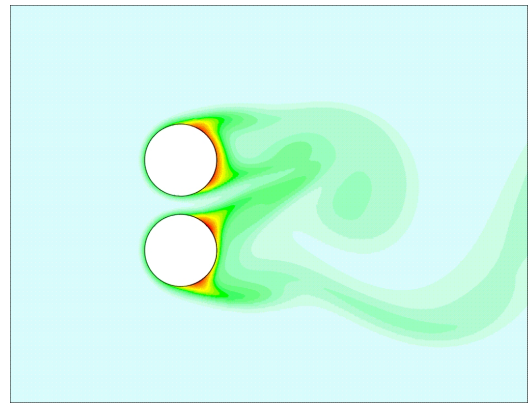
1. At Reynolds number equals to 100, there is almost no biased jet flow between the cylinders and a large hot region behind the two cylinders is formed.
2. By increasing Reynolds number, the biased flow becomes more dominant.
3. Any growth in Reynolds number is accompanied with a shorter hot wake behind the cylinders.
4. For the whole range of Reynolds numbers under consideration -except that at Reynolds number of 100- there is an irregularity in the flow and no definite vortex street could be described.

9.1.2 Mean Local Nusselt Number

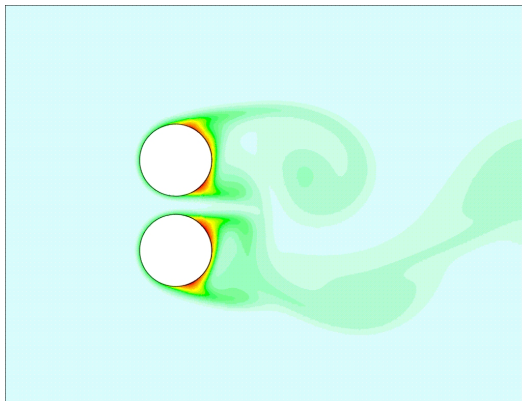
To study the effect of changing Reynolds number on the heat transfer phenomenon from the cylinders' surfaces to the air stream, the local mean Nusselt number defined by Equ. (8.2) will be characterized in Figure 9-3. This figure represents the mean local Nusselt number calculated at the surface of the lower cylinder. The two bounding values of s/d were chosen and the whole range of Reynolds numbers under consideration is shown.



a) $Re_D = 100$



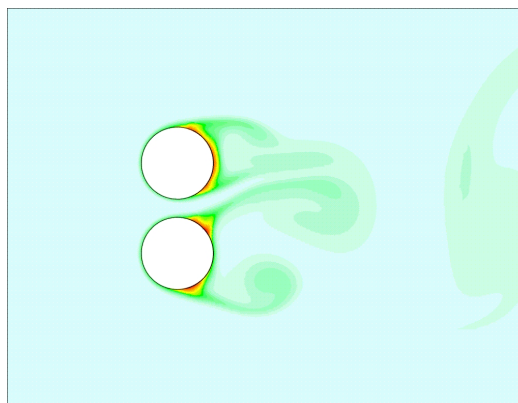
b) $Re_D = 200$



c) $Re_D = 300$



d) $Re_D = 400$



e) $Re_D = 500$

Figure 9-2 Normalized instantaneous thermal field for the cases $s/d = 1.25$ and Re_D ranging from 100 to 500.

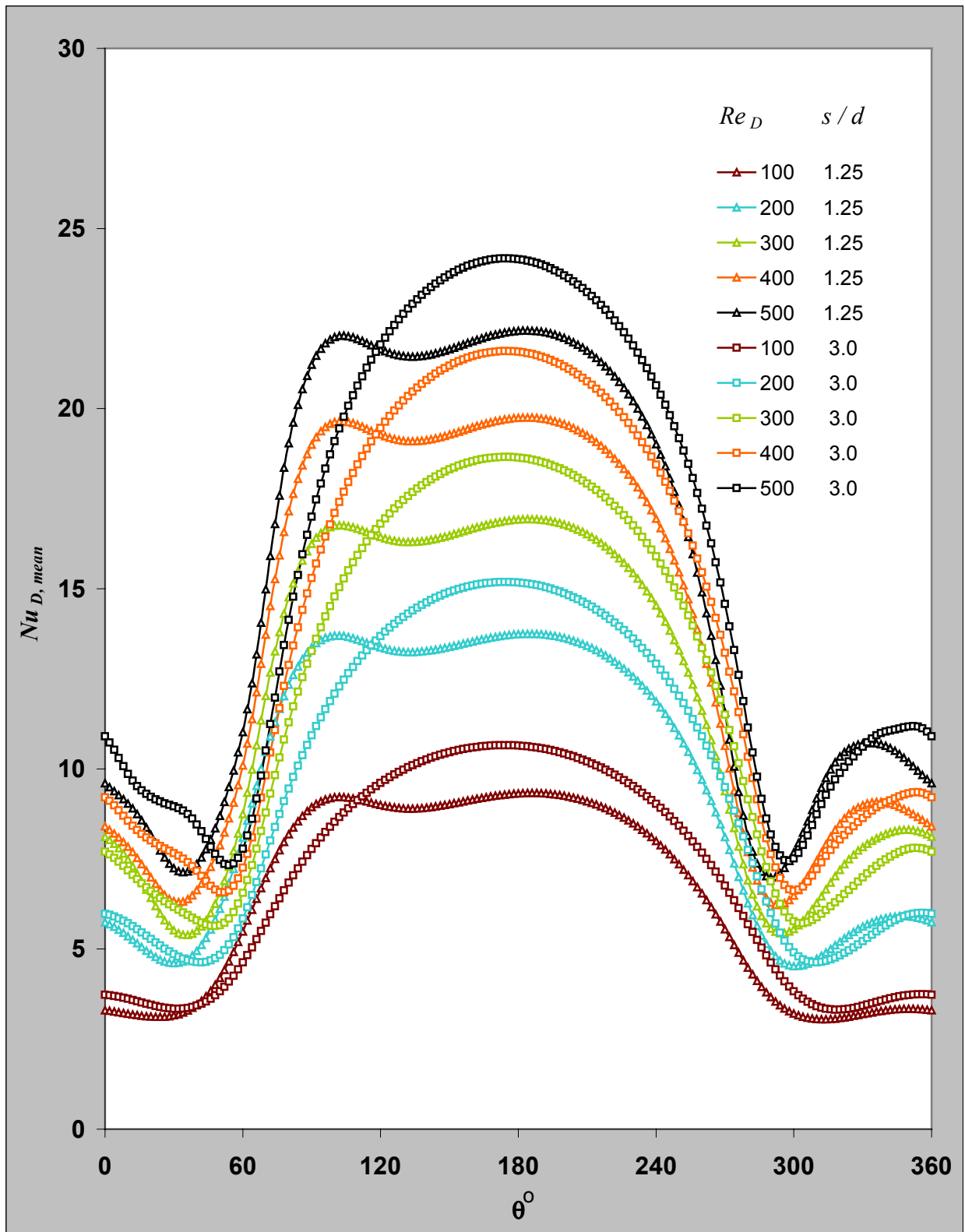


Figure 9-3 Local values of the mean Nusselt number on the surface of the lower cylinder for $s/d=1.25$ and 3.0 and Reynolds number ranging from 100 to 500 .

Starting with a Reynolds number of 100, it is seen that for the case of $s/d = 3.0$ the Nusselt number is almost symmetric between the two separation points in the upstream part of the cylinder. Behind the cylinder in the wake, the Nusselt number changes slightly from the value at the separation point till that at the rear (base) point. At $s/d = 1.25$ the Nusselt number distribution is shifted towards the jet due to the shift of the stagnation point. The Nusselt number is in general lower than that of $s/d = 3.0$ in the range away from the jet and higher near the jet. This is due to the enhancements in the heat transfer process associated with the increased jet velocity.

By increasing the Reynolds number up to 200, there is a noticeable growth in Nusselt number. The improvement in Nusselt number is found to be non-linearly proportional all over the cylinder surface. For example, the increase in Nusselt number at the region around the stagnation point is found to be about 50% while that at the region near the separation point is found to be about 25%. At the downstream part of the cylinders between the two separation points, there is an increase in Nusselt number toward the rear (base) point. This increase is more dominant due to the increased effect of vortex shedding on the heat transfer process by increasing the value of Reynolds number. The shift in the Nusselt number distribution toward the stagnation point in the case of $s/d=1.25$ is found to enhance the heat transfer process in this region (near the stagnation point). The rest of the cylinder surface away from the jet suffers from a low value of Nusselt number.

By rising the value of Reynolds number the same trend continues. The noticeable change is found to take place in the region behind the cylinder. The increase of Reynolds number leads to a changing behavior of the Nusselt number distribution in this region. For example, in case of $Re_D = 100$ there is a slight change in Nusselt number at the region of the cylinder surface between the two separation points behind the cylinders. At $Re_D = 500$, there is a very noticeable change in Nusselt number in this region. In addition, as the cylinders get closer to each other, the peak value of Nusselt number in the region behind the cylinder does not occur at the rear (base) point but the position changes to be at:

$$\theta \cong 332^\circ \quad \text{when } Re_D = 500,$$

$$\theta \cong 338^\circ \quad \text{when } Re_D = 400 \text{ and}$$

$$\theta \cong 350^\circ \quad \text{when } Re_D = 200.$$

9.1.3 Mean Average Nusselt Number

As previously defined in Chapter 8 by Equ. (8.3), this Nusselt number is of great interest for the design purposes. Figure 9-4 shows the average Nusselt number for both cylinders versus pitch to diameter ratio s/d for different values of Reynolds number (Equ. (8.3)). As seen, there is usually a local peak in Nusselt number at $s/d \cong 2.0$ for the whole range of Reynolds number under consideration. The effect of increasing the distance between cylinders is more remarkable for larger values of Reynolds number. According to these results one can conclude that for design purposes, the most appropriate pitch to diameter ratio is to be around 2.0 which gives the most effective heat transfer coefficient between the cylinders and the air stream.

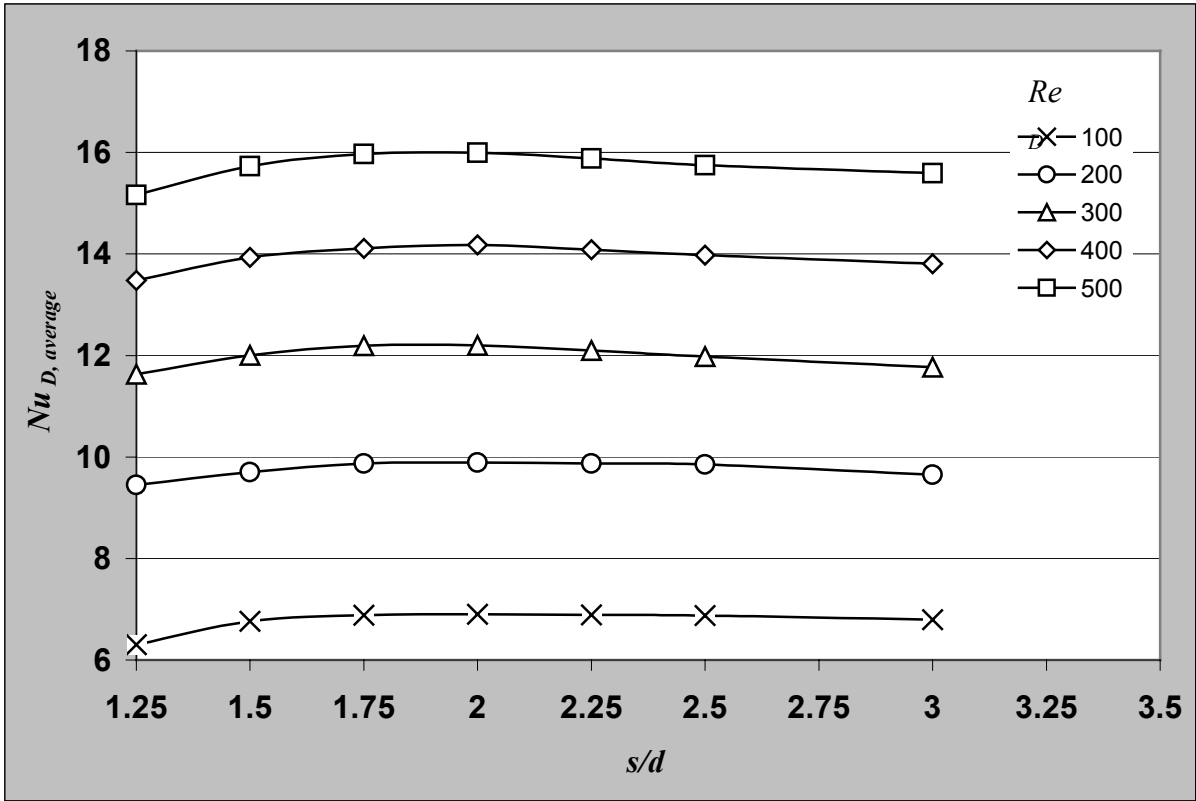


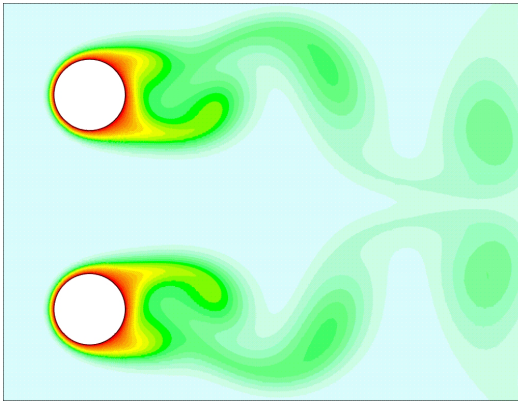
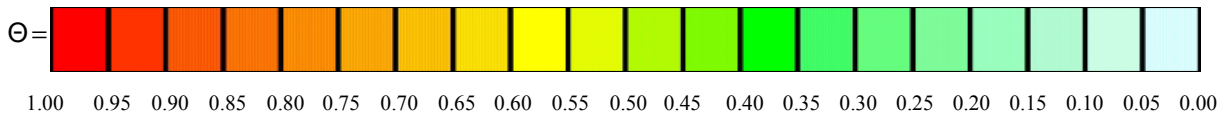
Figure 9-4 Average Nusselt number for both cylinders as one unit versus pitch to diameter ratio s/d for different values of Reynolds number.

9.2 Isothermal Walls

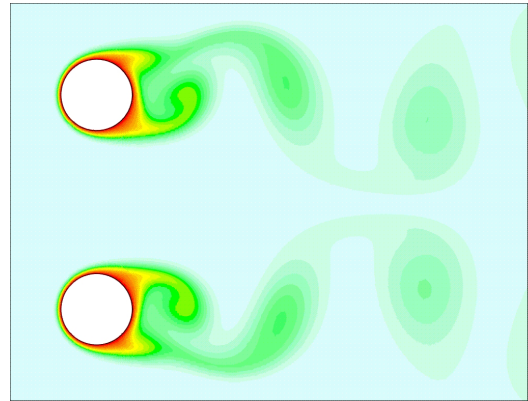
9.2.1 Thermal Field

The thermal field results for the case of isothermal walls, $s/d = 3.0$, and different values of Reynolds number are represented in Figure 9-5. In case of Reynolds number equal to 100 , the thermal boundary layer at the upstream part of the cylinder is clearly thinner than at the downstream part. The vortex streets are very well seen coupled and symmetric. At Reynolds number of 200 , the thermal boundary layer at the upstream part of the cylinder becomes thinner. At the downstream part, the hot region behind the cylinders is smaller. The distance between the vortex centers in the street will be shorter. By increasing Reynolds number more and more until reaching the value of 500 , it is very well seen that the thermal boundary layer at the upstream part is in its thinnest situation. At the downstream part, the hot region of the street is the shortest one. The enhancement of the heat transfer process in the downstream part of the cylinders is very well noticeable at the higher values of Reynolds numbers. This can be realized by comparing Figures 9-5-a and 9-5-e together.

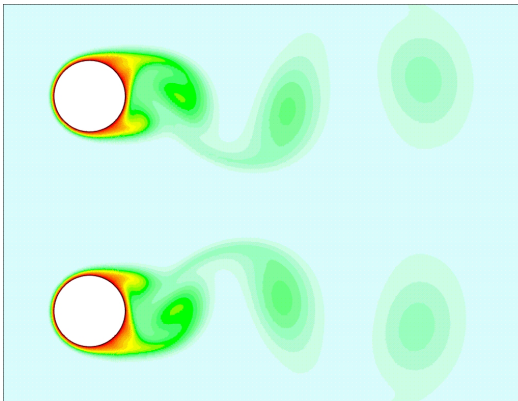
Figure 9-6 show the thermal field but this time for $s/d = 1.25$. In case of Reynolds number 100 , the biased flow is found to have a minimum effect on the thermal properties of the field behind the cylinders. As seen in Figure 9-6-a, there are almost no vortex streets behind the cylinders. The hot region behind the upper cylinder changes its place with time to move towards the lower one. By increasing Reynolds number to 200 , the irregularity in the flow field starts to take place. This is reflected directly on the thermal field. Increasing Reynolds number further more results in a strong presence of the biased flow. This could be noticed in Figure 9-6-d. At Reynolds number 500 , it is also seen that the hot region behind the cylinders is now smaller compared to the previous cases. For all values of Reynolds numbers except 100 , there was an irregular flow pattern behind the cylinders. No vortex streets could be defined.



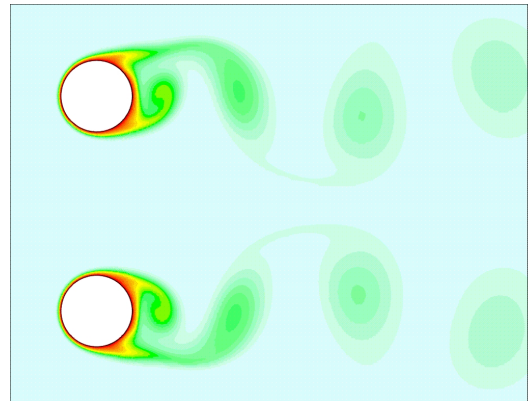
a) $Re_D = 100$



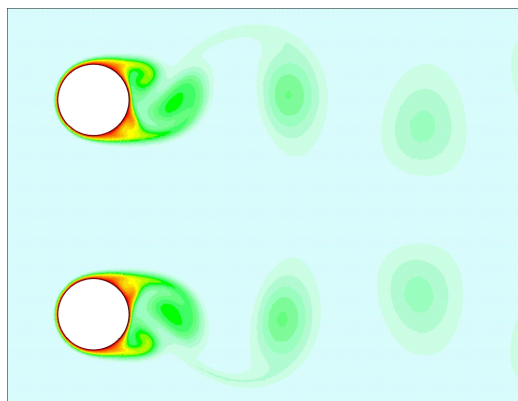
b) $Re_D = 200$



c) $Re_D = 300$

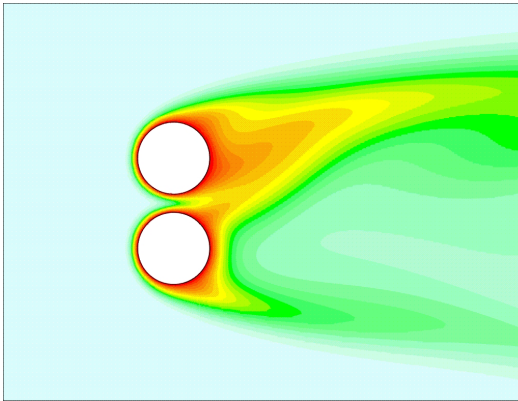
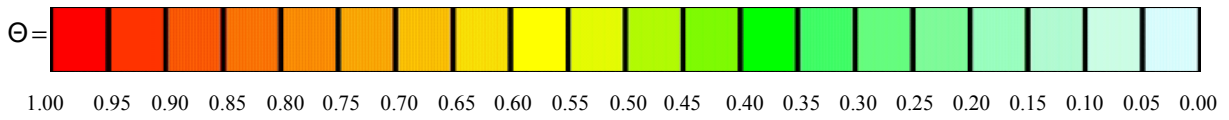


d) $Re_D = 400$

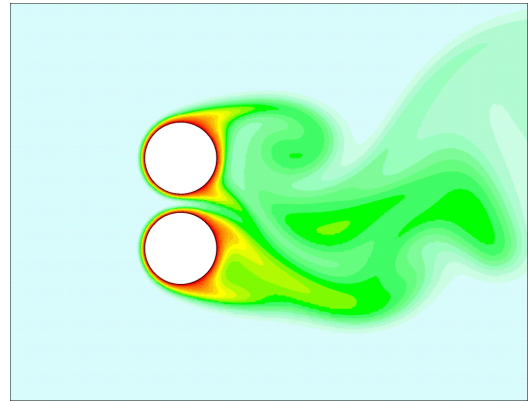


e) $Re_D = 500$

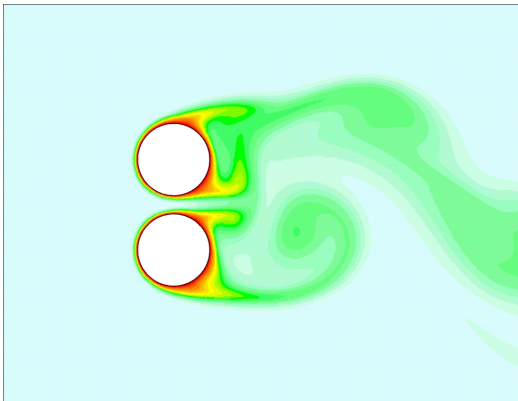
Figure 9-5 Normalized instantaneous thermal field for the cases $s/d = 3.0$ and Re_D ranging from 100 to 500.



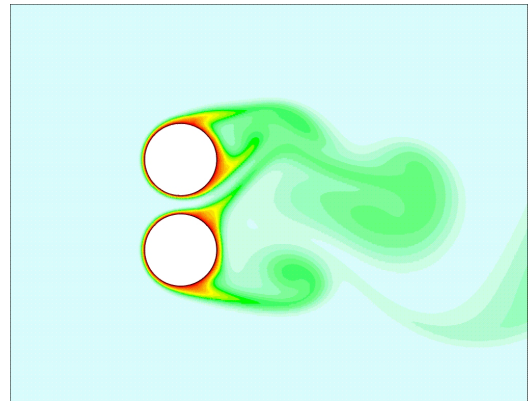
a) $Re_D = 100$



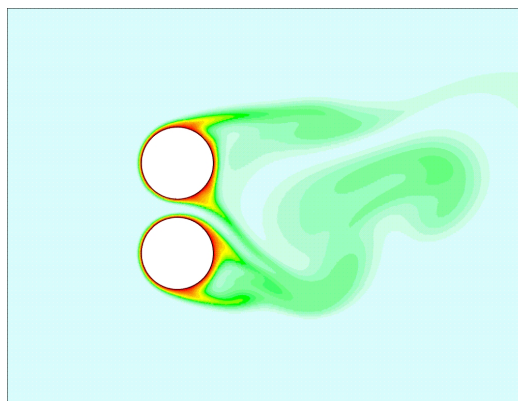
b) $Re_D = 200$



c) $Re_D = 300$



d) $Re_D = 400$



e) $Re_D = 500$

Figure 9-6 Normalized instantaneous thermal field for the cases $s/d = 1.25$ and Re_D ranging from 100 to 500.

9.2.2 Mean Local Nusselt Number

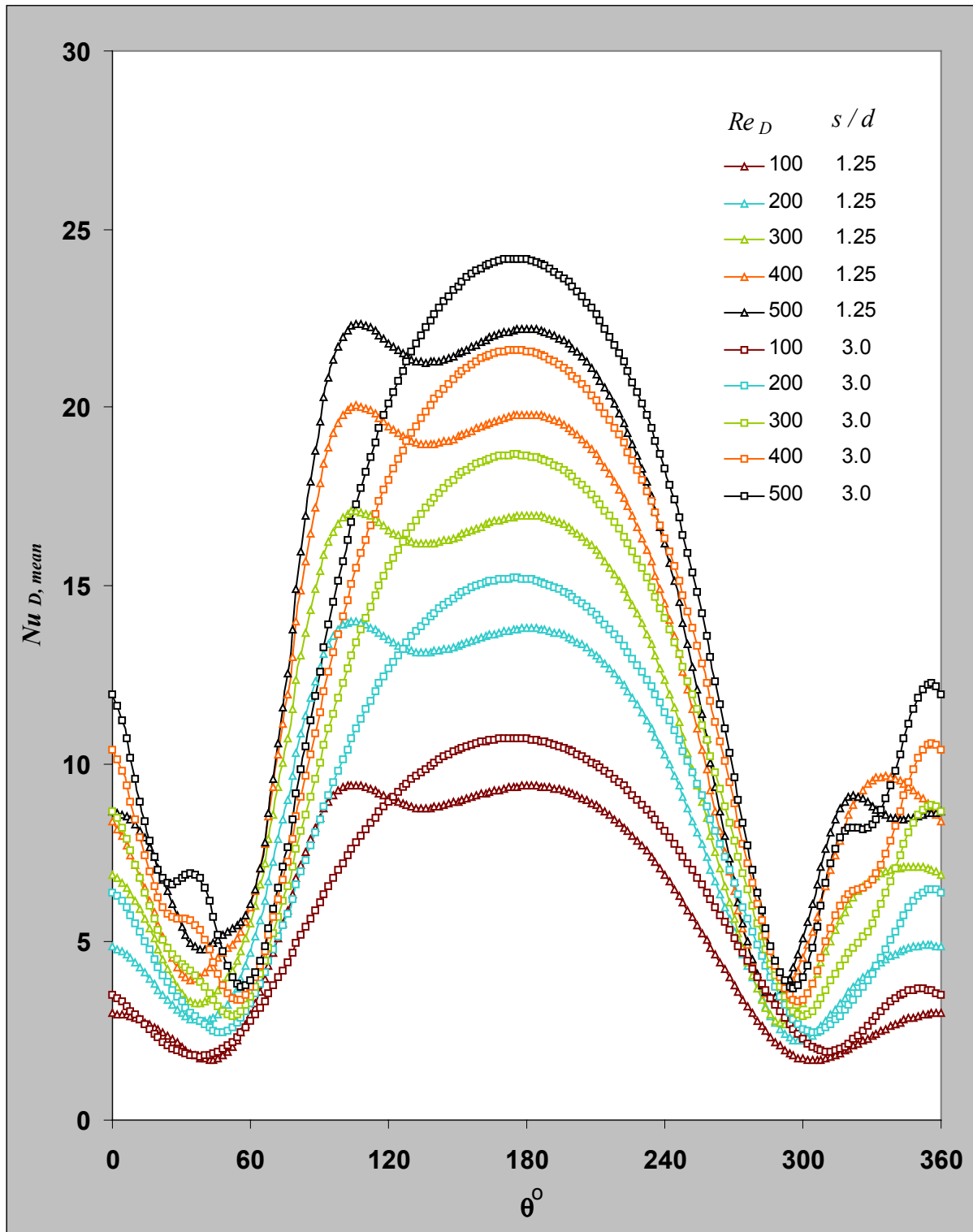
Figure 9-7 represents local values of the mean Nusselt number on the surface of the lower cylinder as defined by Equ. (8.2) for the values of $s/d = 1.25$ and 3.0 , and Reynolds number ranging from 100 to 500 . Starting with Reynolds number of 100 and $s/d = 3.0$, it is seen that the Nusselt number distribution between the two separation points at the upstream part of the cylinder takes a dome shape and it is symmetric about the forward stagnation point. At the downstream part, there is a rising trend in Nusselt number, which reaches its maximum value at an angle of about 350° . Making the two cylinders closer to each other ($s/d = 1.25$) the dome shape of the curve loses its symmetry as the stagnation point moves towards the jet flow. The jet flow enhances the heat transfer in its neighborhood ($60^\circ < \theta < 120^\circ$). Except in this range, the Nusselt number is usually lower than before.

Increasing Reynolds number to be 200 results in a direct enhance in the Nusselt number for both values of the studied pitch to diameter ratios. The two regions that mostly benefit from this growth were the forward stagnation point and the rear (base) point.

At Reynolds number of 300 , any decrease in the distance between the two cylinders enhances the heat transfer process, not only near the jet but also in the downstream part away from the jet flow ($290^\circ < \theta < 345^\circ$). This trend occurs also for Reynolds number of 400 .

It is well noticeable that the maximum value of Nusselt number for $s/d = 1.25$ at the downstream part of the cylinder is found to be in the region away from the jet flow ($290^\circ < \theta < 345^\circ$). It moves towards the separation point by increasing the value of Reynolds number. Nevertheless, it occurs at almost the same position ($\theta \cong 350^\circ$) when $s/d = 3.0$.

For all values of Reynolds numbers, it is found that the position of the forward stagnation point depends only on the value of the pitch to diameter ratio.



Figures 9-7 Local values of the mean Nusselt number on the surface of the lower cylinder for $s/d = 1.25$ and 3.0 and Reynolds number ranging from 100 to 500 .

9.2.3 Mean Average Nusselt Number

Figure 9-8 gives the average Nusselt number for both cylinders versus pitch to diameter ratio s/d for different values of Reynolds number. It is very interesting to find that also for this mode of heat transfer (isothermal walls) there is always a peak value of Nusselt number at a pitch to diameter ratio of about 2.0 for the whole range of Reynolds number. Placing the cylinders approach to each other, this phenomenon becomes significant. At s/d larger than 2.5 the change in Nusselt number versus s/d starts to fade away.

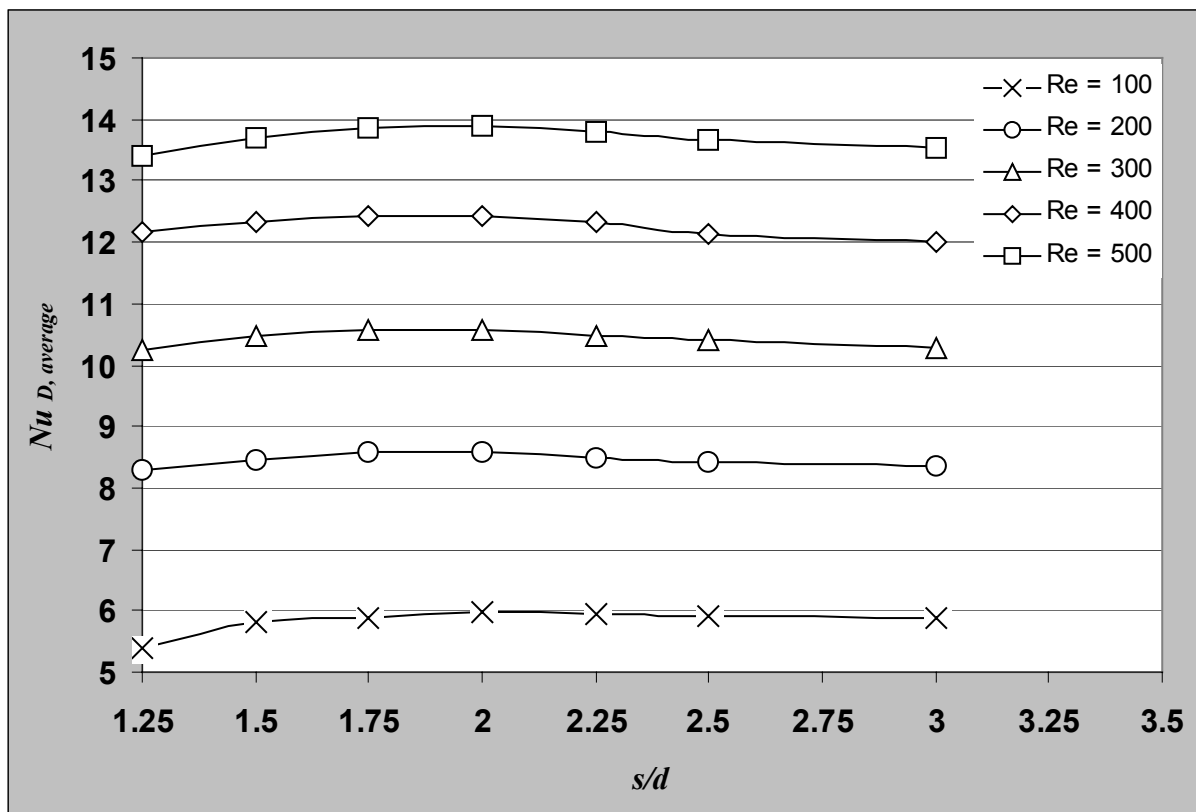


Figure 9-8 Average Nusselt number for both cylinders as one unit versus pitch to diameter ratio s/d for different values of Reynolds number.

According to the previous results, one can say that also for this heat transfer mode, a pitch to diameter ratio of about 2.0 is the best value to be used in design purposes.

Chapter 10

Conclusions and Future Work

10.1 Conclusions

The following conclusions can be drawn on the behavior of two cylinders in a parallel stream of air:

1. It was surprising to find that only the flow characteristics of this problem took attention in the literature and no work was found that concentrates on the heat transfer side of the problem although it is actually of great interest.
2. The nature of the problem requires very careful treatment during the preparation of the solution process. Only higher order numerical schemes gave an acceptably accurate solution of the problem. When solving similar problems, one should keep in mind that the surface of the cylinder must be represented by sufficiently large number of polygons (more than 360 faces).
3. According to the benchmarks utilized, the used program (STAR-CD) showed an excellent ability in solving similar problems to the problem of the current study.
4. The numerical flow field obtained showed a transient behavior that agrees well with the results found in the literature. Until pitch to diameter ratio of 2.0, one can define two coupled vortex streets that show symmetry about the axis of the gap. The biased nature of the flow could be proven numerically and be found to take place for all pitch to diameter values lower than 2.0. The biased nature of the flow has no confined time behavior. The flow changes its direction in an irregular manner. The closer the two cylinders are from each other; the clearer is the biased nature of the flow.
5. The numerical pressure field obtained showed that the pressure distribution around the cylinders loses its symmetry about the point $\theta = 180^\circ$ for all the pitch to diameter

ratios smaller than 2.0. The forwarded stagnation point is shifted towards the jet flow. This movement of the stagnation point is inversely proportional to the pitch to diameter ratio.

6. Until pitch to diameter ratio of 2.0, one can define a sinusoidal variation in lift coefficient with time. For values lower than 2.0, no wavy form of variation with time takes place because of the introduction of the biased flow.
7. For the cases $s/d \geq 2.0$ the calculated Strouhal number was about 0.21. This agrees well with the data found in the literature for two cylinders arranged side by side. For lower values of s/d because of the biased nature of the flow, no definite Strouhal number could be obtained.
8. The calculated mean drag coefficient variation versus pitch to diameter ratio showed a good agreement with the results found in the literature.
9. The calculated thermal field reflected clearly the flow characteristics of the problem. The thermal field is found to be completely driven by the flow field.
10. The distribution of mean local Nusselt number around the cylinders is found to be symmetric about the forward stagnation point for all the values of pitch to diameter ratios ≥ 2.0 . It loses its symmetry for all other values considered. Nusselt number is found to be maximal at the forward stagnation point and to be a minimum around the two separation points. These results are found to be valid for both heat transfer modes considered.
11. Mean average Nusselt number for both cylinders as on unit showed a local peak value at a pitch to diameter ratio of about 2.0 for both studied heat transfer modes. This is a very interesting result because it gives the best way to put the two cylinders together to get the most effective heat transfer coefficients from both of them.
12. Decreasing Reynolds number from 500 to 100 showed no biased jet flow between the cylinders and a large hot region behind the two cylinders is formed from both heat transfer modes used.
13. For the whole range of Nusselt number under consideration, the best way to obtain the most efficient heat transfer coefficient from the cylinders is to put the cylinders one

diameter apart from each other (i.e. pitch to diameter ratio of 2.0). This result was found to be valid for both heat transfer modes used.

10.2 Future Work

At the end of this work, it is useful to draw some lines for any extension research to the current study:

1. It would be very practical to extend the range of the Reynolds number to cover the turbulent region (Reynolds number > 2000). It might be very interesting to study the validity of the result of the maximum average mean Nusselt number for both cylinders that occurs at a pitch to diameter ratio of about 2.0. To study something like this in the turbulent flow regime is really an important subject.
2. The tandem and staggered arrangements of the two cylinders are also of great interest. The staggered distribution combines both tandem and side-by-side arrangement. It will be a very good extension to the current work if one considers studying these cases and searches for an optimum configuration for the two cylinders that optimizes the heat transfer process.

REFERENCES

Single Cylinder

Fluid Flow

- [1] Thom, A.: *An Investigation of Fluid Flow in Two Dimensions*. Aeronaut. Res. Council London Rep. Mem., no.1194, pp.166-183, 1928.
- [2] Thom, A.: *The Flow past Circular Cylinders at Low Speeds*. Proc. R. Soc. London Ser. A, vol.141, pp.651-669, 1933.
- [3] Tomotika, S.; Aoi, T.: *The Steady Flow of Viscous Fluid Past a Sphere and Circular Cylinder at Small Reynolds Numbers*. Quart. J. Mech. Appl. Math., vol.3, part 2, pp.140-161, 1950.
- [4] Kawaguti, M.: *Discontinuous Flow past a Circular Cylinder*. J. Phys. Soc. Jpn., vol.8, no.3, pp.403-406, 1953.
- [5] Kawaguti, M.: *Numerical Solution of the Navier-Stokes Equations for the Flow around a Circular Cylinder at Reynolds Number 40*. J. Phys. Soc. Jpn., vol.8, no.6, pp.747-757, 1953.
- [6] Allen, D. N.; Southwell, R. V.: *Relaxation Methods to Determine the Motion, in Two Dimensions, of a Viscous Fluid past a Fixed Cylinder*. Quart. J. Mech. Appl. Math., vol.8, part 2, pp. 129-145, 1955.
- [7] Taneda, S.: *Experimental Investigation of the Wakes behind Cylinders and Plates at Low Reynolds Numbers*. J. Phys. Soc. Jpn., vol.11, no.3, pp. 302-307, 1956.
- [8] Batchelor, G. K.: *A Proposal Concerning Laminar Wakes behind Bluff Bodies at Large Reynolds Number*. J. Fluid Mech., vol.1, part 4, pp.388-398, 1956.
- [9] Payne, R. B.: *Calculations of Unsteady Viscous Flow past a Circular Cylinder*. J. Fluid Mech., vol.4, part 1, pp.81-86, 1958.
- [10] Apelt, C. J.: *The Steady Flow of a Viscous Fluid past a Circular Cylinder at Reynolds*

- Numbers 40 and 44. Aeronaut. Res. Council Rep. Mem., no.3175, pp.1-28, 1958.*
- [11] Tritton, D. J.: *Experiments on the Flow past a Circular Cylinder at Low Reynolds Numbers. J. Fluid Mech., vol.- 6, part 4, pp.547-567, 1959.*
- [12] Fromm, J. E.; Harlow, F. H.: *Numerical Solution of the Problem of Vortex Street Development, Phys. Fluids, vol.6, no.7, pp. 975-982, 1963.*
- [13] Grove, A. S.; Shair, F. H.; Petersen, E. E.; Acrivos, A.: *An Experimental Investigation of the Steady Separated Flow past a Circular Cylinder, J. Fluid Mech., vol. 19, part 1, pp.60-81, 1964.*
- [14] Dennis, S.C. R.; Shimshoni, M.: *The Steady Flow of a Viscous Fluid past a Circular Cylinder, Aeronaut. Res. Council Current Papers 797, pp.1-44, 1964.*
- [15] Acrivos, A.; Snowden, D. D.; Grove, A. S.; Petersen, E. E.; *The Steady Separated Flow past a Circular Cylinder at Large Reynolds Numbers, J. Fluid Mech., vol.21, part 4, pp.737-760, 1965.*
- [16] Kawaguti, M.; Jam, P.: *Numerical Study of a Viscous Fluid Flow past a Circular Cylinder, J. Phys. Soc. Jpn., vol.21, no.10, pp.2055-2062, 1966.*
- [17] Roshko, A.: *A Review of Concepts in Separated Flow, in Proc. of the First Canadian Congress of Applied Mechanics, (B. H. Karnopp, ed.), Laval University, Quebec, Canada, vol.3, no.5, pp.3-81 to 3-115, 1967.*
- [18] Acrivos, A.; Leal, L. G.; Snowden, D. D.; Pan, F.: *Further Experiments on Steady Separated Flows past Bluff Objects, J. Fluid Mech., vol.34, part 1, pp.25-48, 1968.*
- [19] Hamielec, A. E.; Raal, J. D.: *Numerical Studies of Viscous Flow around Circular Cylinders, Phys. Fluids, vol.12, no.1, pp.11-17, 1969.*
- [20] Son, J. S.; Hanratty, T. J.: *Numerical Solution for the Flow around a Cylinder at Reynolds Numbers of 40, 200 and 500, J. Fluid Mech., vol.35, part 2, pp.369-386, 1969.*
- [21] Takami, H.; Keller, H. B.: *Steady Two-Dimensional Viscous Flow of an Incompressible Fluid past a Circular Cylinder, Phys. Fluids, Suppl. II, vol.12, no.12, pp. II-51 to II-56, 1969.*

- [22] Jain, P. C.; Rao, K. S., *Numerical Solution of Unsteady Viscous Incompressible Fluid Flow past a Circular Cylinder*, Phys. Fluids, Suppl. II, vol.12, no.12, pp.II-57 to II-64, 1969.
- [23] Thoman, D. C.; Szewczyk, A. A.: *Time-Dependent Viscous Flow over a Circular cylinder*, Phys. Fluids, Suppl. II, vol.12, no.12, pp. II-76 to II-87, 1969.
- [24] Dennis, S. C. R.; Chang, G. Z.: *Numerical Solutions for Steady Flow past a Circular Cylinder at Reynolds Numbers up to 100*, J. Fluid Mech., vol.42, part 3, pp. 471-489, 1970.
- [25] Collins, W. M.; Dennis, S. C. R.: *Flow past an Impulsively Started Circular Cylinder*, J. Fluid Mech., vol.60, part 1, pp.105-127, 1973.
- [26] Jam, P. C.; Goel, B. S.: *Shedding of Vortices behind a Circular Cylinder*, Computers and Fluids, vol. 4, no.1, pp.137-142, 1976.
- [27] Patel, V. A.: *Time-Dependent Solutions of the Viscous Incompressible Flow past a Circular Cylinder by the Method of Series Truncation*, Computers and Fluids, vol.4, no.1, pp.13-27, 1976.
- [28] Nagata, H.; Matsui, T.; Ichikawa, M.: *Velocity Field of the Flow around a Circular Cylinder Started Impulsively (2nd Report, Unsteady Boundary Layers)*, int. J. Jpn. Soc. Mech. Eng., vol.23, no.179, pp. 696-704, 1980.
- [29] Fornberg, B.: *A Numerical Study of Steady Viscous Flow past a Circular Cylinder*, J. Fluid Mech., vol.98, part 4, pp. 819-855, 1980.

Fluid Flow-Heat Transfer References

- [30] Giedt, W. H.: *Investigation of Variation of Point Unit Heat-Transfer Coefficient around a Cylinder Normal to an Air Stream*, Trans. ASME, vol.71, no.4, pp.375-381, 1949.
- [31] Giedt, W. H.: *Effect of Turbulence Level of Incident Air Stream on Local Heat Transfer and Skin Friction on a Cylinder*, J. Aeronaut. Sci., vol.18, no.11, pp. 725-730, 766, 1951.

- [32] Eckert, E. R. G.; Soehngen, E.: *Distribution of Heat-Transfer Coefficients around Circular Cylinders in Crossflow at Reynolds Numbers from 20 to 500*, Trans. ASME, vol. 74, no.3, pp.343-347, 1952.
- [33] Van der Hegge Zijnen, B. G.: *Modified Correlation Formulae for the Heat Transfers by Natural and by Forced Convection from Horizontal Cylinders*, Appl. Sci. Res., vol.6, sec. A, pp.129-140, 1956.
- [34] Corns, D. C.; Williams, M. J.: *Two-Dimensional Convection from Heated Wires at Low Reynolds Numbers*, J. Fluid Mech., vol.6, part 3, pp.357-384, 1959.
- [35] Perkins, Jr., H. C.; Leppert, G.: *Forced Convection Heat Transfer from a Uniformly Heated Cylinder*, J. Heat Transfer, vol.84, ser. C, no.3, pp.257-263, 1962.
- [36] Van Meel, D. k: *A Method for the Determination of Local Convective Heat Transfer from a Cylinder Placed Normal to an Air Stream*, int. J. Heat Mass Transfer, vol.5, pp.715-722, 1962.
- [37] Richardson, P. D.; *Heat and Mass Transfer in Turbulent Separated Flows*, Chem. Eng. Sci., vol.18, pp. 149-155, 1963.
- [38] Suter, S. P.; Maeder, P. F.; Kestin, J.: *On the Sensitivity of Heat Transfer in the Stagnation-Point Boundary Layer to Free-Stream Vorticity*, J. Fluid Mech., vol.16, part 4, pp.497-520, 1963.
- [39] Harlow, F. H.; Fromm, J. E.: *Dynamics and Heat Transfer in the Von Karman Wake of a Rectangular Cylinder*, Phys. Fluids, vol.7, no.8, pp.1147-1156, 1964.
- [40] Suter, S. P.: *Vorticity Amplification in Stagnation-Point Flow and Its Effect on Heat Transfer*, J. Fluid Mech., vol.21, part 3, pp.513-534, 1965.
- [41] Smith, M. C.; Kueth, A. M.: *Effects of Turbulence on Laminar Skin Friction and Heat Transfer*, Phys. Fluids, vol.9, no.12, pp.2337-2344, 1966.
- [42] Kestin, J.: *The Effect of Free-Stream Turbulence on Heat Transfer Rates*, in Advances in Heat Transfer, vol. 3 (J. P. Hartnett and T. F. Irvine, Jr., eds.), pp.1-32, Academic Press, New York, 1966.
- [43] Dennis, S. C. R.; Hudson, J. ,D.; Smith, N.: *Steady Laminar Forced Convection from a*

- Circular Cylinder at Low Reynolds Numbers*, Phys. Fluids, vol.11, no.5, pp.933-940, 1968.
- [44] Suter, S. P.; Williams, G.: *The Effect of External Vorticity on Stagnation-Point Heat Transfer at High Prandtl Number*, int. J. Heat Mass Transfer, vol. 11, no. 12, pp.1795-1806, 1968.
- [45] Sikinanovic, S.; Oka, S.; Koncar-Djurdjevic, S.: *Influence of the Structure of Turbulent Flow on Heat Transfer from a Single Cylinder in a Cross Flow*, in Proc. of the 5th int. Heat Transfer Conf., Tokyo, Japan, vol.2, FC 5.7, pp.320-324, Hemisphere, New York, 1974.
- [46] Lowery, G. W.; Vachon, R. I.: *The Effect of Turbulence on Heat Transfer from Heated Cylinders*, int. J. Heat Mass Transfer, vol.18, no.11, pp.1229-1242, 1975.
- [47] Morgan, V. T.: *The Overall Convective Heat Transfer from Smooth Circular Cylinder*, in Advances in Heat Transfer, vol.11 (J. P. Hartnett and T. F. Irvine, Jr., eds.), pp.199-264, Academic Press, New York, 1975.
- [48] Jain, P. C.; Goel, B. S.: *A Numerical Study of Unsteady Laminar Forced Convection from a Circular Cylinder*, J. Heat Transfer, vol.98, ser. C, no.2, pp. 303-307, 1976.
- [49] Apelt, C. J.; Ledwich, M. A.: *Heat Transfer in Transient and Unsteady Flows past a Heated Circular Cylinder in the Range $1 \leq R \leq 40$* , J. Fluid Mech., vol. 95, part 4, pp.761-777, 1979.
- [50] Papell, S. S.: *Influence of Thermal Boundary Conditions on Heat Transfer from a Cylinder in Crossflow*, NASA Technical Paper 1894, NASA Lewis Research Center, OH, 1981.
- [51] Van Fossen, G. J.; Simoneau, R. J.; Olsen, W. A. Jr.; Shaw, R. J.: *Heat Transfer Distributions around Nominal Ice Accretion Shapes Formed on a Cylinder in the NASA Lewis Icing Research Tunnel*, AIAA 22nd Aerospace Sciences Meeting, Reno, NV, AIAA Paper 84-0017, 1984.
- [52] Arimilli, R. V.; Keshock, E. G.; Smith, M. E.: *Measurements of Local Convective Heat Transfer Coefficients on Ice Accretion Shapes*, MAA 22nd Aerospace Sciences Meeting, Reno, NV, AIAA Paper 84-0018, 1984.

- [53] Baughn, J. W.; Elderkin, M. J.; McKillop, A. A.: *Heat Transfer from a Single Cylinder, Cylinders in Tandem, and Cylinders in the Entrance Region of a Tube Bank with a Uniform Heat Flux*, J. Heat Transfer, vol.108, no.2, pp.386-391, 1986.
- [54] Pais, M.; Singh, S. N.: *Local Heat-Transfer Coefficients of Simulated Smooth Glaze Ice Formations on a Cylinder*, J. Thermophys. Heat Transfer, vol.1, no.2, pp.117-121, 1987.
- [55] Baughn, J. W.; Saniei, N.: *The Effect of The Thermal Boundary Condition on Heat Transfer from a Cylinder in Cross flow*, J. Heat Transfer, vol.113, no.4, pp.1020-1023, 1991.
- [56] Ahmad, R. A.; Qureshi, Z. H.: *Laminar Mixed Convection from a Uniform Heat Flux Horizontal Cylinder in a Crossflow*, J. Thermophys. Heat Transfer, vol.6, no.2, pp.277-287, 1992; see also AIAA Paper 91-0383, Jan.1991.

Two and more Cylinders

Fluid Flow

- [57] Biermann, D.; Herrnstein, W. H., Jr.: *The Interference between Struts in Various Combinations*, National Advisory Committee for Aeronautics, Tech. Rep. 468, 1933.
- [58] Landweber, L.: *Flow About a Pair of Adjacent, Parallel Cylinders Normal to a Stream*, Navy Dept. D. W. Taylor Model Basin, Report 485, Washington, D.C., 1942
- [59] Spivak, H. M.: *Vortex Frequency and Flow Pattern in the Wake of Two Parallel Cylinders at Varied Spacings Normal to an Air Stream*, Journal Aeronautical Science, Vol. 13, 1946.
- [60] Hori, E.: *Experiments on Flow Around A Pair of Parallel Circular Cylinders*. Proc. 9th Japan National Congress for Applied Mech. Tokyo, pp. 231-234, 1959.
- [61] Ishigai, S.; Nishikawa, E.; Nishimura, K.; Cho, K.: *Experimental Study on Structure of Gas Flow in Tube Banks with Tube Axes Normal to Flow(Part 1, Karman Vortex Flow around two Tubes at Various Spacings)*, Bulletin of the Japan Society Mechanical

- Engineering, Vol. 15, No. 86, pp. 949-956, 1972.
- [62] Zdravkovich, M. M.: *Review of Flow Interference Between Two Cylinders in Various Arrangements*, Trans. ASME J. Fluids Engineering 618-633, 1977.
- [63] Stansby P. K.: *A Numerical Study of Vortex Shedding From One And Two Circular Cylinders*, Aero. Q. 48-71, 1981.
- [64] Chen, C., K.; Wong, K. L.; Cleaver, J., W.: *Finite Element Solution of Laminar And Heat Transfer of Air in A Staggered And in-Line Tube Bank*. *Int. Heat Fluid Flow* 4, 291, 1986
- [65] Li, J.; Chambarel, A.; Donneaud, M.; Martin R.: *Numerical Study of Laminar Flow Past One and Two Circular Cylinders*, *Computers & Fluids* vol. 19 No. 2, pp. 155-170, 1991.
- [66] Braun, M. J.; Kudriavtsev, V. V.: *Fluid Flow Structures in Staggered Banks of Cylinders Located in a Channel*, *J. of Fluids Engineering, Transaction of the ASME*, vol. 117, pp. 36-44, 1995.
- [67] Ichioka, T.; Kawata, Y.; Nakamura, T.; Izumi, H.; Kobayashi, T.; Takamatsu, H.: *Research on Fluid Elastic Vibration of Cylinder Arrays by Computational Fluid Dynamics (Analysis of Two Cylinders and a Cylinder Row)*, *JSME int. Journal, Seri. B*, vol. 40, No. 1, pp. 16-24 1997.
- [68] Bearman, P. W.; Wadcock, A. J.: *The interaction between a pair of circular cylinders normal to a stream*, *J. Fluid Mech.*, vol. 61, part 3, pp. 499-511, 1973.

General

- [69] Gosman, A. D.; Pun W.M.; Runchal, A. K.; Spalding, D. B.; Wolfstein, M: *Heat and Mass Transfer in Recirculating Flows*, Academic Press, London, 1969.
- [70] Patanker, S. V.: *Numerical Heat Transfer and Fluid Flow*, Hemisphere, Washington, D. C., 1981.
- [71] Warsi, Z.V.A.: *Conservation Form of the Navier-Stokes Equations in General*

- Nonsteady Coordinates*, AIAA J., 19, pp. 240-242, 1980.
- [72] Lai, K. Y. M.: *Numerical Analysis of Fluid Transport Phenomena*, PhD Thesis, University of London 1983.
- [73] Leschinziner, M. A.: *Practical evaluation of three finite difference schemes for the computations of steady-state recirculating flows*, Comp. Meth. In Appl. Mech. & Eng., 23, pp. 293-312, 1980.
- [74] Hirsch, C.: *Numerical Computation of Internal and External Flows, Vol. II: Computational Methods for Inviscid and Viscous Flows*, John Wiley & Sons, New York, 1960.
- [75] Richtmeyer, R. D.; Morton, K. W.: *Difference Methods for Initial-Value Problems*, 2nd Edition, Wiley-Interscience, New York, 1967.
- [76] Wilkes, N. S.; Thompson, C. P.: *An evaluation of higher-order upwind differencing for elliptic flow problems*, CSS 137, AERE, Harwell, 1983.
- [77] Issa, R. I.: *Solution of the implicitly discretised reacting flow equations by operator-splitting*, J. Comp. Phys., 62, pp. 66-82, 1986.
- [78] Schäfer, M.; Turek S.: *Benchmark Computations of Laminar Flow Around a Cylinder*, Notes on Numerical Fluid Mechanics, Vol. 52 "Flow Simulation with High-Performance Computers II, Vieweg, 1996.
- [79] Niedergesäß, A.: *Berechnung zweidimensionaler laminarer Rezirkulationsströmungen*, Kleine Studienarbeit, Institut für Mechanik, D6-453/96, Universität Hannover 1996. (unveröffentlicht)
- [80] *STAR-CD User Guide. Version 3.05*, Computational Dynamics Limited, London, 1998.
- [81] Nieuwstadt, F; Keller, B.: *Viscous Flow Past Circular Cylinders*, Computers & Fluids, Vol. 1, pp. 59-71. Pergamon Press 1973.
- [82] Muzaferija, S.; Peric, M.; Seidl, V.: *Computation of Flow Around Circular Cylinder in A Channel*, Internal Report, Institut für Schiffbau, University of Hamburg, 1995.

Lebenslauf

Persönliche Daten

Name	Khaled Yahia Zakaria
Geburtsdatum	15. November 1967
Geburtsort	Alexandria, Ägypten
Familienstand	verheiratet mit 2 Kindern

Schulbildung

1973-1982	Einschulung in die Grundschule, Alexandria
1982-1985	Secondary-Schule in Alexandria

Hochschulausbildung

1990	B.Sc. Maschinenbau an der Universität Alexandria
1993	M.Sc Maschinenbau an der Universität Alexandria

Praktika

1985	Al-Ahram Co. Alexandria
1993	Alexandria Water Organisation

Berufliche Tätigkeiten

1990-1995	Wissenschaftlicher Mitarbeiter an der Universität Alexandria-Ägypten
seit 1995	DAAD Stipendiat am Institut für Mechanik der Universität Hannover